Two Jets Production in Neutral Current Deep Inelastic e^+p Interactions at 300 GeV c.m.s. energy

PhD Thesis

Maciej Przybycień

Institute of Nuclear Physics,
Kawiory 26a, 30-055 Cracow, Poland

Abstract

The exclusive dijet cross section has been measured in deep inelastic e^+p scattering at 300 GeV c.m.s. energy at the HERA collider. The whole 1995 data sample collected by the ZEUS detector has been used in this analysis, which corresponds to integrated luminosity of 6.1 pb^{-1}. Jets were identified using the cone and the cluster (k_T) algorithms in the laboratory frame. Jets were required to have axis in the pseudorapidity range -2 $< \eta <$ 2 in laboratory frame and transverse momentum greater then 4 GeV in both, laboratory and center-of-mass frames. Only events with 7 $GeV^2 < Q^2 <$ 100 GeV^2 were accepted. The measured cross section at the hadron level is $\sigma_{cone}^{hadr} = 3.04 \pm 0.03(stat)^{+0.36}_{-0.39}(sys) nb$ ($\sigma_{k_T}^{hadr} = 2.74 \pm 0.03(stat)^{+0.34}_{-0.39}(sys) nb$) and at the parton level: $\sigma_{cone}^{part} = 3.93 \pm 0.04(stat)^{+0.34}_{-0.61}(sys) nb$ ($\sigma_{k_T}^{part} = 3.74 \pm 0.04(stat)^{+0.38}_{-0.62}(sys) nb$). Although the shapes of kinematical and jet variables distributions are well described by most of the models, the absolute normalization is not reproduced by any.

Contents

1 Introduction **1**

2 ep deep inelastic scattering processes **2**

2.1 DIS kinematics 2

2.2 NC DIS and structure functions 3

2.3 The naive parton model 4

2.4 The QCD-improved parton model 5

2.5 Perturbative QCD and parton evolution equations 6

2.6 Parton parameterizations 10

2.7 Extracting of gluon density from dijet production in DIS 11

2.8 Dijet production as a probe of BFKL dynamics 13

3 Experiment **15**

3.1 HERA collider 15

3.2 ZEUS detector 17

3.2.1 Tracking system 18

3.2.2 Calorimeter 20

3.2.3 Other components 22

3.2.4 Luminosity monitor 23

3.3 ZEUS trigger system 25

4 Monte Carlo simulation **27**

4.1 Monte Carlo models 27

5 Reconstruction of the kinematical variables **30**

5.1 Reconstruction methods 30

5.2 Smearing and migration effects 31

6 Event selection **33**

6.1 On-line DIS trigger 33

6.2 Off-line data selection 34

6.3 Jets search 36

6.4 Rejection of background events. 39

7 Jet studies **41**

7.1 Energy flow around the jet axis 41

7.2 Jet shapes 41

7.3 Jet energy scale and energy corrections 46

7.3.1 P_T balance method in DIS 49

7.3.2 P_T balance method results 49

7.3.3 Jet energy corrections from $P_{T,had(part)}/E_{T,cal}$ comparison 52

8 Determination of dijet cross section using the cone algorithm **57**

8.1 Detector level comparison between MC and data 57

8.2 Corrections for detector effects 57

8.3 Total and differential dijet cross section determination 60

8.4 The Born cross section 64

8.5 Systematic studies 65

8.6 High or asymmetric E_T jet cuts 67

9 Determination of dijet cross section using k_T algorithm **73**

10 Dijet decorrelation as a probe of BFKL dynamics **83**

11 Summary **86**

Acknowledgments **88**

Bibliography **89**

A Appendix **93**

1 Introduction

The deep inelastic (DIS) lepton nucleon scattering experiments have played a crucial role in the understanding of hadronic matter. On the basis of the results from these experiments the theory of strong interactions between quarks and gluons, Quantum Chromodynamics (QCD), has been developed.

The first electron-proton collider HERA with a center-of-mass energy of 300 GeV, has allowed the probing of the structure of the proton in a kinematic region previously unexplored and unreachable in fixed target scattering experiments. Two HERA experiments, ZEUS and H1 have shown the rapid rise of the F_2 structure function with decreasing x (Bjorken scaling variable, i.e. the fraction of the proton momentum carried by a parton) which is well described by the perturbative QCD and can be interpreted as a steady increase of the slow partons contribution to the proton momentum.

The analysis of hadronic final states provides unique and abundant information on the parton densities inside such objects as the proton, the photon and even the hypothetical pomeron and allows to perform the decisive tests of various theoretical models.

In this thesis the measurement of the exclusive neutral current (NC) DIS dijet production cross section at medium momentum transfer squared (Q^2) using the HERA data collected with the ZEUS detector in 1995 is presented. The cross section is measured at the hadron and the parton levels. The results are compared to Monte Carlo (Ariadne, Lepto, Herwig) and to exact NLO QCD analytical calculations.
For the inclusive NC DIS dijet production the decorrelation effects as a possible sign of BFKL dynamics are analyzed.

Section 2 covers an introduction to deep inelastic scattering and the discussion of structure functions, the simple and the QCD improved quark-parton model and the parton evolution equations. In particular the applicability regions of different evolution schemes, unfolding of gluon density and dijet decorrelation as a BFKL signal are discussed. The HERA collider, the ZEUS detector, the trigger and the data acquisition system are described in Section 3. In Section 4 some information about Monte Carlo techniques and generators applied for the event simulations are given. Different reconstruction methods of kinematical variables together with smearing and migration effects are compared in Section 5. Data selection, jet reconstruction techniques, background effects and methods of its removal are discussed in Section 6. Section 7 is devoted to the jet studies. The measured jet shapes and energy flow around the jet axis are compared to the MC model's predictions. The jet energy scale difference between MC and the experimental data is measured with an E_T balancing method. The jet energy correction methods are also described. In Section 8 the differential and total cross sections are discussed at the hadron and the parton levels. The experimental results are compared to the MC predictions and NLO analytical QCD calculations. The dijet decorrelation as a possible BFKL sign is analysed. The summary of the results presented in this thesis is given in Section 9.

2 ep deep inelastic scattering processes

Deep Inelastic Scattering (DIS) is defined as the scattering of a lepton from a nucleon with high momentum transfer. We distinguish two classes of ep DIS events[1]:

$$e^- + p \to e^- + X \quad \text{and} \quad e^- + p \to \nu + X$$

where X denotes the total hadronic system in the final state. The first reaction is known as a neutral current (NC) DIS, because the intermediate vector boson is neutral (γ,Z^0), whereas in the second process, so called charged current (CC) DIS, the intermediate vector boson is charged ($W^{\pm}$) and the initial electron converts to an neutrino.
In this thesis we restrict ourselves to the study of NC deep inelastic scattering of unpolarized electrons and protons, for which the final electron and final hadrons are detected. Deep inelastic lepton-hadron scattering is the most powerful test of perturbative Quantum Chromodynamics (pQCD), since its study offers the direct determination of the momentum distributions of partons in hadrons.
In the following we describe the basic kinematics of DIS events, naive and improved quark-parton model and the dynamical equations governing evolution of partons in different kinematical regions. Dijet decorrelation as a possible sign of BFKL evolution is also discussed.

2.1 DIS kinematics

A schematic view of the ep NC DIS in one photon exchange approximation in shown in Fig. 2.1. The incoming electron e with four-momentum k $(\vec{k}, E)$ is scattered off the proton P with four-momentum p via the exchange of a virtual photon ($\gamma^\star$) with four-momentum q. The scattered electron $e^{'}$ has four-momentum $k^{'}$ $(\vec{k'}, E^{'})$ and X denotes the hadronic final state. The kinematics of deep inelastic ep scattering can be described by the two independent variables from which all other variables can be derived. Below the definitions of three commonly used basic kinematic variables are given.

$$Q^2 \equiv -q^2 = -(k - k^{'})^2 > 0 \tag{2.1}$$

$$x = \frac{Q^2}{2p \cdot q} \; ; \; (0 < x < 1) \tag{2.2}$$

$$y = \frac{p \cdot q}{p \cdot k} \; ; \; (0 < y < 1) \tag{2.3}$$

Q^2 is the four-momentum transfer variable, x [1] is interpreted as a fraction of the proton momentum carried by the struck quark. y [1] is the fraction of energy lost by the initial electron calculated in the proton rest frame.

[1] In the analysis presented in this thesis the data on positron-proton interactions were used but throughout the text the word "electron" is used to denote the initial lepton.

Denoting by s the total energy squared for the colliding electron and proton the following relation holds:

$$s = \frac{Q^2}{xy} \tag{2.4}$$

Other useful variables are: the invariant mass squared of the hadronic system :

$$W^2 = (p+q)^2 = Q^2\left(\frac{1}{x} - 1\right) + m_p^2 \tag{2.5}$$

(where m_p is the proton mass) and electron energy loss in the proton rest frame:

$$\nu = \frac{p \cdot q}{M} = E - E' \tag{2.6}$$

2.2 NC DIS and structure functions

The cross section for ep NC DIS, has the following form [2]:

$$\frac{d^2\sigma}{dxdQ^2} = \frac{4\pi\alpha^2}{xQ^4}[y^2 x F_1(x,Q^2) + (1-y)F_2(x,Q^2)] \tag{2.7}$$

where α is the fine-structure constant. $F_1(x,Q^2), F_2(x,Q^2)$ are the structure functions. They are functions of the two independent kinematic variables (here x, Q^2 were chosen). The cross section for the reaction $ep \to eX$ can also be described by the convolution of the flux [3] of virtual photons and the absorption cross sections for transversely polarized virtual photon $\sigma_T(Q^2,x)$ and for a longitudinally polarized photon $\sigma_L(Q^2,x)$. For $Q^2 \ll \nu$ and $x \ll 1$ which applies for HERA, this cross section reduces to:

$$\frac{d^2\sigma}{dxdQ^2} = \frac{\alpha}{2\pi x Q^2}[y^2\sigma_T(x,Q^2) + 2(1-y)(\sigma_T(x,Q^2) + \sigma_L(x,Q^2))] \tag{2.8}$$

The virtual photon cross sections are usually written in terms of structure functions of the proton. The relationship between the structure functions and the virtual cross sections is:

$$2xF_1(x,Q^2) = \frac{Q^2}{4\pi^2\alpha}\sigma_T(x,Q^2) \tag{2.9}$$

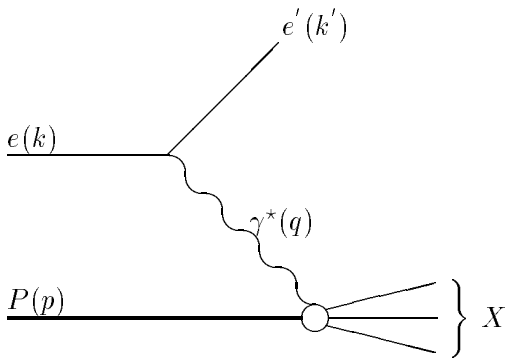

Figure 2.1: *Schematic diagram of ep DIS in one photon exchange approximation.*

$$F_2(x,Q^2) = \frac{Q^2}{4\pi^2\alpha}(\sigma_T(x,Q^2) + \sigma_L(x,Q^2)) \tag{2.10}$$

The longitudinal structure function: $F_L = F_2 - 2xF_1$. The experimental program is to measure the structure functions F_2, F_1 or F_2, F_L.

If large Q^2 virtual photons resolve point like constituents inside the proton then the structure functions F_1 and F_2 become functions of the single variable $x = \frac{Q^2}{2M\nu}$:

$$F_1(x,Q^2) \to F_1(x) \tag{2.11}$$

$$F_2(x,Q^2) \to F_2(x) \tag{2.12}$$

This property, called *scale invariance*, was first postulated by Bjorken [1]. It was experimentally observed [4]. Naive parton model gives explanation of scaling property.

2.3 The naive parton model

In the quark parton model description of DIS scattering the virtual photon interacts with one of the constituent quarks in the proton. We view the process from the infinite momentum frame of the proton. The relativistic time dilation slows down the rate with which the quarks interact with each other. The quark appears essentially free during the short time of interaction with the photon. Thus the electron-proton interaction may be described as an incoherent sum of the scatterings from single free quarks:

$$\frac{d^2\sigma}{dxdQ^2} = \sum_q \int_0^1 d\xi f_q(\xi) \left(\frac{d^2\sigma}{dxdQ^2}\right)_{eq} \tag{2.13}$$

where $f_q(\xi)$ is the probability of finding the quark q in the proton carrying a fraction ξ of it momentum. To determine the structure function $F_i(x)$ from equations (2.11), (2.12) we need to know the cross section for electron-quark scattering process:

$$\left(\frac{d^2\sigma}{dxdQ^2}\right)_{eq} = \frac{2\pi\alpha^2 e_q^2}{Q^4}[1 + (1-y^2]\delta(x-\xi) \tag{2.14}$$

where α is fine-structure constant, e_q is the fractional charge of the struck quark. The α^2/Q^4 comes from the coupling and virtuality of exchanged photon. The factor in square brackets arises from spin-1/2 quarks. The outgoing quark is on the mass-shell and has four-momentum $\xi p + q$, so:

$$m_q^2 = (\xi p + q)^2 \approx 2p \cdot q\xi - Q^2 \tag{2.15}$$

Comparing equations (2.2) and (2.15) we see that $\xi = x$ for $Q^2 \gg m_q^2$. Using the equations: (2.7), (2.13) and (2.14) we obtain the quark-parton model predictions:

$$F_2 = 2xF_1 = x\sum_q e_q^2 \int_0^1 d\xi f_q(\xi)\delta(x-\xi) = \sum_q e_q^2 x f_q(x) \tag{2.16}$$

This result displays the postulated scaling behavior of the structure function: $F_{i=1,2}(x,Q^2) = F_{i=1,2}(x)$. As shown by equation (2.16), the structure functions F_1, F_2 are dependent. The relation $F_2 = 2xF_1$ follows from spin 1/2 nature of partons and is known as Callan-Gross relation [5].

In the quark-parton model we assume the proton is built of the three-constituent or three-valence quarks $u_v u_v d_v$ accompanied by many quark-antiquark pairs. These are known as "sea" quarks. If we sum over all partons we have to reconstruct the total momentum of the proton. However the data show that about half of the proton momentum is carried by objects which does not couple to the photon [6]. Quantum Chromodynamics (QCD) postulates that the missing momentum of the proton is carried by gluons. Gluons mediate the strong interactions and bind the quarks within the proton.

2.4 The QCD-improved parton model

QCD postulates that the constituents of proton (partons) carry a new quantum number "colour" and that the interactions between them are mediated also by the coloured gluons and depend on this number. Scaling violation observed for the proton structure function [6], i.e. their dependence on Q^2 suggests that the strong coupling constant α_s also depends on Q^2 and

$$\alpha_s(Q^2) = \frac{\alpha_s(\mu^2)}{1 + [\alpha_s(\mu^2)/6\pi](33/2 - n_f) ln(Q^2/\mu^2)}$$

where n_f is the number of different flavors, μ is the renormalization point, at which the coupling α_s was measured. The factor $\frac{33}{2}$ comes from non-Abelian character of QCD what means that gluons themselves carry the colour charge and hence couple to each other. It causes $\alpha_s(Q^2)$ to decrease with increasing Q^2. From this formula can be seen that in QCD partons are asymptotically free, that is $\alpha_s \to 0$ as $Q^2 \to \infty$. This property is unique to non-Abelian gauge theories.
The variation of α_s with Q^2 but not its absolute value can be derived from QCD. The α_s was determined by experiments and its value is [7] (after translation to the common scale $Q^2 = M_Z^2$ where M_Z is the mass of the Z boson) :

$$\alpha_s(M_Z) = 0.117 \pm 0.005(stat)^{+0.004}_{-0.005}(syst)$$

Since α_s increases as Q^2 decreases. It leads to the (colour) confinement of quarks and gluons inside the hadrons, so called infrared slavery. Colour confinement means that in experiments we can not see the struck quark, but an energetic jet of (colour neutral) hadrons.

2.5 Perturbative QCD and parton evolution equations

A physical quantity C_a (eg. cross section, structure function), when calculated perturbatively in QCD is expanded as a power series in the strong coupling constant α_s [9]:

$$C_a = C_a^0 + C_a^1(\frac{\alpha_s}{2\pi}) + C_a^2(\frac{\alpha_s}{2\pi})^2 + ... \tag{2.17}$$

where subsequent terms are called lowest or Born term, first order correction, second order and so on. The leading order (LO) calculation gives only the first non-zero term in the series. A next-to-leading order (NLO) calculation gives the next term, and so on. The coefficients C_a^n are usually evaluated using Feynman diagrams.
For processes involving the emission of photons and gluons often the most important contribution to the amplitudes comes from photons and gluons which are emitted colinear with the radiating lepton or quark [8] [10]. Each n-term in (2.17) is then usually enhanced by the presence of a kinematic terms such as ln^nQ^2. While $\frac{\alpha_s}{2\pi} \ll 1$, $\frac{\alpha_s}{2\pi}lnQ^2$ may be of order of 1 and one has to sum the series to all orders of α_s. The sum of all terms proportional to $(\frac{\alpha_s}{2\pi}lnQ^2)^n$ gives the leading log approximation (LLA),

$$C_a^{(LLA)} = \sum_{n=0}^{n=\infty} \tilde{C}_a^{(n)} \left(\frac{\alpha_s}{2\pi}lnQ^2\right)^n \tag{2.18}$$

The next-to-leading logarithmic approximation (NLLA) leads in addition to the series of terms $\alpha_s ln^{n-1}Q^2$. In the NLLA all the leading and the next-to-leading terms must be summed up.
In perturbative calculations in the small x regime also terms $ln^n(\frac{1}{x})$ become large. Thus depending on the approximation one can have either a (N)LLA in lnQ^2 or in $ln\frac{1}{x}$. The approximation where both the large lnQ^2 and $ln\frac{1}{x}$ are taken into account leads to so called double leading logarithmic (DLL) approximation.

Since the coefficients C_a^n are evaluated using Feynman diagrams the divergences which arise in these calculations have to be handled. In order to perform it a renormalization scheme [11] must be adopted. In addition a scale μ must be introduced to represent the point at which the coupling constant α_s is renormalized. As a results, the coefficients depend on both the renormalization scheme and the scale μ. This scale is denoted as the *renormalization scale*. Of course, physics is independent of the adopted renormalization scheme and the scale choice [11]. The renormalization group equation applied to the perturbative expansion representing physical quantity tells us that we must choose the renormalization scale μ of the order of the characteristic scale of the hard process under the study. Any ambiguity with regard to a proper choice of the scale should be resolved by computing to the next order in α_s [11].

The asymptotic freedom and the factorization theorems are nontrivial properties of QCD, which allow to represent the cross sections for hard processes as a convolution of universal parton distributions and process dependent elementary cross sections describing

the hard scattering of partons.
In case of deep inelastic scattering the factorization theorem for any structure function $F(x,Q^2)$ reads as follows:

$$F(x,Q^2) = \sum_i \int_x^1 \frac{dz}{z} C_i \left(\frac{x}{z}, \alpha_s(\mu_F^2), \frac{Q^2}{\mu_F^2}) \right) f_i(z,\mu_F^2) + O(\frac{\Lambda}{Q^2}) \tag{2.19}$$

where C_i are the process dependent coefficient functions, f_i are universal, process independent parton distributions of the hadron under consideration. The sum runs over all quarks, aniquarks and gluons. The scale μ_F^2 is an arbitrary *factorization scale* such that $\mu_F^2 \gg \Lambda^2$ (Λ is the QCD cut-off parameter) and defines the separation between short distance and long distance effects.
Because the structure function in equation (2.19) is an observable and cannot depend on the arbitrary factorization scale:

$$\mu_F^2 \frac{dF(x,Q^2)}{d\mu_F^2} = 0 \tag{2.20}$$

Thus the μ_F^2 dependence of C_i is exactly cancelled by that of f_i. This leads to the evolution of parton distributions:

$$\frac{df_i(x,\mu^2)}{dln\mu^2} = \sum_j \int_x^1 \frac{dz}{z} P_{ij}\left(z, \alpha_s(\mu^2)\right) f_j\left(\frac{x}{z}, \mu^2\right) \tag{2.21}$$

This equation is known as the DGLAP [12] evolution equation. The splitting function $P_{ij}(z)$ is interpreted as the probability that a parton j will emit a parton i with momentum fraction z of the parent parton. As previously explained, both the coefficient functions C_i and the splitting functions P_{ij} are computable in perturbative QCD as a power series:

$$P_{ij} = \frac{\alpha_s}{2\pi} P_{ij}^{(0)}(z) + \left(\frac{\alpha_s}{2\pi}\right)^2 P_{ij}^{(1)}(z) + ... \tag{2.22}$$

$$C_i = \alpha_s^p \left(C_i^{(0)} + \frac{\alpha_s}{2\pi} C_i^{(1)}(z) + \left(\frac{\alpha_s}{2\pi}\right)^2 C_i^{(1)}(z) + ... \right) \tag{2.23}$$

where the value of p depends on the initial process.

DGLAP equation determines how parton distributions evolve with Q^2 once they are known at some initial scale Q_0^2. Initial conditions are not provided by perturbative QCD but has to be taken from experiment. The x dependence of initial parton densities $f_i(x,Q^2)$ has to be parameterize at some low scale Q_0^2 and then we can evolve these distributions up in Q^2 to compute the cross sections or structure functions at measured (x,Q^2) points.

Leading order DGLAP equation resumes only leading lnQ^2 terms. In axial gauge [13] these terms are generated by "ladder" diagrams of the type shown in Fig. 2.2. The

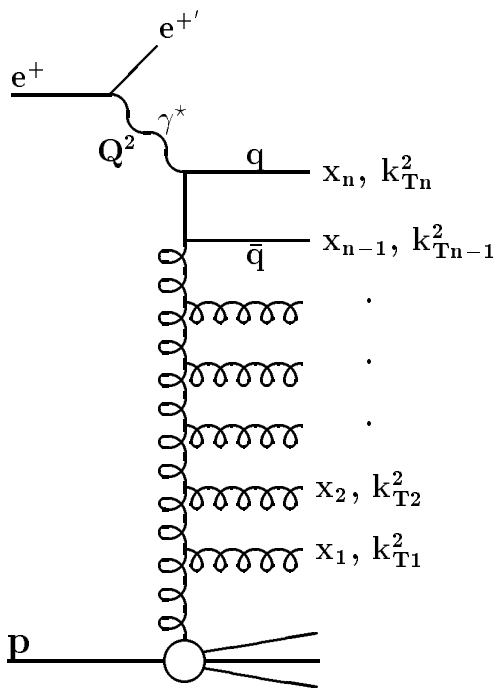

Figure 2.2: *The ladder diagram which is summed by the evolution equations.*

diagram with n rungs corresponds to the $(\alpha_s ln Q^2)^n$ contributions. In the DGLAP scheme this parton cascade follows strong ordering in the transverse momenta and weak ordering in longitudinal momenta:

$$k_{T,1} \ll k_{T,2} \ll ... \ll k_{T,n} \ll Q^2$$

$$x_n < x_{n-1} < ... < x_1$$

Use of the DGLAP evolution equation is well justified in the region of moderate x where the only large logarithms are $ln Q^2$. In perturbative calculations, for low x the other type of logarithms are important, $ln\frac{1}{x}$, and have to be resummed. For low x, gluons dominate and attention is focused on the evolution of gluon densities ($g(x, Q^2)$). DLL approximation of DGLAP equations for gluons involves the summation of the DLL contributions $\alpha_s ln Q^2 ln\frac{1}{x}$ and

$$xg(x, Q^2) \sim exp\left(2\left[\frac{3\alpha_s}{\pi} ln Q^2 ln\frac{1}{x}\right]^{\frac{1}{2}}\right) \tag{2.24}$$

This behaviour is identical with the sum of ladder diagrams where both the transverse and the longitudinal gluon momenta are strongly ordered along the ladder of Fig. 2.2:

$$k_{T,1} \ll k_{T,2} \ll ... \ll k_{T,n} \ll Q^2$$

$$x_n \ll x_{n-1} \ll ... \ll x_1$$

DDL approximation does not take into account all the leading terms in the small x limit. Terms containing the leading power of $ln\frac{1}{x}$ but not accompanied by the leading powers of lnQ^2 are neglected. The resummation of terms involving $\alpha_s ln\frac{1}{x}$ leads to the Balitskij-Fadin-Kuraev-Lipatov (BFKL) equation [15] whose kernel describes patron radiation without transverse momentum (k_T) ordering constraint:

$$-x\frac{\partial f_g(x,k_T)}{\partial x} = \frac{3\alpha_S}{\pi}k_T^2\int_{k_{T_0}^2}^{\infty}\frac{dk_T'^2}{k_T'^2}\left[\frac{f_g(x,k_T'^2)-f_g(x,k_T^2)}{\mid k_T'^2-k_T^2\mid} + \frac{f_g(x,k_T^2)}{\sqrt{4k_T'^4+k_T^4}}\right] = K_L\otimes f_g \tag{2.25}$$

where f_g is related to the integrated gluon distribution $xg(x,Q^2)$ through:

$$xg(x,Q^2) = \int_0^{Q^2}\frac{dk_T^2}{k_T^2}f_g(x,k_T^2) \tag{2.26}$$

In the leading logarithmic $\frac{1}{x}$ approximation the strong coupling constant α_s should be taken as a fixed parameter. In this approximation the gluon momentum density obtained due to the BFKL equation is expected to behave as:

$$xg(x,Q^2) \sim x^{-\lambda}, \quad \lambda = \frac{12ln2}{\pi}\alpha_s \tag{2.27}$$

In the derivation of the BFKL equation the k_T ordering is not forced but only longitudinal gluon momenta are strongly ordered along the ladder (see Fig. 2.2):

$$x_n \ll x_{n-1} \ll ... \ll x_1$$

The solution of BFKL equation leads to a non-trivial k_T structure:

$$f_g(x,k_T^2) \sim x^{-\lambda}(k_T^2)^{\frac{1}{2}}exp\left(\frac{-ln^2(k_T^2/\bar{k}^2)}{ln(1/x)}\right) \tag{2.28}$$

where $\bar{k}$ is a constant. The initial k_T distribution of the gluons is such that the k_T distribution becomes broader with a diffusion into larger and smaller values of k_T. The width of the lnk_T distribution grows like $\sqrt{ln\frac{1}{x}}$.

The presented BFKL theory was worked out in LO approximation. The NLO calculations, which have been performed recently show significant corrections [16] to the LO approach.

The increase of gluon density as x decreases cannot go on indefinitely. If the density of gluons within the proton becomes too large they can no longer be treated as free partons. The growth as $x \to 0$ must eventually be suppressed by the gluon recombination. By considering QCD Feynman diagrams which become important at small x, these $2g \to g$ recombination effects were estimated by Gribov, Levin and Ryskin(GLR) [17]. To the first approximation the normal evolution is corrected by including a quadratic term in which the gluon ladder branches into two ladders which then couple to the proton. GLR equation has the symbolic form:

$$\Delta g = P \otimes g - V \otimes g^2$$

where the extra term with minus sign reflects the suppression due to recombination or shadowing. It was established that there are interactions between gluons in the ladders, which put the validity of the GLR equation into doubts. However it appears reasonable to use an enhanced form [18] of $V \otimes g^2$ to estimate the onset of shadowing.

Phase space regions where the different evolution equations can be applied are shown in Fig. 2.3.

2.6 Parton parameterizations

In order to describe the hadronic high energy hard scattering processes it is necessary to know the individual parton distributions as a function of x and Q^2. The basic formula for a generic high energy inclusive hadronic process: $A + B \to C + X$ has the form:

$$\sigma(AB \to CX) = f_A^a \otimes \hat{\sigma}_{ab \to cX} \otimes f_B^b \tag{2.29}$$

where $\hat{\sigma}$ is the calculable hard cross section for the partonic subprocess, and $f_A^a(f_B^b)$ is the distribution function of parton a(b) in hadron A(B).

Since theory does not give absolute predictions for parton distributions, they have to be obtained from some experimental input and then DGLAP equations allow to determine those parton distributions at any Q^2. However, parton distributions are not directly measured in the experiment. It is the structure functions and hadronic cross sections that are measured.

To extract the parton distributions from the measured data, the structure functions are parameterized at some initial value Q_0^2 and then evolved numerically in Q^2 through the DGLAP equations in the kinematical regions where they are measured. A fit is then performed to determine the best values for the starting parameters. All the hard scattering hadron-hadron, lepton-lepton and lepton-hadron data are useful in the fitting procedure.

The most frequently used parameterizations of parton distributions are those of Martin, Roberts and Stirling [19] (MRS), CTEQ [11] collaboration and this of Glück, Reya, Vogt (GRV) [20].

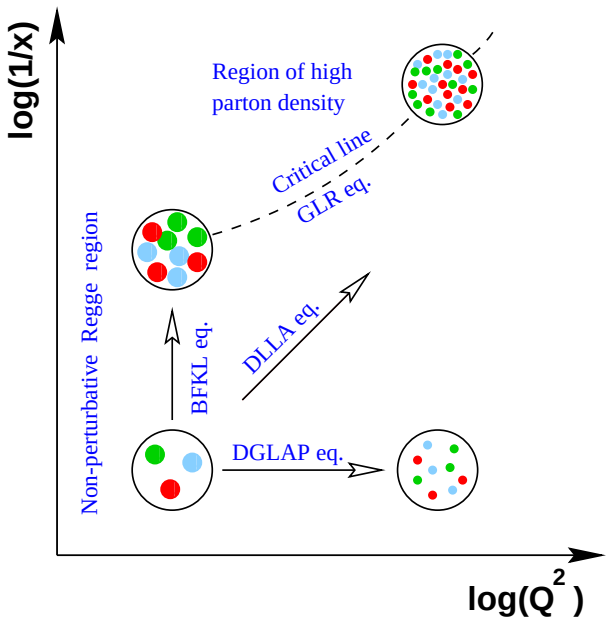

Figure 2.3: *Applicability regions of various evolution equations in* $(\frac{1}{x},Q^2)$ *plane: a) the* $LLA(Q^2)$ *region where* $\alpha_s ln Q^2 \sim 1$ *but* $\alpha_s ln\frac{1}{x}$ *is small (described by DGLAP equation), b) the* $DLLA(Q^2,\frac{1}{x})$ *region where* $\alpha_s ln Q^2 ln\frac{1}{x} \sim 1$ *but both* $ln Q^2$ *and* $ln\frac{1}{x}$ *are small (described by DLL DGLAP equation), c) the* $LLA(\frac{1}{x})$ *limit where* $\alpha_s ln\frac{1}{x} \sim 1$ *but* $\alpha_s ln Q^2$ *is small (described by BFKL equation). The critical line indicates the transition region between the dominance of gluon radiation and splitting, described by the linear evolution equations, and the saturation due to the gluon recombination and shadowing. Non-perturbative region successfully described by Regge approach is also indicated.*

2.7 Extracting of gluon density from dijet production in DIS

The gluon density distribution is of special interest at low x since it is believed that the rise seen in the structure function as x decreases is due to an increasing number of gluons.

There are two methods to extract gluon densities in proton. One is through the global QCD fits, using the inclusive DIS cross section measurement [21]. The other is a direct method in which one uses an exclusive process the cross section of which is proportional to the gluon density as eg. J/Ψ [22] or two jet production in DIS.

The electron-proton scattering cross section is a convolution of parton densities $f_q(\xi,\mu)$ (ξ is the proton momentum fraction of colliding parton, μ is the factorization scale), for quarks and antiquarks and $f_g(\xi,\mu)$, for gluons with the corresponding parton-level cross sections [23]:

$$\sigma = \int d\xi \left[f_q(\xi,\mu)\sigma_q(\xi,\mu^2) + f_g(\xi,\mu)\sigma_g(\xi,\mu^2) \right] \tag{2.30}$$

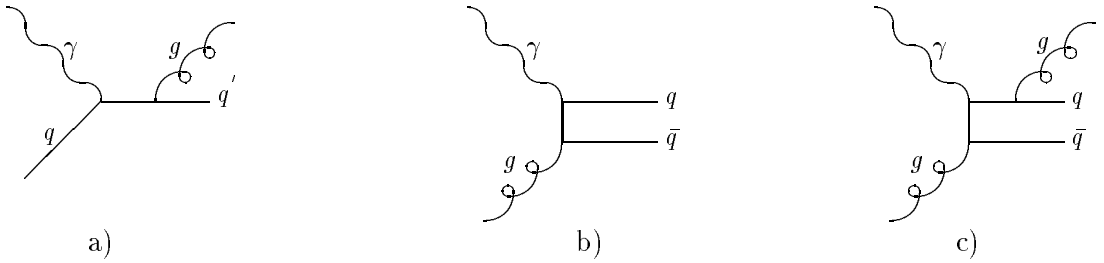

Figure 2.4: *a) QCD Compton scattering, b) boson gluon fusion and c) example of NLO real corrections.*

Besides the indicated dependence on ξ and μ, σ_q and σ_g also depend on Q^2 and momenta of the outgoing partons.

In the LO the prescription for the extraction of f_g from the cross section in DIS is intuitively clear. The parton cross sections σ_q, σ_g can be identified with the QCD Compton and BGF scatterings (Fig. 2.4.a,b). Both processes lead to two outgoing jets from the hard scattering. The calculated contribution from the Compton scattering can be subtracted from the measured cross section and thus f_g can be determined in LO by the direct unfolding, since in this case ξ can be expressed in terms of measured quantities as $\xi = x(1 + m^2/Q^2)$, where m^2 is the invariant mass squared of the dijet system. An analysis based on this method has already been made by the H1 experiment [24].

However, in LO calculation the scale dependence is particularly strong. Thus for reliable comparison with theoretical predictions a NLO analysis of gluon density is mandatory.

In the NLO approximation a hard partonic cross section is calculated with an accuracy of one order of α_s higher than in the LO approximation. In addition, corrections with one logarithm of Q^2 less accompanying α_s (NLL(Q^2) approximation) are summed in the evolution of the nucleon parton densities, what is described in Section 2.5.
In NLO aside the virtual corrections to the Born processes (see Fig. 2.4.a,b), real corrections have to be added. An example of real corrections is shown in Fig. 2.4.c. If the gluon in Fig. 2.4.c is soft or collinier to the quark, the diagram constitutes a correction to photon-gluon fusion. However if this gluon is hard and the outgoing antiquark is soft, then this configuration can be said to be a correction to the QCD Compton scattering process. In the later case, the soft antiquark forms a jet with the proton remnant. It causes that beyond the LO the variable ξ is unobservable and straightforward method described above can not be applied.

The only one way to achieve a direct determination of $f_{g/p}$ is to parameterize the $f_{g/p}$ at some initial scale and to evolve it then to the kinematical region where the cross section is measured. This procedure is repeated with different set of initial parameters to get the

best agreement between calculations and experimental data. An analysis based on this method, however in different kinematical region then studied in this thesis, has already been presented [26].

2.8 Dijet production as a probe of BFKL dynamics

With HERA ep collider we entered the new kinematical region of small Bjorken-x and Q^2 large enough for using perturbative QCD. It has been suggested that the small x region may be sensitive to the new dynamic features of QCD [27]. The ZEUS and H1 collaborations have observed that the proton structure function F_2 exhibits a strong rise with decreasing x. This rise has caused much debate on whether the HERA data are still in a regime where QCD evolution of the parton densities can be described by the DGLAP evolution equations or whether they extend into a new regime where the QCD dynamics is described by the BFKL evolution equations. Present F_2 measurements do not allow yet to discriminate between the BFKL and conventional DGLAP dynamics.
The hadronic final state may give additional information and could be more sensitive to the parton evolution mechanizm. In this context the transverse energy flow, forward jet production [27], measurement of charged particles p_T spectra [28] and NC DIS dijet production [29] can be studied to test BFKL versus DGLAP hypothesis.

In this thesis we concentrate on the NC DIS dijet production. In the lowest order approach, dijets are produced by the QCD Compton process ($\gamma p \to gq$) or by the photon gluon fusion ($\gamma p \to q\bar{q}$). The dijet events of particular interest are those in which the two jets tend to go in the virtual photon direction (in γp centre-of-mass frame) and are separated by a rapidity interval which is small relative to their large individual rapidities. In this configuration the photon-gluon-fusion process dominates and the small values of x_g (longitudinal fraction of the proton's momentum carried by the interacting gluon) are sampled.
There are two characteristic features of the solution of the BFKL equation described previously (see Section 2.5):

- the leading small x behaviour :
  $f_g(x, k_T^2) \sim x^{-\lambda}$,
- a broadening of k_T (transverse momenta of gluons) distribution with decreasing x which is a consequence of no k_T ordering along the gluon ladder.

The leading $x^{-\lambda}$ behaviour gives rise to an increase of dijet production with decreasing x. But this behaviour can be also obtained from conventional DGLAP dynamics which evolves from a singular parton distribution at some starting scale, that is $xg \sim x^{-\lambda}$.

No ordering in k_T along the gluon ladder manifests itself in a weakening of the back-to-back azimuthal correlation of the two quark jets from the top of the gluon ladder (q, $\bar{q}$

jets shown in Fig. 2.2).
As x decreases the larger k_T's are sampled and the broader azimuthal angle distributions are expected what is unique to BFKL dynamics. On the other hand the strong ordering of the gluon's transverse momenta along the ladder in DGLAP evolution leads to a narrow azimuthal angle distributions around the back-to-back jet configuration.

It should be pointed out that this effect of decorrelation is predicted in LO BFKL approximation and the NLO calculations can lead to the significant corrections.

3 Experiment

The Hadron Electron Ring Accelerator (HERA) project was approved in 1984 [30]. Operation of HERA for physics started in 1992 with two large, general purpose detectors H1 and ZEUS. Two more experiments were also approved. HERMES for the measurement of the nucleon spin structure by colliding the polarized electron beam with the polarized nucleons and HERA-B which aims at measuring CP violation in $b\bar{b}$ production by scattering beam protons on a fixed target.
The HERA accelerator and the ZEUS detector are described below in more details.

3.1 HERA collider

The word's first electron-proton collider HERA is located at DESY in Hamburg. The layout of HERA is shown in Fig. 3.1. It was designed to study the interaction between electrons and protons in the head-on collision at a center of mass energy of about 300 GeV. Two separate magnet systems guide the beams around the 6.3 km long ring. The proton ring uses superconducting magnets and stores 820 GeV protons. The electron ring uses conventional magnets to store 30 GeV electrons. The main design characteristics together with operational ones in 1995 are listed in Table 3.1.

The injection scheme of HERA is shown in Fig. 3.2. The proton injection starts with negative hydrogen ions (H^-) from the 50 MeV Proton Linac, followed by acceleration in

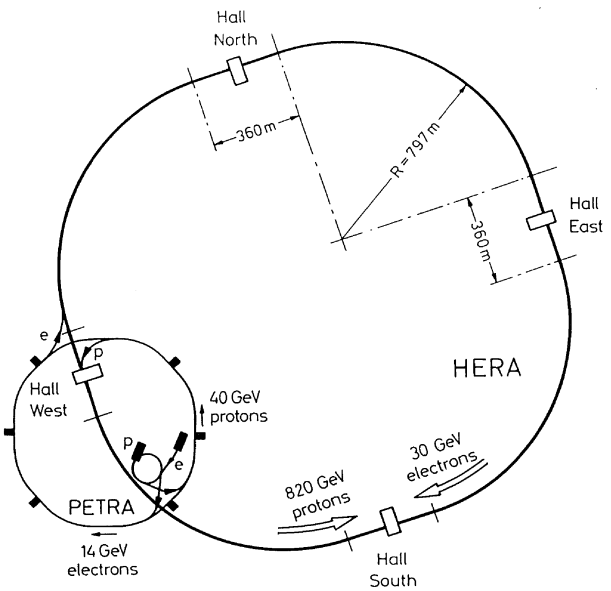

Figure 3.1: *Layout of HERA accelerator.*

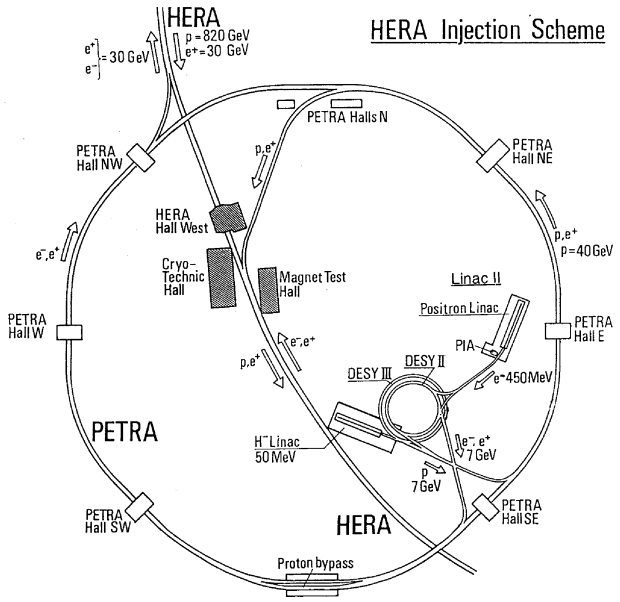

Figure 3.2: *The HERA injection system.*

HERA parameters	designed values		1995	
	electron	proton	electron	proton
Circumference (m)	6336			
Nominal Energy (GeV)	30	820	27.52	820
C.M. Energy (GeV)	314		300	
Specific luminosity ($cm^{-2}s^{-1}mA^{-2}$)	3.6×10^{29}		5.0×10^{29}	
Instantaneous luminosity ($cm^{-2}s^{-1}$)	1.6×10^{31}		4.3×10^{30}	
Magnetic Field (T)	0.165	4.65	0.165	4.65
Injection Energy (GeV)	14	40	12	40
Filling Time (min)	15	20	45	60
Circulating Current (mA)	58	163	30	55
Number of Bunches	210		174+15	174+6
Time between Crossings (ns)	96			
Horizontal Beam Size σ_x (mm)	0.301	0.276	0.239	0.185
Vertical Beam Size σ_y (mm)	0.067	0.087	0.055	0.058
Longitudinal Beam Size σ_z (cm)	0.8	11	0.8	11

Table 3.1: *Design and operational(1995) values of the main HERA parameters.*

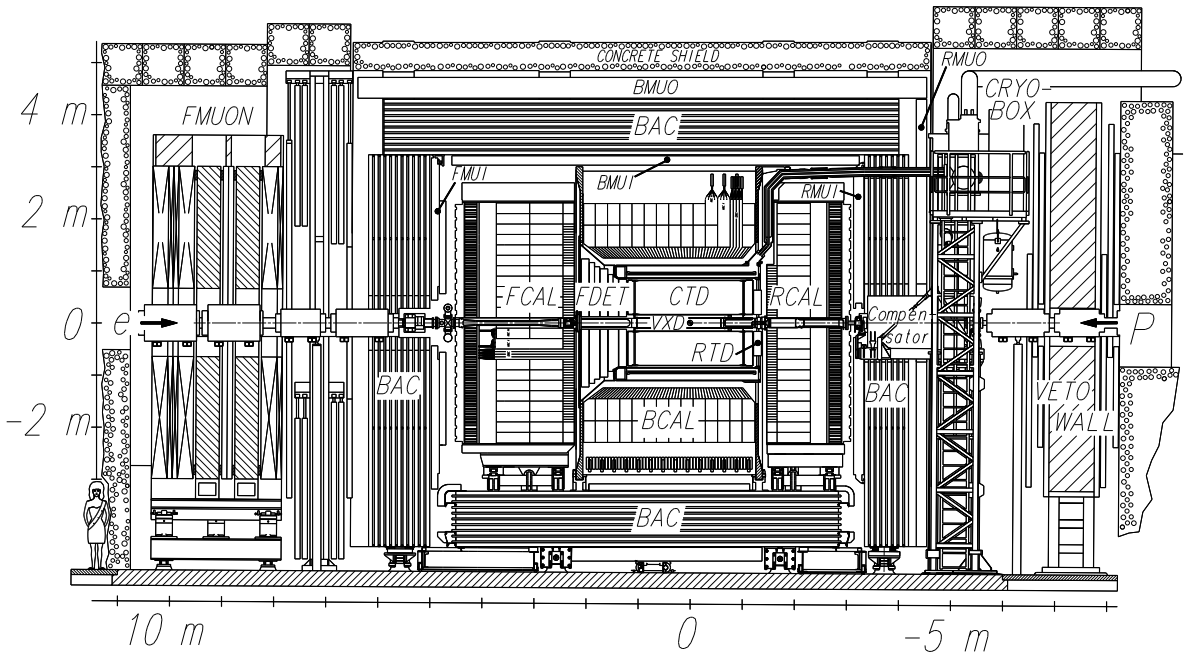

Figure 3.3: *Section of the ZEUS detector along the beam.*

the proton synchrotron DESY III to 7.5 GeV. From there the protons are transfered to the PETRA ring where they are accelerated to the energy of 40 GeV and then injected into the HERA proton storage ring.
The electrons or positrons are pre-accelerated first in a linear accelerator, LINAC I (220 MeV, e^-) or LINAC II (450 MeV, e^+) and at the DESY II synchrotron to 7.5 GeV. Then the particles are injected via PETRA at an energy of 14 GeV into the HERA electron storage ring.
Acceleration of protons to 820 GeV and electrons to 30 GeV takes place in the HERA rings.

3.2 ZEUS detector

The ZEUS detector [31] is a multipurpose detector designed to achieve the best measurement of products of *ep* reactions. The main components of the ZEUS detector are shown in Fig. 3.3 and Fig. 3.4. It is asymmetric along the beam direction, to account for the boosted center-of-mass for ep collisions at HERA. The direction of the proton beam defines the positive z axis, the positive y axis points upwards and the positive x axis points towards the center of the HERA ring.
Below, the main components of the ZEUS detector are described.

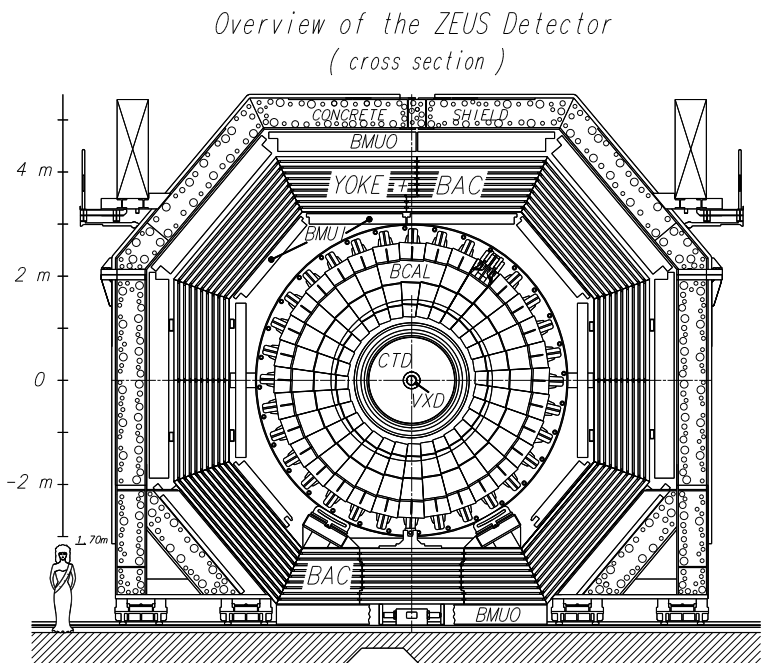

Figure 3.4: *Section of the ZEUS detector perpendicular to the beam.*

3.2.1 Tracking system

The tracking system of ZEUS is located inside the superconducting solenoid [32]. It consists of different tracking detectors: the Vertex Detector (VXD) (not installed in '95 running period), the Central (CTD), Forward (FTD) and Rear Tracking Detectors (RTD) and the Transition Radiation Detector (TRD) and are dedicated to charged particle detection.

The primary tasks of the VXD are the detection of the short-lived particles by reconstructing secondary vertices, and the improvement of the momentum and angular resolution of charged particles. It is a high precision drift chamber [33], which covers the angular region $8.6° < \theta < 165°$.

The Central Tracking Detector (CTD) is used to reconstruct the direction and momentum of charged particles in the angular region $15° < \theta < 164°$ [34]. It consists of 72 cylindrical drift layers arranged into 9 super-layers as shown in Fig. 3.5. The odd-numbered "axial" layers have wires strung parallel to the beam, while the four even-numbered "stereo" layers have wires tilted by a small angle to enable determination of the z-position of the hits.

Additional tracking detectors (FTD, RTD) are located in the forward and the rear directions with respect to the interaction region. FTD consists of 3 planar drift chambers

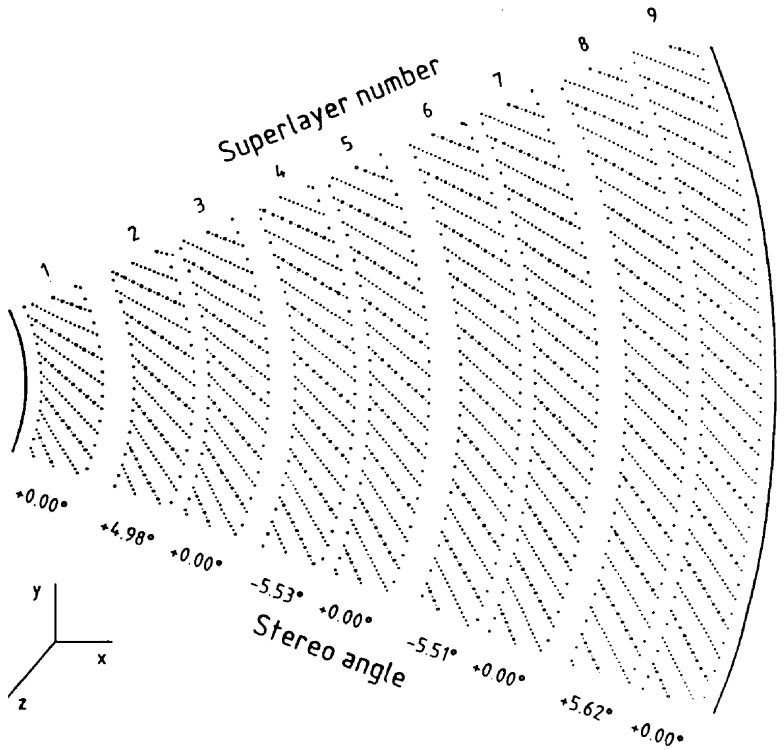

Figure 3.5: *Layout of an octant of the CTD. Sense wires are indicated by larger dots. The superlayer numbering convention and stereo angle of wires within the superlayer is also shown.*

and extends the tracking region in forward direction down to 7.5° and covers the angular region $7.5° < \theta < 28°$, where the high particle rates are expected. The 3 FTD chambers are separated by the TRD, which was optimized to allow a hadron/electron separation on the basis of transition radiation created by charged particles passing the boundary of two materials with different dialectric constants.
The RTD consists of one planar drift chamber covering an angle of $160° < \theta < 170°$. Each of the chambers of the RTD and FTD consists of three layers of drift cells perpendicular to the beam axis with fixed wires orientations of 0°, 60°, −60°.

The tracking chambers are filled with gas mixtures which molecules are ionized by the charged particle as it passes through. The ionization electrons drift in the electric fields of the cells and the avalanche of ionization particles which occurs near the sense wires causes an electric pulse which indicates that the wire has been hit. The pattern of hits and drift times are then used to reconstruct the path of the charged particle.

The central tracking region is enclosed in a superconducting solenoid, which provides magnetic field of about 1.8 T enabling measurement of charged particles momenta. To compensate for the influence of it's magnetic field on the beams an additional supercon-

ducting solenoid (compensator) was constructed, which creates the same but opposite field.

3.2.2 Calorimeter

The calorimeter encloses the inner tracking detectors and the superconducting solenoid, as shown in Fig. 3.3. It consists of three main components:

- Forward Calorimeter (FCAL) ($2.2° < \theta < 39.9°$)
- Barrel Calorimeter (BCAL) ($36.7° < \theta < 129.1°$)
- Rear Calorimeter (RCAL) ($128.1° < \theta < 176.5°$)

FCAL and BCAL are segmented (FCAL along and BCAL perpendicular to the beam direction) into three sections, an electromagnetic (EMC) with 1 interaction length (λ) and two hadronic sections (HAC1, HAC2) with a depth of 3.1λ each in the FCAL and with a depth of 2.1λ each in BCAL. The RCAL is divided longitudinally into two sections, one EMC (1λ) and one HAC (3.1λ).
The modular structure of FCAL as seen from the interaction point is shown in Fig. 3.6. The sampling in all calorimeter is the same: 3.3mm depleted uranium plates (DU) ($1X_0$) and 2.6mm scintillator plates. The DU plates are clad with 0.2mm (EMC) and 0.4mm (HAC) steel foils for ease of handling and reduction of noise from the radioactivity of the uranium, while the scintillator is wrapped in white Tyvek paper. The light from the scintillators is transported by plastic wavelength shifter plates (WLS), light guides and read by photomultipliers.

The particles entering the calorimeter interact with DU and initiate a shower of particles. A charged particle from this shower produces in the scintillator light which propagates to wavelength shifters (WLS) where it is converted to the light of a longer wavelength. From WLS light propagates to photomultipliers, where it is converted into electrical signal.

The ZEUS uranium calorimeters are so called compensating calorimeters i.e. they give the same signals for electrons and hadrons of equal energy. The compensation of incident hadron's energy loss for the breakup of the heavy nucleus is possible through the use of depleted uranium and plastic scintillator. A fraction of the shower energy results in production of spallation neutrons in depleted uranium which undergo elastic np scattering on free hydrogen atoms in the plastic scintillator. The recoil protons produce light in the scintillator by ionization thereby compensating for some of the lost energy. The thickness of the uranium and scintillator plates is tuned such that the energy gained from the np scatters equals the lost binding energy.
In this way for all jets of the same energy the same signal is produced irrespective of their

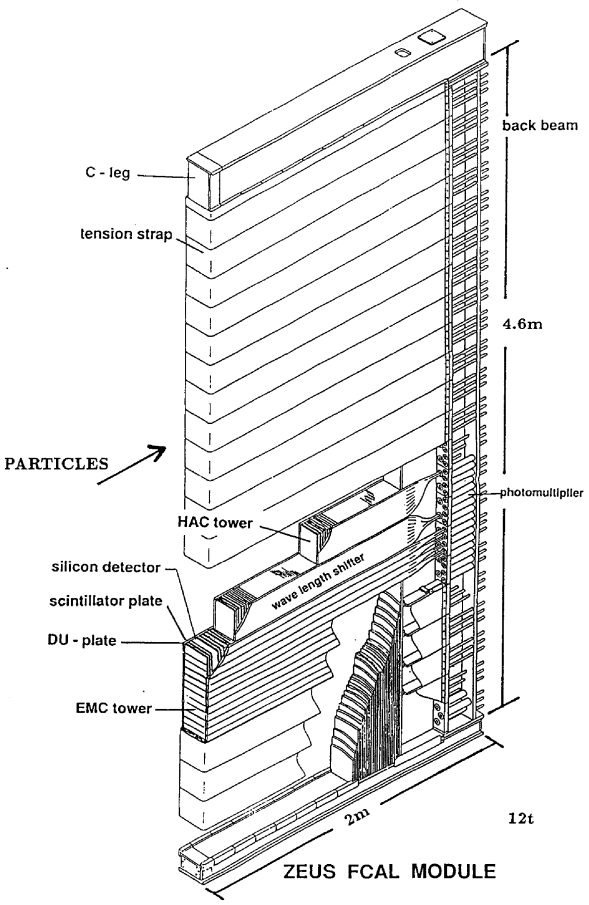

Figure 3.6: *Layout of a ZEUS FCAL module. The module is partitioned into towers of 20×20 cm^2 having three sections, an electromagnetic section EMC and two hadronic sections, HAC1 and HAC2.*

electromagnetic and hadronic composition. A compensating calorimeter gives the best energy resolution for hadrons. In ZEUS this amounts to $35\%/\sqrt{E(GeV)} \oplus 2\%$.

Hadron Electron Separator (HES) is installed in gaps situated after the 4-th and 7-th scintillator layers in FCAL and after the 4-th scintillator layer in BCAL and FCAL. HES consists of two planes of Si diodes and significantly improves identification of electrons compared to the calorimeter alone. This identification is possible due to the different development of electromagnetic and hadronic showers in the calorimeter. At the depth the HES is positioned electromagnetic showers (initiated by e or γ) give a large signal, while hadrons, which typically interact at greater depths, behave like minimum ionizing particles in the HES [35].

3.2.3 Other components

Below, for completeness, are described other components of ZEUS detector.

The Small angle Tracking Detector (SRTD) is installed in the region around the RCAL beam pipe [36]. The active part of the SRTD consists of arrays of scintillator strips. The SRTD consist of 4 quadrants, $24cm \times 44cm$. Each quadrant contains two layers of scintillator strips arranged in orthogonal directions. The SRTD improves measurement of charged particles and electrons, which is essential in the proper reconstruction of event kinematics.

For correction of energy measured in the calorimeter due to showering in dead material between the interaction point and calorimeter the Presampler was constructed [37]. Two scintillator walls have been installed in front of FCAL and RCAL and are used to correct the measured energies both of electrons and jets.

The Backing Calorimeter measures the hadron shower leaking out of the main calorimeter and acts as a veto counter selecting precisely measured events fully contained in the uranium calorimeter.

An important element of QCD studies and the search for new physics at HERA is lepton identification. In addition to electron identification provided by the tracking system and the calorimeter it is essential to have muon identification, which is achieved by the muons detectors (FMUON,BMUON,RMUON).

The Leading Proton Spectrometer (LPS) allows measurement of forward scattered protons with transverse momentum $p_T < 1GeV/c$ and momenta $p/p_{beam} = 0.3 - 1.0$.

The vetowall (VETO) shields the detector from the proton beam halo particles and also vetos beam-gas interactions.

C5 beam monitor is used to reject proton beam-gas events and to measure the beam arrival time.

The Beam Pipe Calorimeter (BPC) was installed behind the RCAL (at z=-300cm) (not shown in the Fig. 3.3) to catch electrons scattered through small angles, which escape through the beam hole in RCAL. It allows measurement of Q^2 down to $0.1GeV^2$

The Proton Remnant Tagger (PRT) consists of 7 pairs of rectangular scintillation counters surrounding the forward beam pipe and is used to detect highly energetic charged particles that escape the central detector.

To detect neutrons produced in the proton beam direction the FNC (Forward Neutron Calorimeter) is installed (at z=105 m). The FNC accepts neutrons produced at angles less then 7 mrad.

3.2.4 Luminosity monitor

The main task of the Luminosity Monitor (LUMI) is a precise measurement of the luminosity [38].

The luminosity is defined by the formula:

$$L = \frac{R}{\sigma} \tag{3.1}$$

where L is the measured luminosity, R is the event rate of the process with cross section σ. This formula can be used for luminosity measurement provided that the cross section σ is well known and process can be precisely measured in experiment. For luminosity measurement at HERA the bremsstrahlung process $ep \to ep\gamma$ was chosen. The differential cross section for bremsstrahlung, in the Born approximation, is given by the Bethe-Heitler formula [40]:

$$\frac{d\sigma_{bh}}{dE_\gamma} = 4\alpha r_e^2 \frac{E'_e}{E_\gamma E_e}\left(\frac{E_e}{E'_e} + \frac{E'_e}{E_e} - \frac{2}{3}\right)\left(ln\frac{4E_p E_e E'_e}{MmE_\gamma} - \frac{1}{2}\right), \tag{3.2}$$

where:
E_γ - photon energy,
E_e, E'_e - energy of primary and secondary electrons,
E_p - proton energy,
M, m - proton and electron masses,
α - fine structure constant,
r_e - classical electron radius.

The layout of the LUMI is shown in Fig. 3.7. The LUMI consists of two detectors: an electron and a photon detector. The photon detector is placed at a distance 104 m from the interaction point close to the proton beam pipe. The electron detector is placed about 35 m from the interaction point close to electron beam pipe behind the bending magnet BH04, which acts as electron spectrometer for off beam energy electrons. Both detectors consist of one calorimeter (with resolution of $18.5\%/\sqrt{E(GeV)}$) and one position detector (which consists of two layers of horizontal and vertical scintillator fingers). In the experiment we observe bremsstrahlung of beam electrons on protons and gas molecules as well. The second process is the most severe experimental background. This background is statistically subtracted using electron bunches without proton counterpart, so called pilot bunches.

The ep rate (R_{ep}) obtained from the total rate of bremsstrahlung events after corrections for the electron-gas is:

$$R_{ep} = R_{tot} - kR_{pilot} \tag{3.3}$$

where R_{tot} denotes the total rate of observed bremsstrahlung events, R_{pilot} is the rate measured from the pilot bunches and k is the ratio of the total current in all the bunches to that in the pilot bunches.

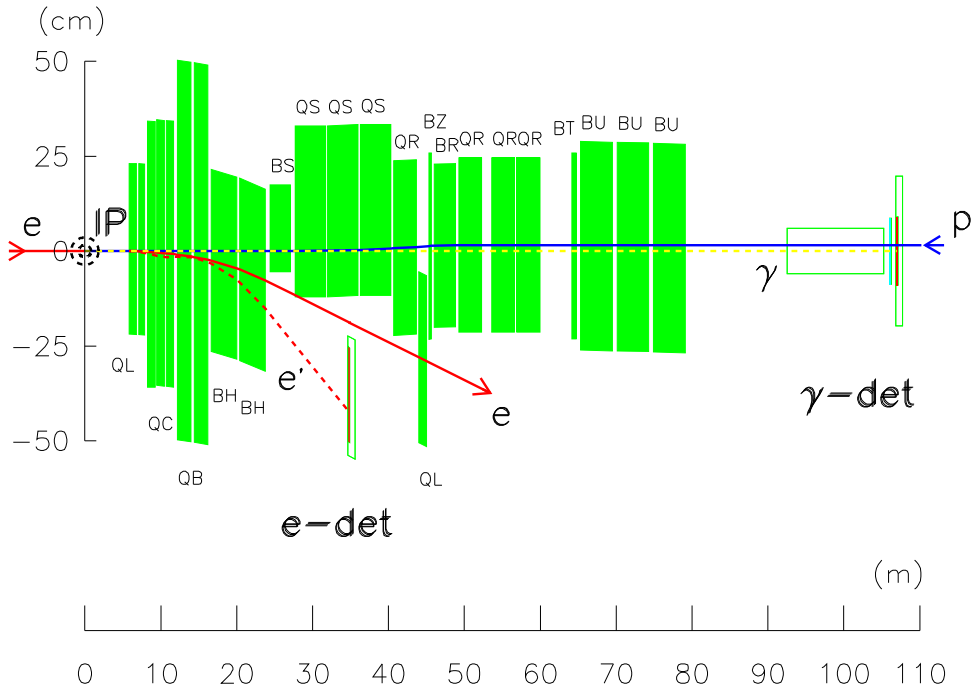

Figure 3.7: *Layout of the luminosity detectors.*

The observed cross section is the bremsstrahlung cross section corrected for the acceptance of the LUMI detector:

$$\sigma_{obs} = \int A_{lumi} d\sigma_{bh} \tag{3.4}$$

where A_{lumi} is LUMI acceptance and integration is over the whole relevant range of photon four-momenta.

The luminosity L measured in experiment is given by the formula:

$$L = \frac{R_{ep}}{\sigma_{obs}}. \tag{3.5}$$

For luminosity determination photons within the energy range 10 - 16 GeV were used. However, for systematic checks these cut values were changed.
The observed cross section, σ_{obs} (formula (3.4)), is subject to the errors [39] in the calculation of the theoretical cross section for flagged bremsstrahlung events, the errors in the photon acceptance determination and the energy scale errors.

The rate, R_{ep} (formula (3.3)), is subject to the errors made in e-gas background subtraction (factor k), in the correction due to the multiple bremsstrahlung contribution and in flagging of bremsstrahlung events.

Since all the contributions are independent, errors can be summed up in quadrature resulting in a 1.1% total systematic error of the luminosity measurement.

3.3 ZEUS trigger system

The electron and proton bunches collide at HERA every 96ns (or at the rate of 10MHz). The ZEUS trigger system has the task of selecting interesting events and rejecting background for study of ep physics. The main types of background are proton beam-gas interactions, proton beam halo events and cosmic particle induced events. The short time between bunch collisions requires an innovative approach to the triggering and the data acquisition. To minimize dead time and to reduce the rate of accepted events to the level of a few Hz ZEUS has worked out a three level pipeline system [41], the flow diagram of which is shown in Fig. 3.8.

The First Level Trigger (FLT) is a hardware trigger, designed to reduce the input rate below 1kHz. Each detector component has its own FLT, which stores the data in a pipeline and makes a trigger decision between $1\mu s$ and $2.5\mu s$ after the bunch crossing. The decision from the local FLT's are passed to the Global First Level (GFLT). The GFLT calculations take a minimum of $1.9\mu s$ additional time after receiving information from the individual components. The GFLT is issued exactly $4.4\mu s$ after the crossing that produced it [43].

If the event is accepted, the data are transferred to the detector component Second Level Trigger (SLT), which is software based, runs on a network of programable transputers and reduces the rate to below 100 Hz. The sophisticated algorithms are used to identify and reject background events. The results of the local (component) SLT's are combined in the Global Second Level Trigger (GSLT) [42] to execute a final decision.

Once the positive decision of the GSLT has been issued, the data from each component is sent to the Eventbuilder to combine the component data into one single data set. The Eventbilder makes the event information accessible to the Third Level Trigger (TLT) and formats the components data in the ADAMO tables, which are used in the off-line reconstruction and analysis.

The TLT is software based and runs part of the off-line reconstruction code on a farm of Silicon Graphics CPUs. It is designed to reduce the event rate to a few Hz. Events which are accepted by the TLT are written to tape and can be used for off-line analysis.

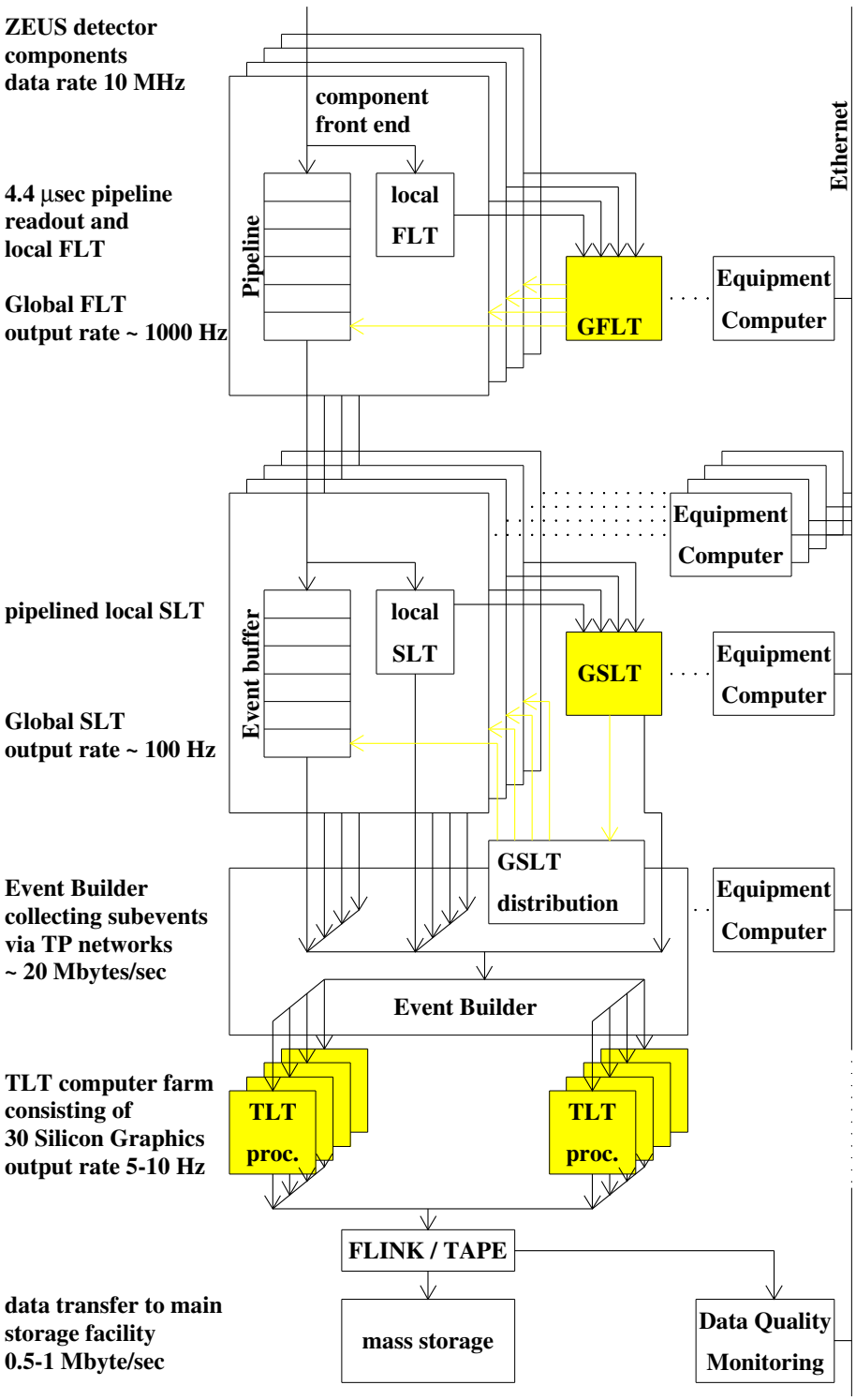

Figure 3.8: *Outline of the ZEUS trigger and data acquisition.*

4 Monte Carlo simulation

The Monte Carlo (MC) simulation of the observed data is a powerfull tool which allows one to make a direct comparison between the theory and the experiment. Here the MC programs are used to generate events according to the chosen theoretical models and to simulate the detector response to the generated particles. Fig. 4.1 shows schematically the data taking and MC simulation chains in ZEUS experiment at HERA.

The output from the event generator consists of a list of the final state particles and their momenta, generated according to a specific theoretical model. The events are then passed through the ZEUS detector simulation program MOZART [31] which uses the GEANT [44] simulation package. The output is in ADAMO [45] data format, identical to that of ZEUS data. ADAMO provides a way of defining tabular data structures and allows their manipulation. After full simulation of the detector response the output from MOZART is fed into the ZGANA [46] program for a simulation of the trigger logic, so that MC events can be treated in the same way as data. Selection cuts are applied off-line by the different physics groups, and events are flagged if they pass the selection criteria of a physics filter. Events can be quickly then picked out to produce Data Summary Tapes (DST) for the different physics groups.

To compare the theoretical predictions with the experimental data the different MC models were formulated on the basis of QCD. In the following section we describe those which are used in this thesis.

4.1 Monte Carlo models

The hard lepton-quark scattering process is well theoretically understood in leading order QCD approximation, however in order to describe the hadronic final state in DIS scattering it is necessary to include the higher order QCD corrections as well as the parton

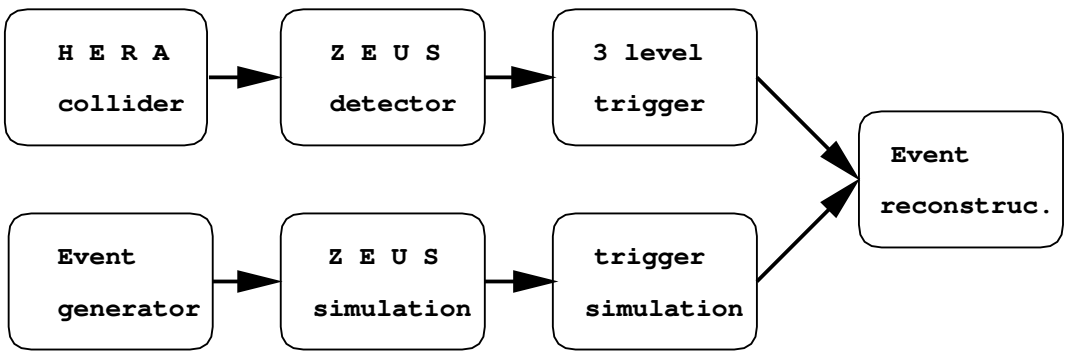

Figure 4.1: *Overview of the data and MC simulation chains in the ZEUS experiment.*

hadronization, description of which is only phenomenological. This results in a variety of theoretical models which aim to describe the distributions observed in DIS.

The event generation is performed in three stages:

- the cross section of the hard scattering process is calculated using an exact matrix element. Parton distributions in the proton are provided separately;
- calculation of the higher order corrections is made (based on theoretical models);
- hadronization of partons is included using a phenomenological prescription.

In this analysis we have used the following MC programs:

- Lepto [47], which describes the QCD processes using the exact first order matrix elements (ME). It covers processes:
  - the leading order photon absorption, $\gamma q \to q$, at parton level,
  - gluon radiation (QCD Compton), $\gamma q \to qg$,
  - boson gluon fusion (BGF), $\gamma g \to qq$.

  The higher order processes are simulated in the leading logarithmic approximation by the parton shower (PS) models [48].
- Ariadne [49], which is only a generator of QCD cascades using the Color Dipole Model (CDM). In this model the gluon is emitted from the dipole formed by the struck parton and the proton remnant. Further emission can occur between dipoles formed from the gluon and struck quark and the gluon and proton remnant, etc.
- Jetset [50]. The final state quarks and gluons are combined to form colourless hadrons using the Lund string model [51]. According to this model, as the struck quark moves away from the proton remnant, the colour flux string is being stretched between the participating partons. As the potential energy stored in the string increases with increasing stretching the string may break into shorter fragments and the hadrons are formed by partons from adjacent breaks. A large fraction of the particles produced by fragmentation are unstable and subsequently decay into stable ones. The fragmentation and the decays are described in a phenomenological approach given by Jetset.
- Django [52]. The event generator Django simulates deep inelastic lepton-proton scattering including both QED and QCD radiative corrections. Django is an interface between MC programs Heracles [53] (describing QED corrections) and Lepto (Ariadne). Complete hadronic final state is obtained by using the Lund fragmentation model, as implemented in Jetset.

- Herwig [54]. In the Herwig MC the QCD cascade is modelled using the parton showers alone. For the nonperturbative hadronization a cluster model [55] is used instead of string fragmentation.

- Mepjet [56]. The NLO MC Mepjet allows to study the jet cross section for arbitrary jet identification algorithms in DIS. Since Mepjet provides only the exact perturbative QCD calculations up to NLO, then only the parton level cross sections are available.

5 Reconstruction of the kinematical variables

A precise reconstruction of the kinematical quantities x, y, Q^2 is crucial for the physics analysis. In this section we present the different methods used for calculation of kinematical variables and their resolutions.

5.1 Reconstruction methods

In the NC DIS events kinematic variables can be determined either from the energy and the angle of the scattered electron, or from the final state hadron system, or from a mixture of both.

For definition of the variables we use the following notation:

E_e	–	Energy of the initial electron
$E_e^{'}$	–	Energy of the final electron
E_p	–	Energy of the initial proton
s	–	Square of the total center mass energy
θ_e	–	Angle of the scattered electron

Electron method
In this method variables are calculated from the energy and angle of the scattered electron.

$$y_{elec} = 1 - \frac{E_e^{'}}{2E_e}(1 - \cos\theta_e) \tag{5.1}$$

$$Q^2_{elec} = 2E_e E_e^{'}(1 + \cos\theta_e) \tag{5.2}$$

$$x_{elec} = \frac{E_e}{E_p}\frac{E_e^{'}(1 + \cos\theta_e)}{2E_e - E_e^{'}(1 - \cos\theta_e)} \tag{5.3}$$

Jacquet-Blondel(JB) method
The JB method [57] uses only hadron variables and can be determined by summing the energies(E_h), transverse(p_{x_h}, p_{y_h}) and longitudinal (p_{z_h}) momenta of the final state particles. It is based on the assumption that the total transverse momentum of hadrons which escape through the beam hole in the proton direction and the energy carried by the particles escaping through the hole in the electron direction can be neglected.

$$y_{JB} = \frac{\sum_h (E_h - p_{z_h})}{2E_e} \tag{5.4}$$

$$Q^2_{JB} = \frac{(\sum_h p_{x_h})^2 + (\sum_h p_{y_h})^2}{1 - y_{JB}} \tag{5.5}$$

$$x_{JB} = \frac{Q^2_{JB}}{s y_{JB}} \tag{5.6}$$

where summation is over all the calorimeter cells.

Double angle method
In the double angle method [58] kinematic variables are reconstructed using the angle θ_e of the final state electron and angle γ of the final state hadron flow, respectively. The angle γ of the current jet is obtained from the hadronic flow measurement.

$$\cos\gamma = \frac{(\sum_h p_{x_h})^2 + (\sum_h p_{y_h})^2 - (\sum_h (E_e - p_{z_h}))^2}{(\sum_h p_{x_h})^2 + (\sum_h p_{y_h})^2 + (\sum_h (E_e - p_{z_h}))^2} \tag{5.7}$$

From conservation of energy, longitudinal and transverse momentum, the energy of the scattered electron can be also expressed in terms of scattering angles (θ_e, γ):

$$E_e^{'} = \frac{2E_e \sin\gamma}{\sin\theta_e + \sin\gamma - \sin(\theta_e + \gamma)} \tag{5.8}$$

Using the angle γ and (5.8) the variables in the electron method can be redefined:

$$y_{DA} = \frac{\sin\theta_e(1 - cos\gamma)}{\sin\gamma + \sin\theta_e - \sin(\theta_e + \gamma)} \tag{5.9}$$

$$Q^2_{DA} = 4E_e^2 \frac{\sin\gamma(1 + \cos\theta_e)}{\sin\gamma + \sin\theta_e - \sin(\theta_e + \gamma)} \tag{5.10}$$

$$x_{DA} = \frac{E_e}{E_p} \frac{\sin\gamma + \sin\theta_e + \sin(\theta_e + \gamma)}{\sin\gamma + \sin\theta_e - \sin(\theta_e + \gamma)} \tag{5.11}$$

5.2 Smearing and migration effects

The inaccuracy in the measurement of kinematic variables x, y, Q^2 is the consequence of the finite granularity and resolution of the calorimeter. Even though these effects can be corrected using Monte Carlo, the uncertainty of these corrections can become large. As an example in Fig. 5.1 is shown the comparison of reconstructed and generated variables for Ariadne MC, after all NC DIS dijet selection cuts were applied (see Section 6), for the three presented reconstruction methods.

For the electron method, all kinematic variables are well reconstructed, whereas for the double angle method the reconstruction is worse although still reasonable. In the Jacket-Blondel method only y_{JB} reconstruction is good, the best from all methods.
Since the electron method gives the best estimation of generated variables it was chosen for dijet events kinematic reconstruction.

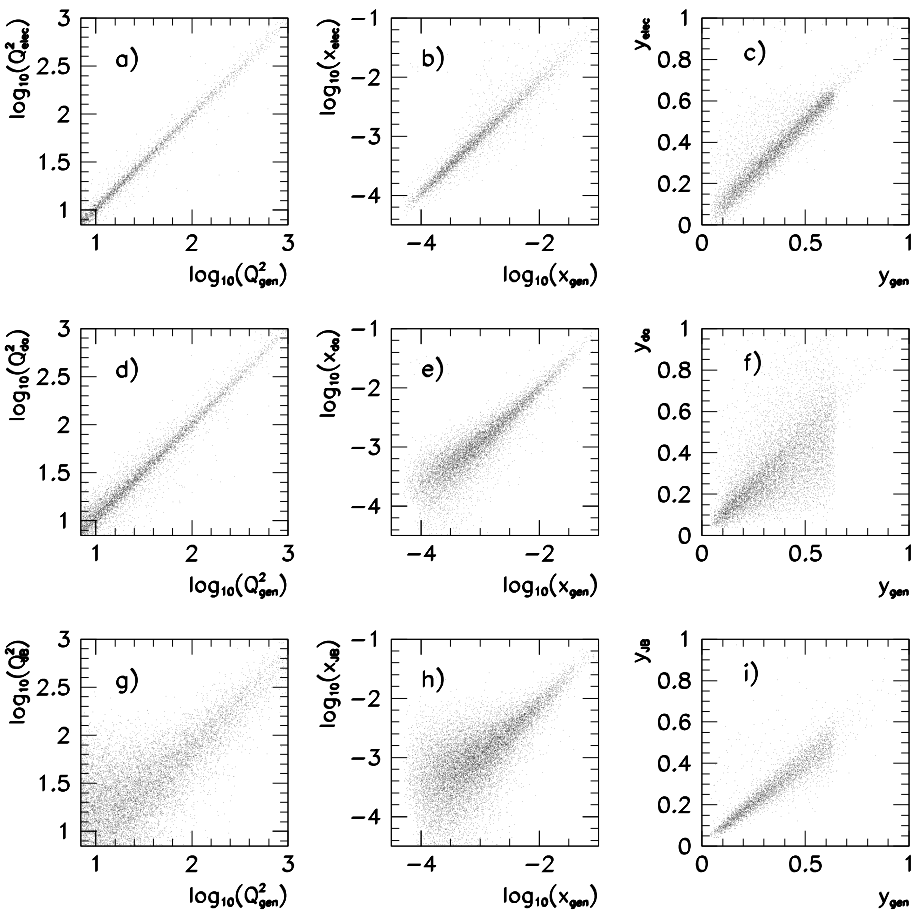

Figure 5.1: *Q^2, x, y reconstructed versus generated, for Ariadne MC, after all NC DIS dijet selection cuts were applied (see Section 6). All three discused reconstruction methods are presented: a-c) electron method, d-f) double angle method, g-i) Jacket-Blondel method.*

6 Event selection

In this section we discuss the NC DIS dijet event selection. During the 1995 running period an integrated luminosity of 8.2 pb^{-1} was collected by the ZEUS detector and over 6.1 pb^{-1} events passed DIS DST (Data Summary Tapes) selection. However, only a small part of these events are indeed neutral current dijet DIS events and were interesting for this analysis. The aim of the selection cuts is to reduce the background and to define a sample of NC DIS dijet events. The selection procedure consists of several stages from the on-line trigger to the final off-line event selection.
In this section we describe the data selection steps, cuts applied, jet finding procedure and all the background sources.

6.1 On-line DIS trigger

The presence of electron in the final state is the main characteristic of a DIS event. The three stages of the DIS trigger are almost entirely based on the identified electron signal in the calorimeter. A reasonable electron identification relies on the following logic.

- At the first level trigger (FLT) the calorimeter trigger allowes the definition of several logical bits which indicate the presence of energy deposits in electromagnetic or hadronic section:
  - the REMC (RCAL electromagnetic (EMC) energy) trigger requires that the total electromagnetic energy deposit in RCAL is greater than 3.4 GeV, excluding the trigger towers next to the RCAL beamhole,
  - the BEMC (BCAL EMC energy) trigger requires that the total electromagnetic energy in the BCAL is greater than 4.8 GeV,
  - the RMECth (RCAL EMC threshold, which is essentially total RCAL EMC energy, but with a worse resolution) trigger reads the entire RCAL electromagnetic section and requires that deposit is greater than 3.75 GeV,
  - the RCAL-IsoE (RCAL isolated electron) trigger searches for energy deposits originating from the isolated electrons or muons in the RCAL. It requires a single or group of up to 4 trigger towers, with electromagnetic or minimum ionization energy deposits, to be surrounded by the quiet trigger towers,

  The satisfaction or denial of any of the above conditions are stored in the bits which form the trigger slots.
- At the second level trigger (SLT), global vetos like timing, spark and halo muon rejection are added and the following quantity is calculated:

$$\delta \equiv E - P_z = \sum_i E_i - P_{z,i}$$

where E and P_z are the total energy and the total longitudinal momentum in an event. $E_i, P_{z,i}$ are energy and longitudinal momentum of the final state particles. Since for forward moving particles (positive ZEUS z-direction), the energy and longitudinal momentum are practically identical their contribution to δ cancels. For particles moving in the rear direction the energy and longitudinal momentum have opposite signs and their contribution is expected to peak at twice the electron beam energy (55.04 GeV) for DIS events. For photoproduction events the contribution to δ from the undetected electron is missing, results that it peaks much below twice the electron beam energy.
In the case of initial state radiation (ISR) events, the initial electron energy (E_e) is lowered to $E_e - E_\gamma$, where E_γ is the energy of the real photon which is emitted from initial state electron and could be tagged in the luminosity monitor.
In order to account for ISR, where a significant fraction of the event $E - p_z$ can be carried down the proton beam pipe by the radiated photon, a SLT cut is imposed on the quantity:

$$E - P_z + 2 * E_\gamma$$

instead of $E - P_z$.

- At the third level trigger (TLT), in addition to FLT and SLT trigger requirements an electron has to be found with energy above 4 GeV, using the ELEC5 [59] or the LOCAL [60] electron finder.

6.2 Off-line data selection

For the events accepted and written to tape, a full reconstruction is performed with the physics reconstruction program ZEPHYR [61]. First data from individual components like the calorimeter, tracking chambers and the luminosity detector are reconstructed [62], then matching between components (eg. matching of calorimeter cells and CTD tracks) is performed and finally particles are identified from combined components data. Results are stored in ADAMO tables and can be easly accessible in a physics analysis.

Using full information of the event after reconstruction the additional cuts should be applied to improve data selection. After these off-line selections the Data Summary Tape (DST) bits are set, which allow an assignment of the event to the specific event classes.

For the analysis presented in this thesis the events have to satisfy the following requirements:

- The event has to pass medium Q^2 branch (DIS03 [63], which was unpreselected during the whole running period) of Neutral Current Third Level Trigger (TLTNC) selection [63].

- Sparks are caused by discharges between calorimeter photomultiplier (PMT) and its shielding. Spark events are characterized by a large imbalance of the 'electron' calorimeter cell, as only one of two PMT's produces a signal. Therefore these events can be easily identified and removed. It is done in the subroutine RMSPARK [64].

- Muons originating from the upstream proton beam-gas interactions as well as cosmic muons can emit a photon via the bremsstrahlung process, which leads to an energy deposit in the electromagnetic section of calorimeter. These deposits can be falsely identified as electrons. The routine MUTRIG [64] for cosmic and the routine ALHALO2 [64] for halo muon rejection are used. Muons are identified by characteristic energy deposits in the calorimeter and by special time signatures.

- The moment of which the particle hits a calorimeter cell is extracted from the PMT information. An energy weighted average of the times of all cells in a particular calorimeter section (FCAL,BCAL,RCAL) yields the total time of this section (t_F, t_B, t_R). The time offset of each individual PMT is adjusted so that the calorimeter cell time equals zero for interactions originating at the nominal interaction point and at nominal bunch crossing time. The calorimeter timing is used to remove upstream beam-gas interactions, since for the proton beam-gas interaction the final particles reach the RCAL earlier than FCAL, whereas for electron beam-gas interactions is opposite. A timing cuts were applied: $\mid t_{FCAL} \mid < 8$ ns,$\mid t_{RCAL} \mid < 8$ ns, $\mid t_{FCAL} - t_{RCAL} \mid < 8$ ns.

- The quantity $E - p_z + 2 * E_\gamma$ has to be greater then 30 GeV, where E_γ is the energy of the photon tagged in the luminosity monitor.

In order to obtain a clean sample of NC DIS events, the following final selection cuts are applied to the data sample:

- Q^2 has to be in the interval:
  $7 \text{ GeV} < {Q^2}_{elec} < 100 \text{ GeV}^2$

- A minimum energy is required for the electron candidate $E'_{elec} > 10$ GeV in order to improve selection of neutral current sample. This cut also effectively removes the photoproduction background events.

- The impact position of the scattered electron on the RCAL calorimeter face is required to be outside a region defined by a square with the dimension 14 cm in x and y centered on the beam axis (box cut $\mid x \mid > 14$ cm or $\mid y \mid > 14$ cm) . Due to he partial shower losses of electrons which hit the calorimeter near the edge of the beam hole, the energy and the angle measurements become degraded. This requirement improves the measurement of the position and energy of the electron.

- To reduce the effects of calorimeter noise it is required that $y_{JB} > 0.04$.

- The majority of the photoproduction background is removed by the cut $\delta > 35$ GeV, whereas the cut $\delta < 65$ GeV suppresses electron beam-gas interactions which leave large energy deposits only in the RCAL.
- The DIS accepted events were required to have a measured tracking vertex. This cut reduces essentially the upstream beam-gas and cosmic rays events. The correct position of the vertex is very important because it influences the angles of the outgoing particles and hence the reconstruction of kinematic variables. A cut on the vertex position $\mid v_z \mid < 50$ cm was applied.
- Elastic QED Compton events ($ep \to ep\gamma$) are characterized by the two calorimeter deposits balanced in transverse momentum, one of which has an associated track. Algorithms based on events topology are used for their identification and rejection.

6.3 Jets search

After a clean sample of medium Q^2 NC DIS events has been selected we searched for jets of particles.

By a jet one understands clustering of hadrons produced at IP within certain angular interval. To find a jet the algorithms have been developed in which a test variable and the hadron recombination procedure have to be defined. The test variable is needed for decision whether or not the two final objects belong to the same jet. The recombination procedure is the prescription how to form a jet from finally observed particles.

There are two classes of jet algorithms used in the jet analysis:

- clustering algorithms (JADE [65], k_T algorithms [66]), or
- cone-type algorithms [67].

In the cone-type algorithms, the jets are formed by grouping the final state hadrons in a cone with a predefined radius in pseudorapidity - azimuthal angle space $\eta - \phi$, while in the clustering-type algorithms, particles are combined to form a jets if some test variable is smaller than a predetermined resolution parameter. In this type of algorithm the definition of jets does not suffer from the ambiguities resulting from overlapping cones, which make the cone algorithm less precise.

In the following we describe the cone-type algorithm, which was used in this thesis for the jet finding. A standard definition for cone-type algorithms was set by the 'Snowmass Convention' [68]. According to this recommendation a cone with center (η_{jet}, ϕ_{jet}) is defined in (η, ϕ) space in such a way that all the objects (calorimeter cells, hadrons or partons) with coordinates $(\eta_{object}, \phi_{object})$ within a radius R_0:

$$R \equiv \sqrt{(\phi_{jet} - \phi_{object})^2 + (\eta_{jet} - \eta_{object})^2} < R_0 \tag{6.1}$$

are included in the jet. The transverse energy of the jet ($E_{T,jet}$) and the coordinates of the jet axis (η_{jet}, ϕ_{jet}) are determined from the object coordinates which lie inside the jet cone:

$$\begin{aligned} E_{T,jet} &\equiv \sum_i E_{T,i} \\ \eta_{jet} &\equiv \frac{1}{E_{T,jet}} \sum_i \eta_i \cdot E_{T,i} \\ \phi_{jet} &\equiv \frac{1}{E_{T,jet}} \sum_i \phi_i \cdot E_{T,i} \end{aligned} \tag{6.2}$$

where $E_{T,i}$, η_i, ϕ_i are transverse energy, pseudorapidity and azimuthal angle of an object.

The jet cone coordinates (η_{jet}, ϕ_{jet}), should be determined in an iterative procedure from the initiating clusters. However, in this approach it is not specified how to obtain the initiating clusters and how to deal with the overlapping jets. This leaves quite a freedom and may lead to significant differences in the implementation.

The cone jet finder used in this thesis (called PUCELL [69]) is an adaptation of the jet algorithm used by the CDF collaboration [70]. In the first step, each object(calorimeter cell, hadron or parton) with transverse energy in excess of 0.5 GeV is considered as a seed for the search of the jet. These seeds are combined if their distance in (η, ϕ) space is smaller then 1 unit. Then a cone of radius R=1 is drawn around each seed and the objects within that cone are combined to form a cluster. The axis and transverse momenta of the precluster are defined as in equation (6.2). A new cone of radius 1 unit is then drawn around the axis of the resulting cluster. All the objects within the cone are used to recalculate a new cluster axis. The procedure is iterated until the content of the cluster does not change.

In the second step the energy sharing of overlapping clusters is considered. Two clusters are merged if the common transverse energy exceeds 75% of the total transverse energy of the cluster with the lowest transverse energy, otherwise two different clusters are formed and the common cells are assigned to the nearest in η, ϕ space cluster. Finally clusters are transformed into jets.

The k_T algorithm [66] has the advantage over cone algorithms that there is a clear choice for the starting point and a clear treatment of overlapping jets. The k_T algorithm, used in this thesis, starts from an initial list of objects (calorimeter cells, hadrons or partons) and recursively groups pairs of them together to form new object.
The algorithm depends on a parameter R, which should be chosen to be of order 1. This parameter is analogous to the cone size parameter in the cone algorithm.
The k_T algorithm begins with a list of objects and an empty list of completed jets. It then proceeds recursively as follows:

- for each object, define
  $d_i = E_{T,i}^2$

and for each pair of objects define
$d_{ij} = min(E_{T,i}^2, E_{T,j}^2)[(\eta_i - \eta_j)^2 + (\phi_i - \phi_j)^2]/R^2$
where $E_{T,i(j)}$, $\eta_{i(j)}$, $\phi_{i(j)}$ are transverse energy, pseudorapidity and azimuthal angle of an object,

- find the smallest of all the d_i and d_{ij} and label it d_{min},
- if d_{min} is a d_{ij}, merge objects i and j into a new object k with
  $E_{T,k} = E_{T,i} + E_{T,j}$
  and
  $\eta_k = [E_{T,i}\eta_i + E_{T,j}\eta_j]/E_{T,k}$
  $\phi_k = [E_{T,i}\phi_i + E_{T,j}\phi_j]/E_{T,k}$
- if d_{min} is a d_i, the corresponding object i is "not mergable" and remove it from the list of objects and add it to the list of jets,
- go to step 1

The procedure continues until there are no more objects, but all of them are uniquelly merged into jets.
The use of the $\eta\phi$ metric in the merging definition allowes the assumption that the results should be similar to those of a cone algorithm. However the k_T algorithm is completely different in method and therefore it is interesting if it leads to the same results as cone algorithm.

In this thesis both jet finding methods (cone and k_T) were used in LAB frame. The following jet selection criteria were applied:

- $E_{T,jet}^{LAB} > 4.0$ GeV and $-2.0 < \eta_{jet}^{LAB} < 2.0$. The E_T cut selects the hard jets and the pseudorapidity region selection is made to avoid proton remnant contamination;
- after transformation to the hadronic center of mass (HCM) frame it was also required that $E_{T,jet}^{HCM} > 4.0$ GeV. The analitical NLO calculations have been performed in HCM frame, so additional E_T cuts was applied also in this frame to have more reliable comparison with experimental data;
- only events with two jets within the described cuts were selected.

An example of a NC DIS dijet event as measured by the ZEUS detector is shown in Fig. 6.1. The event number 46231 comes from run number 13045. A scattered electron with energy of 24.9 GeV was detected in RCAL. Two jets: $E_{T,1}^{LAB} = 9.2$ GeV, $\eta_1^{LAB} = 1.6$ and $E_{T,2}^{LAB} = 9.8$ GeV, $\eta_2^{LAB} = 1.5$ were identified by a cone type algorithm in FCAL. The left plot in Fig. 6.1 shows calorimeter energy deposits and reconstructed tracks in tracking system. The upper right plot shows projection of energy deposits and of tracks on the plane perpendicular to the beam axis. The energy deposits are mainly in FCAL so they are not seen on the picture. The lower right plot illustrates energy flow as a function of azimuthal angle ϕ and pseudorapidity η.

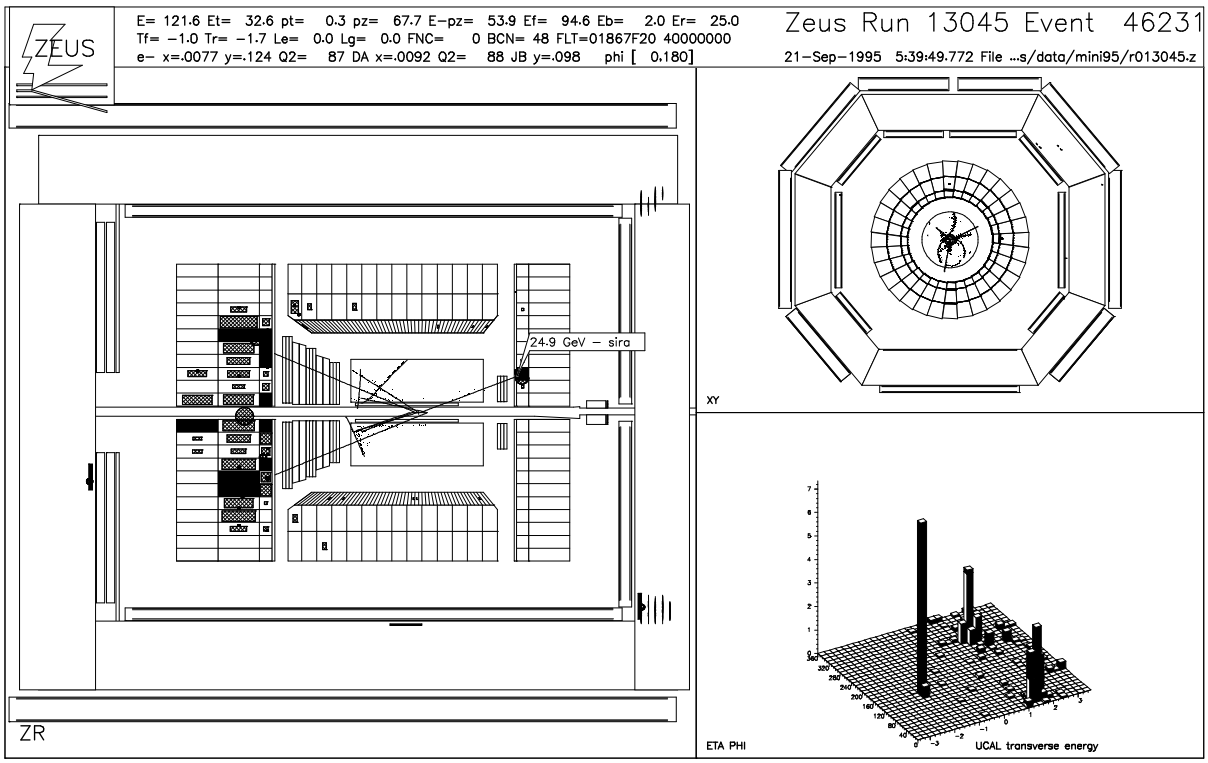

Figure 6.1: *Event display of NC DIS dijet candidate. Selection cuts described above were applied.*

6.4 Rejection of background events.

There are two different ways of rejecting background events from the final sample:

- an event-by-event method, based on the features of the background events,
- and a statistical method, in the case where the background events are very similar to the interesting ones.

Cosmic and halo muon as well as spark events are effectively subtracted in an event-by-event way at the trigger level.
The remaining background in the data sample, after all selection cuts have been applied comes from the beam-gas interactions or from photoproduction. It cannot be identified on an event-by-event basis, but it can be estimated and subtracted statistically.

Beam gas interactions
This source of background comes from the interactions of the beams with the residual gas in the beam pipe. The majority of the gas interactions are removed by cuts on calorimeter timing at the trigger level. However the remaining events have to be subtracted statistically. For this purpose the number of events that pass the final selection and originated

from pilot proton or electron bunches is determined and scaled with the ratio of the currents in the colliding and pilot bunches.
This type of background is much below 1% and therefore negligible for this analysis.

Photoproduction
For the selected Q^2 interval (7 GeV^2-100 GeV^2) the photoproduction background is due to electron misidentification. Therefore photoproduction MC was used for estimation of how significant that effect is. We generated the resolved and direct photon photoproduction events using Herwig MC and normalized their number to the total luminosity of the data. We have checked that they do influence dijet NC DIS analysis resulting in the contribution of about 1%. Therefore photoproduction background is negligible.

7 Jet studies

The dynamics of the hard scattering processes can be investigated by making the analysis of the multihadronic final state measured in the calorimeter and tracking detectors. The way to trace back the partonic structure of the high energy interactions is through the identification of jets of hadrons. The jet search applied in this analysis is performed by using the cone algorithm of radius R=1 defined in the pseudorapidity-azimuthal angle plane in laboratory frame.
In the first part of this section we present the results of jet studies for the NC DIS dijet events. We compare the measured transverse energy flows around the jet axis and the other jet characteristics called "jet shapes" with the MC predictions.
In the second part of this section the measurement of the jet energy scale difference between MC and data is discussed, since it represents a major part of the systematic studies. Finally we calculate the jet energy correction factors due to the particles energy loss in the inactive material in front of the calorimeter.

7.1 Energy flow around the jet axis

The selections of events and jets are described in Section 6. For each event two jets contribute separately in the plots shown.

The transverse energy flow at the detector level around the jet axis averaged over the dijet sample is shown in fig. 7.1.a, as a function of $\Delta\eta$, integrated over $\mid \Delta\phi \mid < 1$ and as a function of $\Delta\phi$ in fig. 7.1.b, integrated over $\mid \Delta\eta \mid < 1$. In this paragraph $\Delta\eta$ ($\Delta\phi$) denotes the difference between η_{jet} (ϕ_{jet}) of the jet axis and η_{cell} (ϕ_{cell}) of the calorimeter cell. Data (black points) are compared with Ariadne (solid line), Lepto (dashed line) and Herwig (dotted line) predictions. As can be seen Ariadne and Herwig overestimate the transverse energy in the jet center, whereas Lepto underestimates it. In fig. 7.2 the transverse energy flow around the jet axis in the $\Delta\eta, \Delta\phi$ plane in different η_{jet} intervals averaged over the dijet sample is shown. In grey are marked the cells assigned to the jet, in black the forward cells with $\eta_{cell} > 2.6$ and in white all other cells. The chosen jets are well separated from the proton remnant and they become wider with increasing jet pseudorapidity.

7.2 Jet shapes

To investigate the internal structure of the jets we have studied the integrated and differential jet shapes [71] at the detector level and compared them with detector level MC predictions.

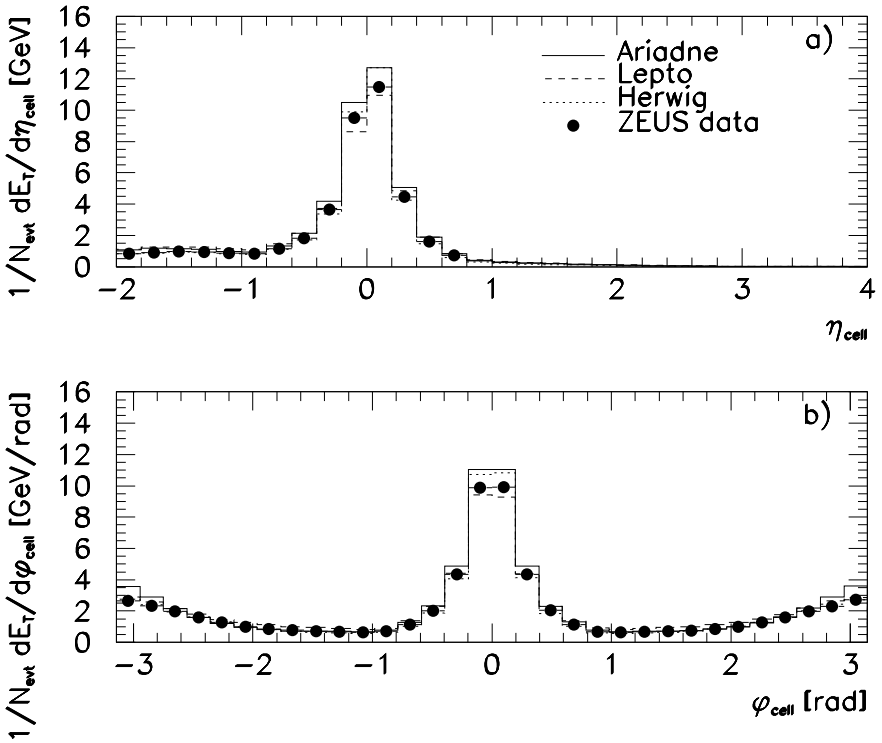

Figure 7.1: *Transverse energy flow around the jet axis in DIS dijet events; a)as a function of $\Delta\eta$, integrated over $|\ \Delta\phi\ | < 1$, b)as a function of $\Delta\phi$, integrated over $|\ \Delta\eta\ | < 1$. Data (black points), Ariadne (solid line), Lepto (dashed line) and Herwig (dotted line) are compared. Only statistical errors are shown, there typical magnitude is of the order of the symbol size.*

The integrated jet shape is defined as follows. For a given jet ($E_{T,jet}$) found with the cone algorithm (with radius R=1), the transverse energy within a sub-cone of a radius r is calculated:

$$\psi(r) = \frac{1}{N_{jets}} \sum_{jets} \frac{E_T(r)}{E_T(r=R)} \tag{7.1}$$

where $E_T(r)$ is the transverse energy within the inner cone of radius r and N_{jets} is the total number of jets in the sample.

In Fig. 7.3 we compare experimental distributions of ψ with the values calculated using Ariadne, Lepto and Herwig models for different values of jet transverse energy $E_{T,jet}$. The Ariadne and Herwig models reproduce the data very well below $E_T < 8$ GeV and $E_T < 6$ GeV respectively, however Lepto underestimates values of $\psi(r)$ in all regions. The agreement gets worse with increasing jet transverse energy. This can be clearly seen for the highest values of $E_{T,jet}$ (Fig 7.3.f). This is also confirmed in Fig 7.3.g where we plot $\psi(r = 0.5)$. The transverse energy within the jet core increases with increasing jet $E_{T,jet}$

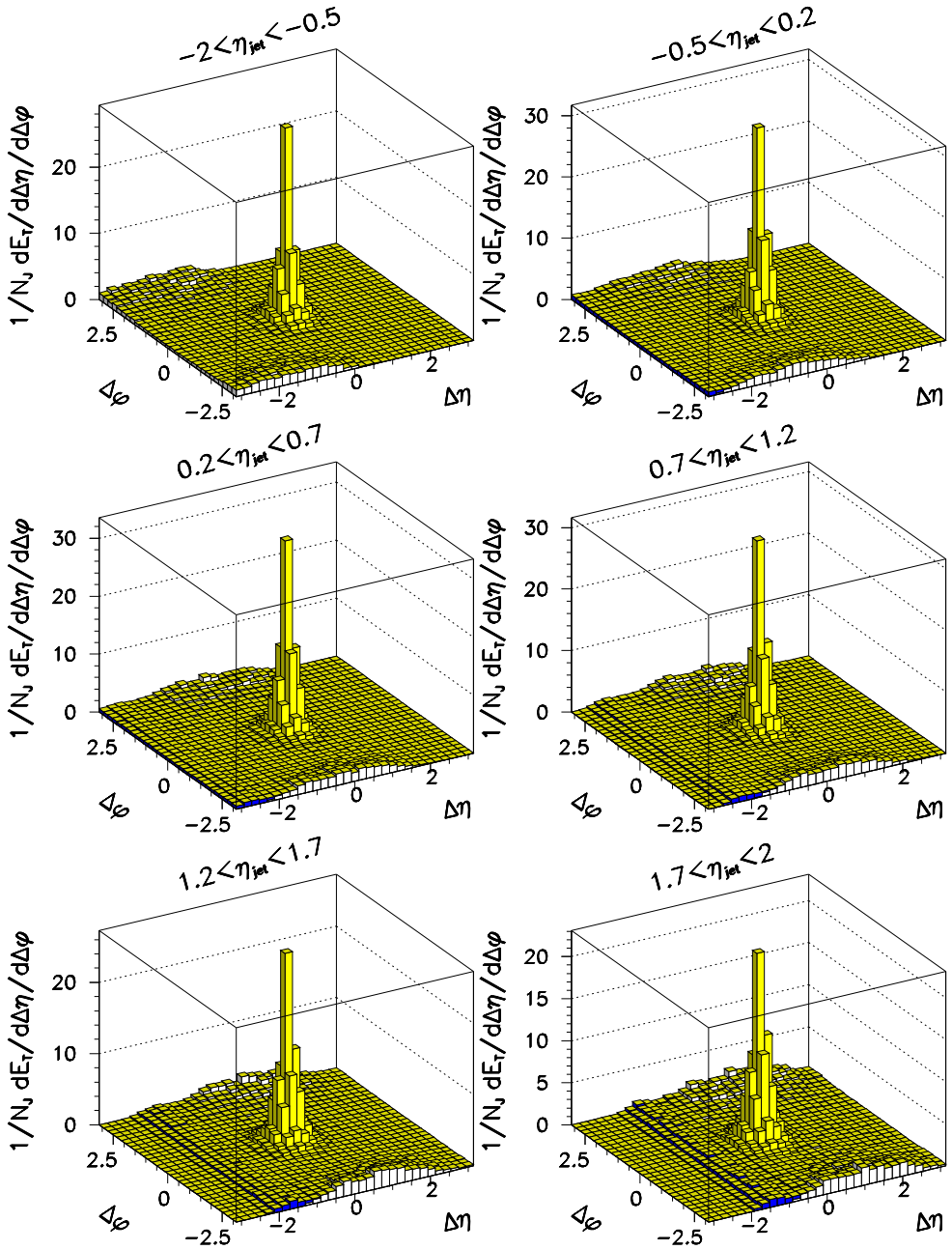

Figure 7.2: *Transverse energy flow around the jet axis in DIS dijet events as a function of $\Delta\eta$ and $\Delta\phi$ in different η_{jet} intervals. Grey histograms show cells assigned to the jet, black histograms are cells with $\eta_{cell} > 2.6$ and white histograms are all the other cells.*

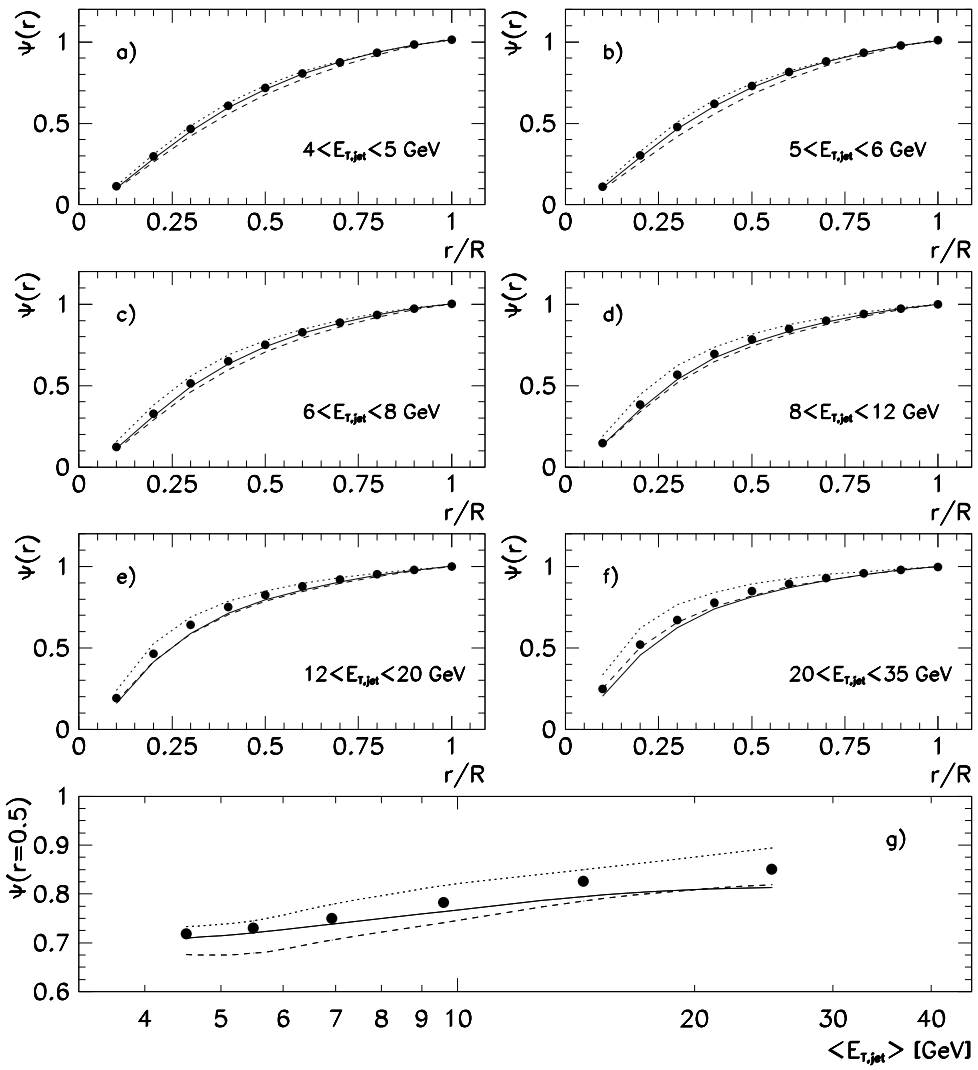

Figure 7.3: *Integral jet shapes for jets measured in six regions of $E_{T,jet}$: a) $4 < E_{T,jet} < 5$ GeV, b) $5 < E_{T,jet} < 6$ GeV, c) $6 < E_{T,jet} < 8$ GeV, d) $8 < E_{T,jet} < 12$ GeV, e)$12 < E_{T,jet} < 20$ GeV, f) $20 < E_{T,jet} < 35$ GeV. In g) the measured jet shape at fixed value of r=0.5, ψ(r=0.5) as the function of $E_{T,jet}$ is plotted. For comparison the reconstructed jet shapes from the Monte Carlo simulation of Ariadne (solid line), Lepto (dashed line) and Herwig (dotted line) are also shown. Only statistical errors are shown, there typical magnitude is of the order of the symbol size.*

which shows the jet collimation. This result is in agreement with the QCD calculations, which predict the increasing jet collimation with increasing E_T.

In fig 7.4 we compare the MC results on $\psi(r)$ with the experimental ones for different regions of η_{jet}. Ariadne MC describe the data quite well in all the bins. Lepto underes-

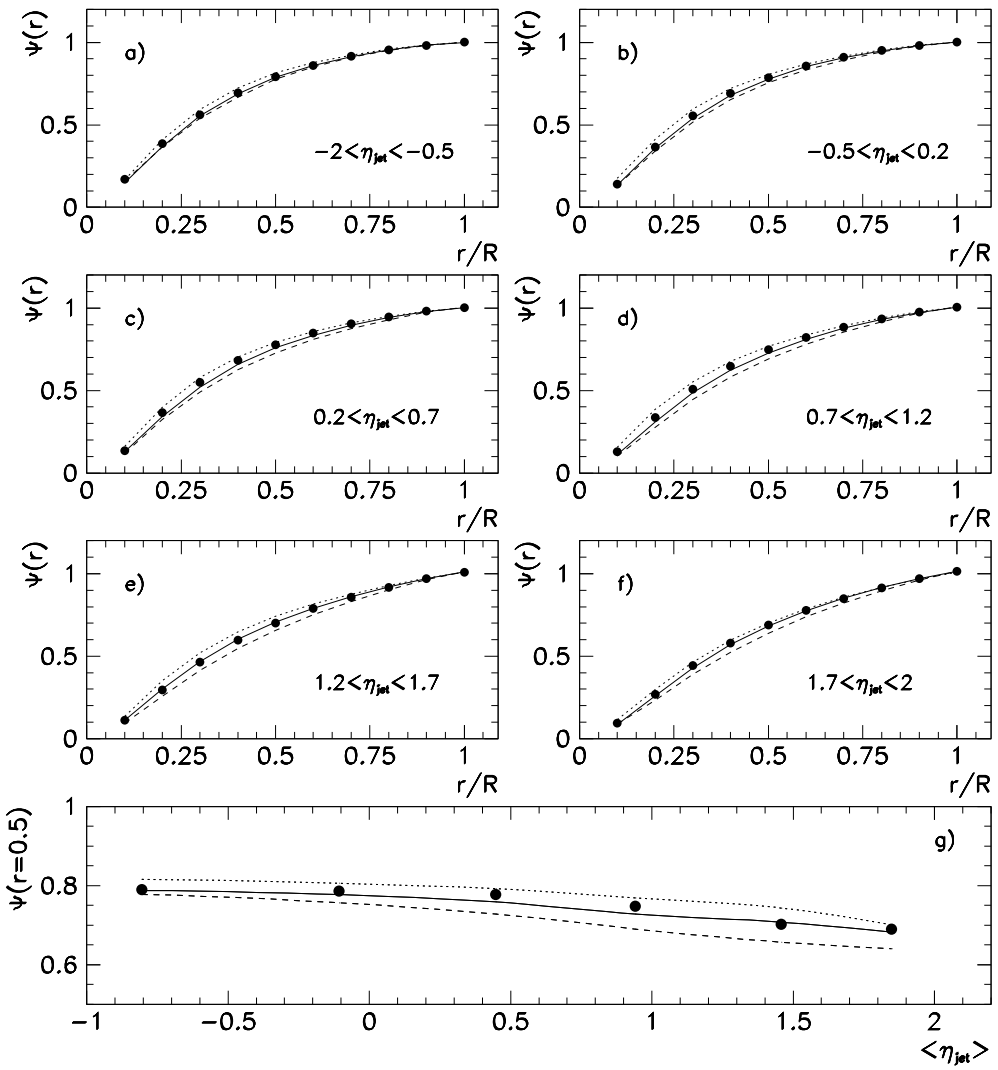

Figure 7.4: *Integral jet shapes for jets measured in six regions of* η_{jet}*: a)* $-2.0 < \eta_{jet} < 0.0$*, b)* $0.0 < \eta_{jet} < 0.5$*, c)* $0.5 < \eta_{jet} < 1.0$*, d)* $1.0 < \eta_{jet} < 1.5$*, e)* $1.5 < \eta_{jet} < 2.0$*, f)* $2.0 < \eta_{jet} < 2.2$*. In g) the measured jet shape at fixed value of r=0.5,* $\psi(r{=}0.5)$ *as the function* η_{jet} *is plotted. For comparison, the reconstructed jet shapes from the Monte Carlo simulation of Ariadne (solid line), Lepto (dashed line) and Herwig (dotted line) are also shown. Only statistical errors are shown, there typical magnitude is of the order of the symbol size.*

timates and Herwig overestimates values of $\psi(r)$ in all regions, except the first (last) one for which Lepto (Herwig) shows good data description. Similar situation is observed in Fig. 7.4.g where we plot $\psi(r = 0.5)$ versus η_{jet}. In this figure we observe weak broadening of a jet with increasing jet pseudorapidity.

In the following we study the differential jet shape. It is defined as a ratio of the transverse energy $E_T(r, \Delta r)$ in an annulus centered on the jet axis with an outer radius r and thickness Δr to the transverse jet energy $E_{T,jet}$:

$$\rho(r) = \frac{1}{N_{jets}} \sum_{jets} \frac{E_{T,jet}(r - \Delta r, r)}{E_{T,jet}(r = R)} \tag{7.2}$$

where N_{jets} is the total number of jets in the sample.

The values of $\rho(r)$ for measured data and MC (Ariadne, Lepto, Herwig) are shown in Fig. 7.5 for different values of $E_{T,jet}$. The Ariadne MC quite well reproduces the data for $E_{T,jet} < 8$ GeV, however for higher $E_{T,jet}$ it underestimates the transverse energy contained in the innermost rings. Lepto and Herwig show only qualitative data description.

The differential jet shapes measured for jets in different regions of η_{jet} (shown in fig. 7.6) are reasonably well described by Ariadne MC, whereas Lepto and Herwig predictions are only qualitative.

The energy flow around the jet axis is overestimated by Ariadne and Herwig models, whereas underestimated by Lepto MC. The integrated and differential experimental jet shapes show reasonably good agreement with Ariadne MC predictions, whereas Lepto and Herwig predictions do not reproduce the data.
The jets are becoming narrower with increasing transverse energy, which is in agreement with QCD predictions. We observe also a weak increase of jet width with increasing pseudorapidity.

7.3 Jet energy scale and energy corrections

The uncertainty in the calorimeter energy scale is the main source of the systematic error in the jet studies. Since the jet rates show strong fall off with increasing transverse energy of the jet, even a small shift in the energy scale may result in a significant change of the absolute normalization of the measured cross section. Therefore, a high precision determination of the jet energy in data and Monte Carlo is very important.

We present a new approach to estimate the difference between the energy measured and simulated by MC. The method is based on an event-by-event balancing of the transverse momentum of the scattered electron, a single jet and the remaining hadronic system [73].

Finally, we calculate the jet energy correction factors as a function of pseudorapidity η and the transverse jet energy.
We provide one set of the correction factors for data and one for MC in the case of P_T balancing method.
We get an independent correction estimation from the comparison of the hadron and the parton jets with the calorimeter jets. In this way we obtain one set of corrections for the hadron level and one for the parton level.

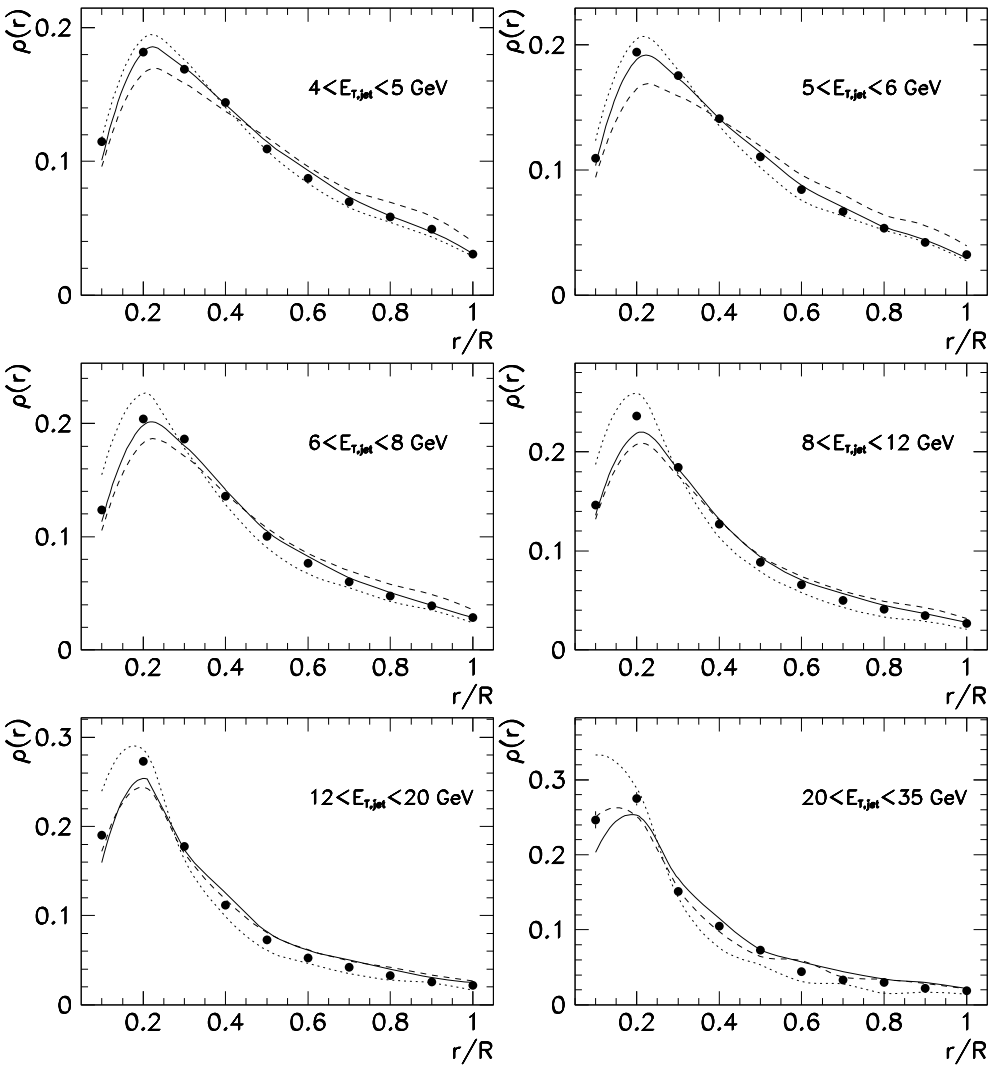

Figure 7.5: *Differential jet shapes for jets measured in six regions of $E_{T,jet}$: a) $4 < E_{T,jet} < 5$ GeV , b) $5 < E_{T,jet} < 6$ GeV, c) $6 < E_{T,jet} < 8$ GeV, d) $8 < E_{T,jet} < 12$ GeV, e) $12 < E_{T,jet} < 20$ GeV, f) $20 < E_{T,jet} < 35$ GeV. For comparison the reconstructed differential jet shapes from the Monte Carlo simulation of Ariadne (solid line), Lepto (dashed line) and Herwig (dotted line) are also shown. Only statistical errors are shown, there typical magnitude is of the order of the symbol size.*

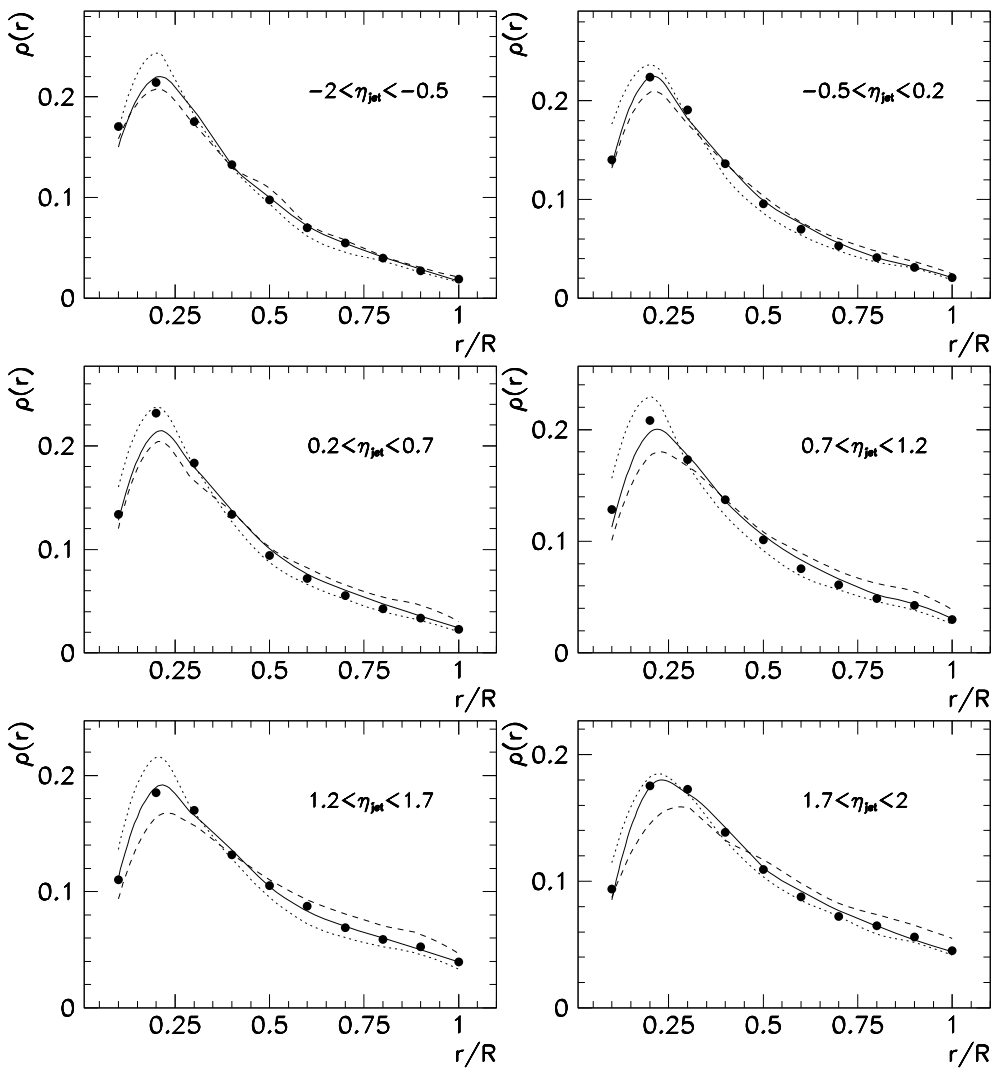

Figure 7.6: *Differential jet shapes for jets measured in six regions of* η_{jet}*: a)* $-2.0 < \eta_{jet} < 0.0$*, b)* $0.0 < \eta_{jet} < 0.5$*, c)* $0.5 < \eta_{jet} < 1.0$*, d)* $1.0 < \eta_{jet} < 1.5$*, e)* $1.5 < \eta_{jet} < 2.0$*, f)* $2.0 < \eta_{jet} < 2.2$*. For comparison the reconstructed jet shapes from the Monte Carlo simulation of Ariadne (solid line), Lepto (dashed line) and Herwig (dotted line) are also shown. Only statistical errors are shown, there typical magnitude is of the order of the symbol size.*

7.3.1 P_T balance method in DIS

The P_T balance method, used to estimate the jet energy corrections as well as the jet energy scale difference between data and MC, is based on the transverse momentum balance between the scattered electron and the hadronic system produced. We assume that the transverse momentum of the unmeasured hadronic system (escaping down through the beam pipe) is small and is uniformly distributed in azimuthal angle.

For this analysis, in addition to the kinematic cuts described in Section 6, we selected events with only one jet found in the ZEUS calorimeter with transverse momentum $p_{T,jet} >$ 2.5 GeV and pseudorapidity $\eta < 2.5$. For each event, the following transverse momenta are calculated:

- $p_{T,jet}$ of the jet.
- $p_{T,h}$ of the hadronic system excluding the jet, which is calculated as a vector sum of all the cells with energy deposits that are not contained in the jet.
- $p_{T,r}$ of the electron and the hadronic system excluding the jet. The electron energy was corrected for the detector effects with good accuracy.

The jet energy corrections in different regions of the calorimeter are calculated from the comparison of $\langle p_{T,jet} \rangle$ and $p_{T,r}$, in each bin of $p_{T,r}$ for the average value of $\langle p_{T,r} \rangle$ in that bin. This method relies on the fact that the corrected transverse momentum of the scattered electron is well measured.

In the following we compare the results obtained with the experimental data with Ariadne MC predictions. Data corresponds to an integrated luminosity of 6.1 pb^{-1}, whereas Ariadne MC corresponds to 4.2 pb^{-1}.

7.3.2 P_T balance method results

The shape distribution of the transverse momentum of the jet ($p_{T,jet}$) is shown in Fig. 7.7.a for MC and data. As can be seen from the figure the data is well simulated by MC. Similarly, the $p_{T,elec}$ (transverse momentum of electron) and $p_{T,r}$ distributions shown in Fig. 7.7.b,c are well reproduced by the MC. However Ariadne overestimates high $p_{T,h}$ and underestimeates low $p_{T,h}$ (Fig. 7.7.d). The average $\langle p_{T,h} \rangle$, is small for both data and MC.

In Fig. 7.8 the dependence of the jet transverse momentum ($p_{T,jet}$) on the transverse momentum of electron and hadronic system excluding the jet ($p_{T,r}$) is shown. In order to quantify this dependence the following procedure was adapted. For every interval in $p_{T,r}$ the average $\langle p_{T,jet} \rangle$ and average $\langle p_{T,r} \rangle$ were calculated. These values were then used in the fit of $\langle p_{T,jet} \rangle = A + B \cdot exp(C \cdot \langle p_{T,r} \rangle)$ The fit results are shown in Fig. 7.8 as solid

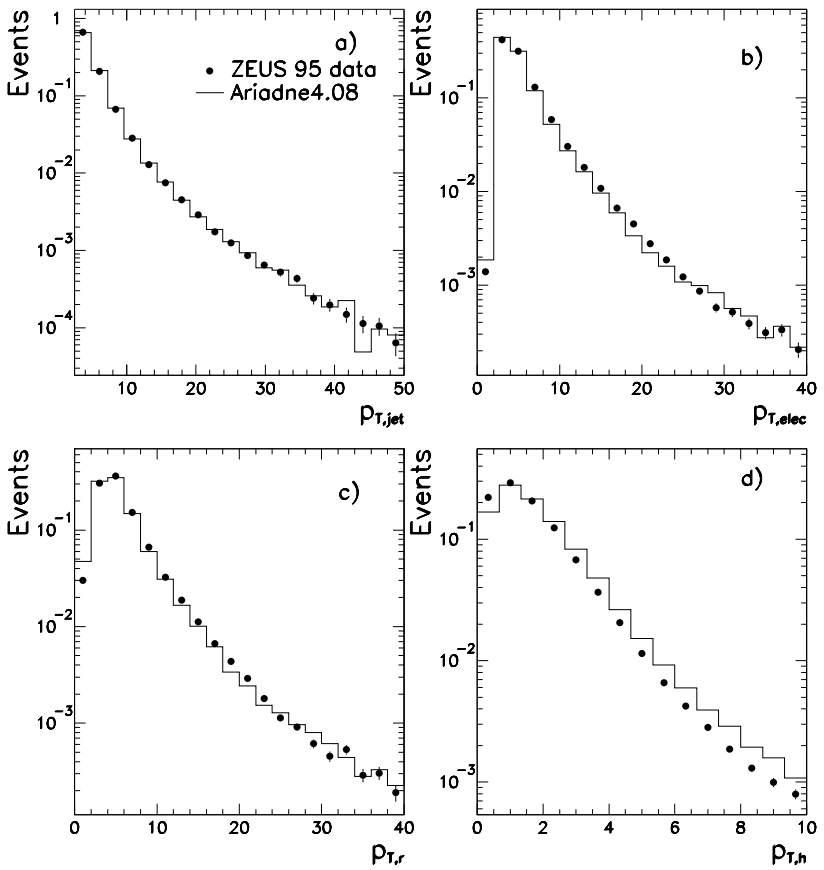

Figure 7.7: *Transverse momentum distributions of: a) the single jet, b) the scattered positron, c) the sum of positron and the remaining hadronic system excluding the jet and d) the remaining hadronic system after removal of the single jet. Black points are the data and the histograms is Ariadne MC.*

line, while the horizontal bars represent the interval size. The curve was fitted only for $p_{T,r} > 7$ GeV, in order to avoid interference with the $p_{T,jet} > 2.5$ GeV cut. The plots and the fitted parameters show that a straight line would yield a reasonable fit to the points for lower values of $\langle p_{T,r} \rangle$. The exponential term is only needed to fit the points at higher values of $\langle p_{T,r} \rangle$. The errors on the values of the fit parameters are about 1% and the χ^2 values are in the range: $0.8 < \chi^2 < 2.1$.

In Fig. 7.9 the ratio of the fitted curves for different ranges of $p_{T,h}$ was plotted. As can be seen, the results are largely independent of the range of $p_{T,h}$ and fit in mainly effected by well measured electron $p_{T,elec}$.

An exponential function was then fitted to $\langle p_{T,jet} \rangle$ versus $\langle p_{T,r} \rangle$ in different η_{jet} regions. The MC, data, and fitted curves are shown in Fig. 7.10. The parameters obtained from the fit are summarized in table 7.1. The errors on the values of the fit parameters are about 1% and the χ^2 values are in the range: $0.5 < \chi^2 < 2.3$. In this case, a straight line would also have yielded a reasonable fit apart from the points at large values of $\langle p_{T,r} \rangle$.

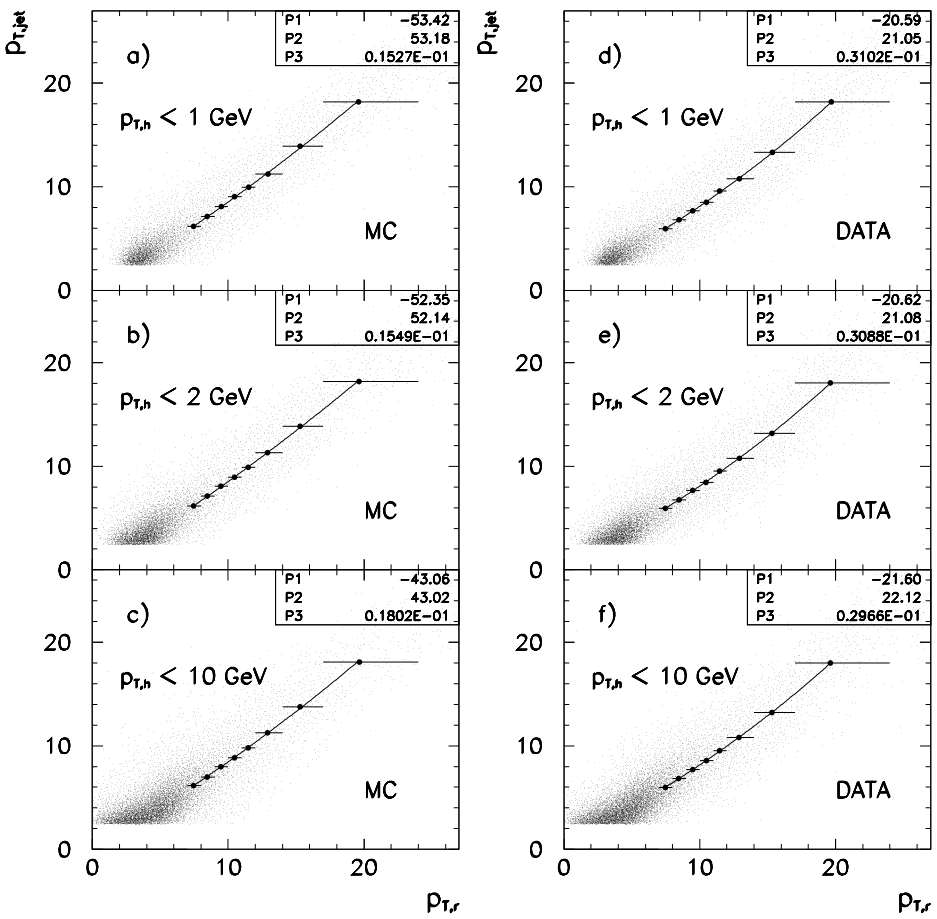

Figure 7.8: *Comparison of $p_{T,jet}$ versus $p_{T,r}$ in different $p_{T,h}$ bins for Ariadne MC (a,b,c) and data (d,e,f). Solid line shows fits of $\langle p_{T,jet} \rangle = A + B \cdot exp(C \cdot \langle p_{T,r} \rangle)$.*

η		MC			data		
minimum	maximum	A	B	C	A	B	C
-2.0	-1.2	-8.8	9.7	0.05	-8.7	9.8	0.05
-1.2	-0.5	-15.8	16.3	0.04	-12.7	13.5	0.04
-0.5	+1.0	-19.6	20.2	0.03	-47.5	47.5	0.02
+1.0	+1.5	-9.2	11.0	0.04	-15.8	17.1	0.03
+1.5	+2.0	-33.3	34.2	0.02	-23.3	24.4	0.03
+2.0	+2.6	-76.8	77.2	0.01	-153.8	153.7	0.01

Table 7.1: *Parameters A,B and C of the exponential fit to the profiles $\langle p_{T,jet} \rangle$ versus $\langle p_{T,r} \rangle$*

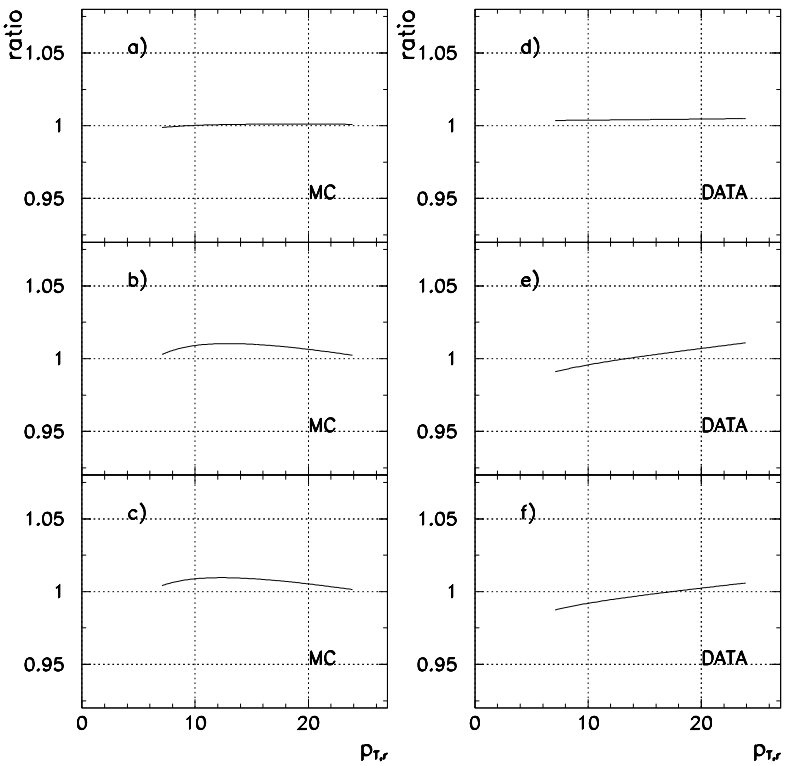

Figure 7.9: *Ratio of parameterizations of* $\langle p_{T,jet}\rangle = A + B\cdot exp(C\cdot\langle p_{T,r}\rangle)$ *for Ariadne MC (a,b,c) and data (d,e,f): a,d)* $\frac{\langle p_{T,jet}\rangle \ for\ p_{T,h}<1}{\langle p_{T,jet}\rangle \ for\ p_{T,h}<2}$, *b,e)* $\frac{\langle p_{T,jet}\rangle \ for\ p_{T,h}<1}{\langle p_{T,jet}\rangle \ for\ p_{T,h}<10}$, *c,e)* $\frac{\langle p_{T,jet}\rangle \ for\ p_{T,h}<2}{\langle p_{T,jet}\rangle \ for\ p_{T,h}<10}$.

The ratio $R = \frac{F_{MC}}{F_{data}}$, where $F = \frac{\langle p_{T,jet}\rangle}{p_{T,r}}$ is sensitive to the energy scale difference between the data and MC. The ratio R (left column) and the fitted functions (right column) for different bins in η_{jet} are shown in Fig. 7.11. In order to calculate the final energy scale difference we evaluated the mean value of $\langle R(p_{T,r})-1\rangle$ averaged over all data events. In Fig. 7.12 we plot the calculated energy scale difference between data and MC for the various η_{jet} bins. The values are also listed in table 7.2.

We observe reasonable agreement between data and MC in the forward region. In the central and backward regions the MC jet energy scale is overestimated. On the other hand, in the most backward region the MC jet energy scale is underestimated. However, one should note that the statistics in this region is quite low and therefore the results are less reliable.

7.3.3 Jet energy corrections from $P_{T,had(part)}/E_{T,cal}$ comparison

This method is based on the comparison of the transverse energy of calorimeter jets $E_{T,cal}$ with the transverse momentum of hadron (parton) jets $P_{T,had(part)}$. For comparison

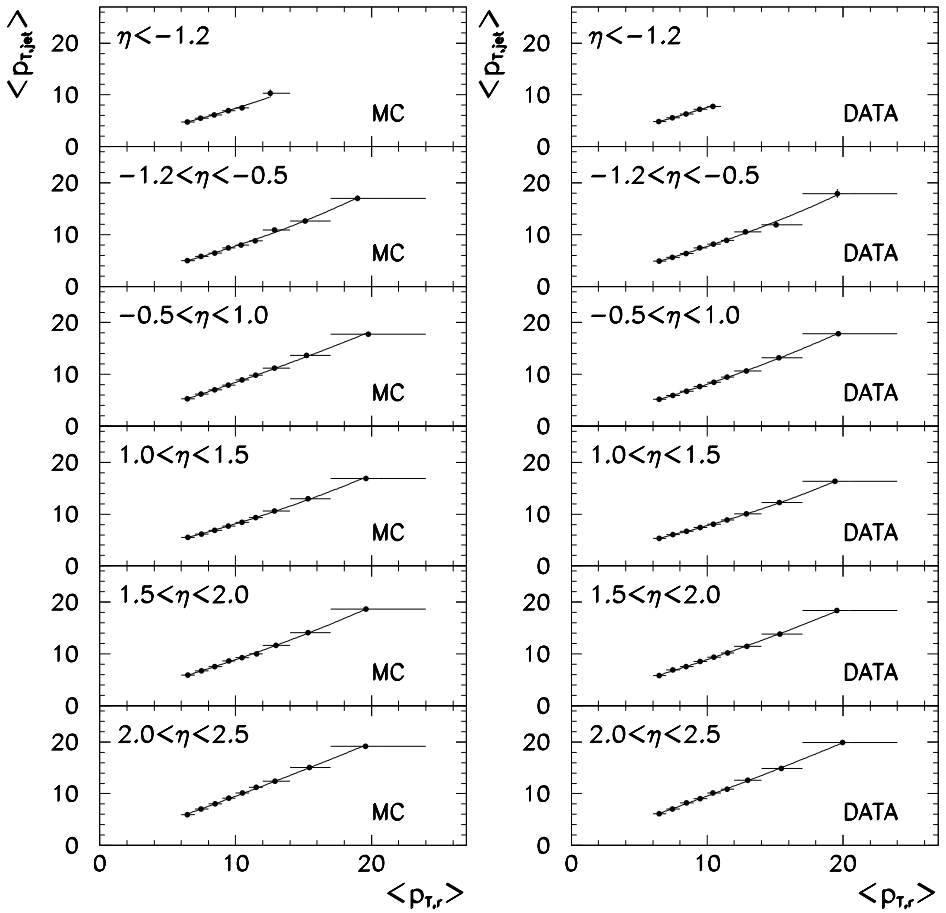

Figure 7.10: *Comparison of $\langle p_{T,jet} \rangle$ versus $\langle p_{T,r} \rangle$ in different η regions for Ariadne (left column) and data (right column). The solid line shows fits to the function $\langle p_{T,jet} \rangle = A + B \cdot exp(C \cdot \langle p_{T,r} \rangle)$*

η		energy scale
minimum	maximum	difference [%]
-2.0	-1.2	-1.7
-1.2	-0.5	1.5
-0.5	+1.0	3.9
+1.0	+1.5	3.9
+1.5	+2.0	0.2
+2.0	+2.5	-0.4

Table 7.2: *The energy scale difference between data and Ariadne. A positive value indicates an overestimation of the jet energy scale in the MC.*

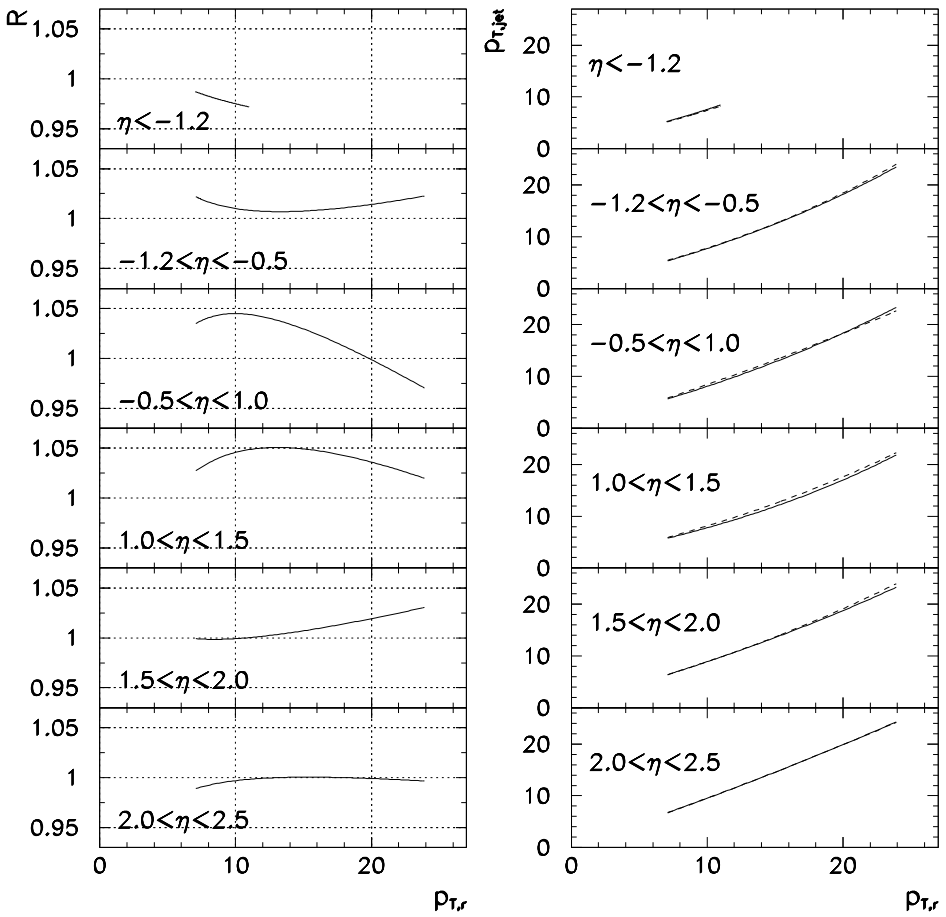

Figure 7.11: *Comparison of fitted functions* $\langle p_{T,jet} \rangle = A + B \cdot exp(C \cdot \langle p_{T,r} \rangle)$ *for Ariadne MC (dashed line) and data (solid line) in different* η_{jet} *bins (right column) and ratio R (see text) (left column).*

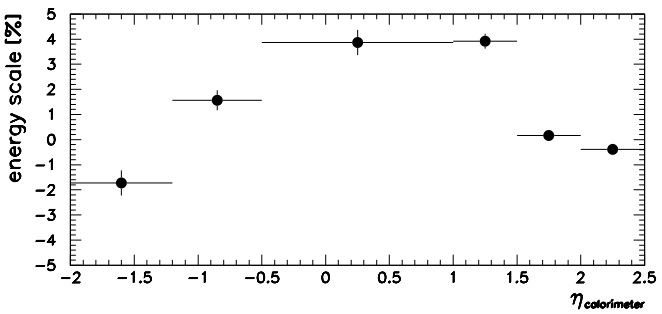

Figure 7.12: *Energy scale difference between MC and data for different* η *regions.*

η		hadron level		parton level	
minimum	maximum	A	B	A	B
-2.0	-1.2	0.54	0.71	0.39	0.66
-1.2	-0.5	0.16	0.76	-0.22	0.74
-0.5	+1.0	0.03	0.86	-0.31	0.84
+1.0	+1.5	0.33	0.79	0.21	0.76
+1.5	+2.0	0.21	0.87	-0.04	0.85
+2.0	+2.5	0.24	0.91	0.27	0.85

Table 7.3: *Parameters A,B of the linear fit to the profiles* $\langle E_{T,cal} \rangle$ *versus* $\langle p_{T,had(par)} \rangle$

Ariadne MC was used, which corresponds to an integrated luminosity of 4.2 pb^{-1}.

In this analysis, additional to the kinematic cuts described in Section 6, we selected events with two or more jets found in the calorimeter with transverse energy $E_{T,cal} > 1$ GeV and pseudorapidity $\eta_{jet,cal} < 2.5$.

Assuming that the hadronization process is well and reliably simulated by MCs we compare the transverse energy of the calorimeter object to the transverse momentum of the hadron jet. Obviously, both jets have to match in the (ϕ, η) plane. One should be aware of the fact that such a procedure leads to jet energies corrected to the hadron level. In Fig. 7.13(a-f) (left column on the plot) we plot the average value of the calorimeter jet transverse energy $\langle E_{T,cal} \rangle$ as a function of the hadron jet transverse momentum $\langle p_{T,had} \rangle$ in different intervals of η_{jet}. In this figure we also show the curves resulting from the fit of a form: $\langle E_{T,cal} \rangle = A + B \cdot \langle p_{T,had} \rangle$. The curve was fitted only for $p_{T,had} > 4$ GeV, in order to avoid interference with the applied detector level jet cut $E_{T,cal} > 1$ GeV. The fit parameters are summarized in table 7.3.

For those who dare to go one step further we compare in Fig. 7.13(g-l) (right column on the plot) the partonic jet transverse momentum to the calorimeter jet transverse energy. Also the curves resulting from the fit ($\langle E_{T,cal} \rangle = A + B \cdot \langle p_{T,par} \rangle$) are shown. The curves were fitted only for $p_{T,par} > 4$ GeV, in order to avoid interference with the applied detector level jet cut $E_{T,cal} > 1$ GeV. The fit parameters are summarized in table 7.3.

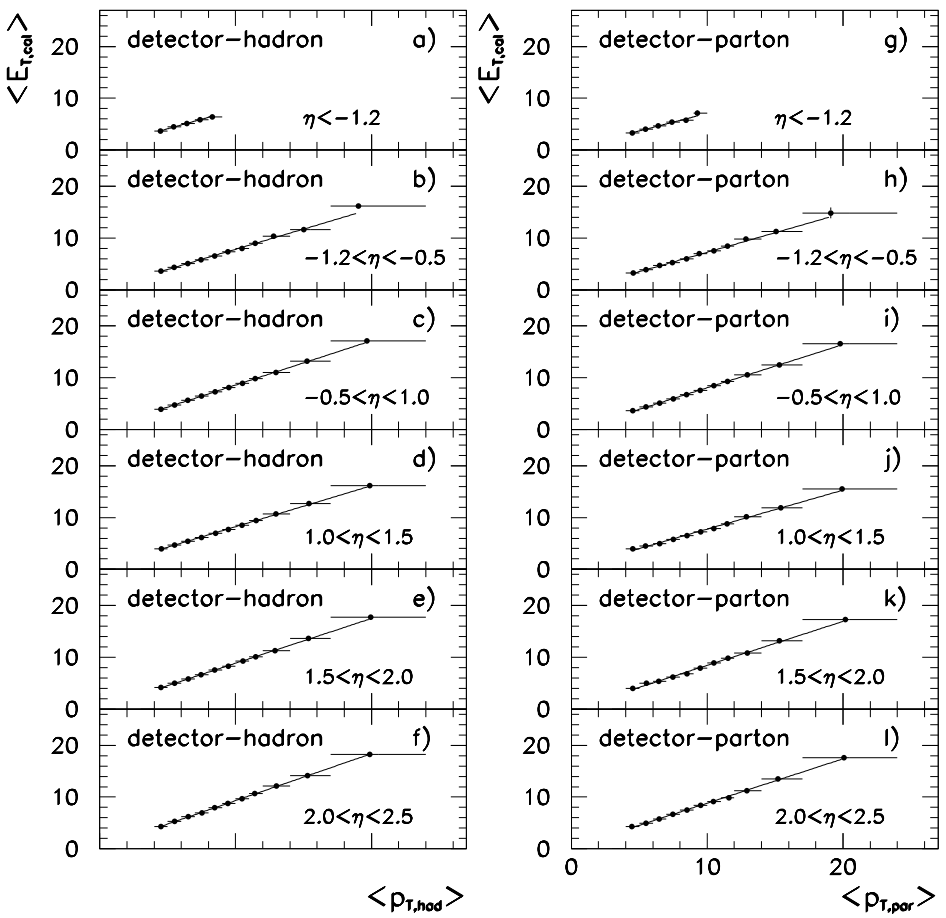

Figure 7.13: *Comparison of the transverse momentum of hadron (parton) $p_{T,had}$ ($p_{T,par}$) and calorimeter jets $\langle E_{T,cal}\rangle$ in different η regions. The solid line shows fits of the function $\langle E_{T,cal}\rangle = A + B \cdot \langle p_{T,had(part)}\rangle$.*

8 Determination of dijet cross section using the cone algorithm

In this section the differential and the integrated dijet cross sections for jets identified in laboratory frame with the cone type algorithm are presented. We compare experimental results with the Monte Carlo predictions and NLO theoretical calculations.

8.1 Detector level comparison between MC and data

We use Monte Carlos (Ariadne, Lepto, Herwig) to correct the data for all distortions due to the detector effects and reconstruction methods. Therefore, it is essential that the MC describes basic distributions of our selected NC DIS dijet sample.
In Fig. 8.1 we compare normalized to unity distributions of kinematical variables Q^2_{elec}, x_{elec}, E_{elec} (reconstructed with the electron method), y_{JB} (reconstructed with the Jacquet-Blondel method), $E - p_z$ and v_z (reconstructed vertex) with Ariadne, Lepto and Herwig predictions at the detector level. From these models Ariadne is closest to the data except $E - p_z$ distribution which is not reproduced by any of MC. Particularly big differences are found in Q^2 shape comparison between Herwig and data.

In Fig. 8.2 we compare distributions of the jet variables. The jet azimuthal angle (ϕ), the pseudorapidity (η) and the transverse energy (E_T) measured in experiment are roughly reproduced by the MC models, although the high E_T jets tail is overestimated by all the models.

From the considered models Ariadne gives the overall reasonable description of the data and will be used for the default correction of the data to hadron and parton levels.

8.2 Corrections for detector effects

The measured distributions are always affected by the trigger logic, selection cuts, detector resolution and by reconstruction methods. The main goal of an experimentalist is to correct the observed distributions for all these distortions, so that they can be compared with the theoretical predictions.

As a first step the jet energy corrections (see Section 7.3) were applied then the resolution of the energy and position (i.e. pseudorapidity and azimuthal angle) of the jets due to finite granularity of the calorimeter cells were checked. The resolutions defined as the differences between the reconstructed (after detector simulation) jet variables and the hadronic (partonic) ones:

$$\Delta\eta \equiv \eta^{det} - \eta^{true}$$

$$\Delta\phi \equiv \phi^{det} - \phi^{true}$$

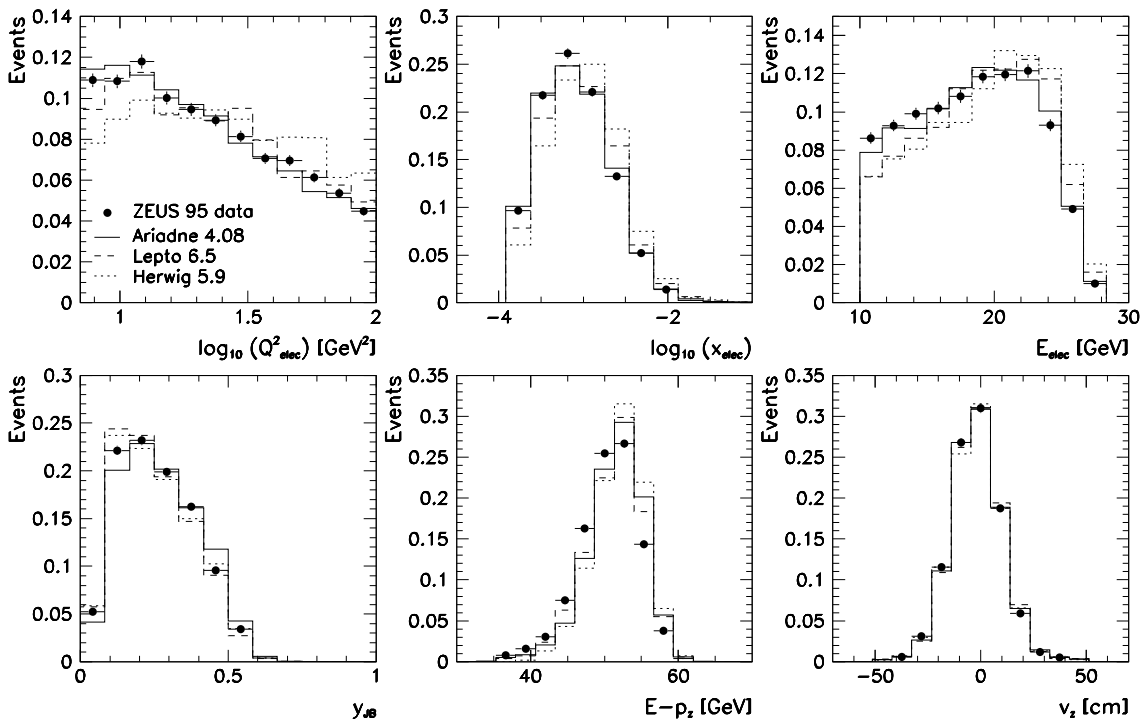

Figure 8.1: *Distribution comparison of Q^2_{elec}, x_{elec}, E_{elec} (reconstructed with the electron method), y_{JB} (reconstructed with the Jacquet-Blondel method), $E - p_z$ and v_z (reconstructed vertex) between data (black points), Ariadne (solid line), Lepto (dashed line) and Herwig (dotted line) at the detector level. Only statistical errors are shown.*

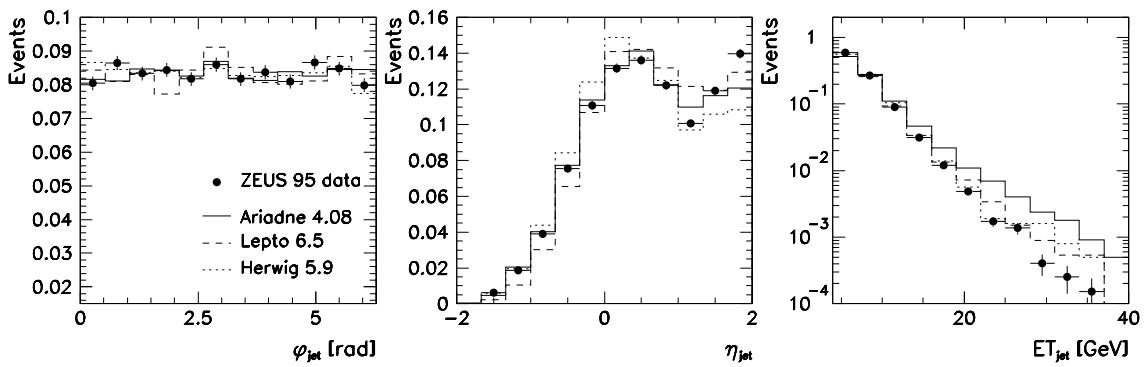

Figure 8.2: *Jet variable distribution comparison (azimuthal angle (ϕ), pseudorapidity (η), transverse energy (E_T)) between data (black points), Ariadne (solid line), Lepto (dashed line) and Herwig (dotted line) at the detector level. Only statistical errors are shown.*

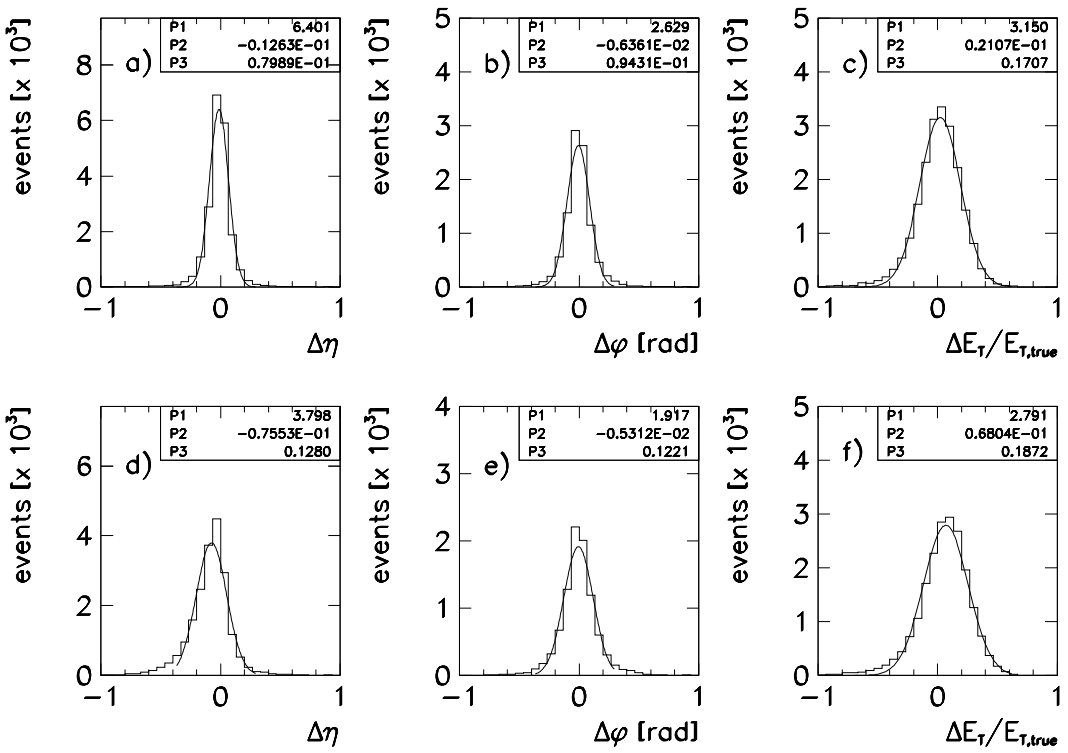

Figure 8.3: *Resolution of jet variables: pseudorapidity $\Delta\eta$, azimuthal angle $\Delta\phi$ and transverse energy ΔE_T at the hadron (a,b,c) and parton (d,e,f) levels.*

$$\frac{\Delta E_T}{E_T} \equiv \frac{E_T^{det} - E_T^{true}}{E_T^{true}}$$

where *det* and *true* are reconstructed and true (hadronic or partonic) level variables, respectively. The widths of these distributions (shown in Fig. 8.3) at the hadron (parton) level are: for η_{jet} 0.08 (0.13), for ϕ_{jet} 0.09[rad] (0.12[rad]) and for $E_{T,jet}$ 17% (19%).

In order to measure the cross sections at the hadron and parton levels the correction for the detector effects was performed by comparing generated events with the reconstructed after detector simulation. We calculated also the purity and the efficiency.
Purity is the ratio of the number of dijet events generated and reconstructed in one bin to the total number of dijet events reconstructed in this bin:

$$purity = \frac{\#dijet\ event\ found\ at\ generator\ AND\ detector\ levels\ in\ a\ bin\ after\ all\ cuts}{\#dijet\ events\ found\ at\ detector\ level\ in\ the\ same\ bin\ after\ all\ cuts}$$

Efficiency is the ratio of dijet events generated and reconstructed in one bin to the total number of dijet events generated in this bin:

$$efficiency = \frac{\#dijet\ events\ found\ at\ generator\ AND\ detector\ levels\ in\ a\ bin\ after\ all\ cuts}{\#dijet\ events\ found\ at\ generator\ level\ in\ the\ same\ bin\ after\ all\ cuts}$$

Both quantities test the measurement quality.

A dijet event which is found at the detector level will contribute to the impurity if there is no corresponding dijet event at the generator level inside the same bin, within the set of cuts applied. If there is no dijet event in the detector, although there is one fulfilling all the selection criteria at the generator level, this will reduce the efficiency of the dijet detection. Both quantities are calculated after energy corrections. They reflect the limitations of the dijet detection due to the distortions produced by detector and imposed by the selection cuts. The higher they are the better is the measurement.
The correction factors are calculated using the bin-to-bin method. Correction factor in each bin is calculated as the ratio of the number of generated to the number of reconstructed dijet events in this bin:

$$corr.fact. = \frac{\#dijet\ events\ at\ generator\ level\ in\ a\ bin\ after\ all\ cuts}{\#dijet\ events\ at\ detector\ level\ in\ the\ same\ bin\ after\ all\ cuts}$$

8.3 Total and differential dijet cross section determination

In this section the experimental distributions of kinematical and jet variables corrected to hadron (parton) levels and Monte Carlo models are compared. Also the total and the differential cross sections are determined.
For corrections all three MC models (Ariadne, Lepto and Herwig) are used separately. The results are compared also to these models. Parton level results are additionally compared to the next-to-leading order calculations based on the program Mepjet 2.0 [56].

Jets were reconstructed using a cone algorithm in the laboratory frame. At the detector level, the jet finding was performed using the calorimeter cells after excluding those containing energy deposited by the scattered electron. The same algorithm was also applied to the hadrons and partons of the MC samples as well as the partons in the next-to-leading order calculations. The reconstructed jets were required to have a minimum transverse energy $E_T > 4$ GeV in both the laboratory and the hadronic center of mass frame and a pseudorapidity in the range -2 $< \eta <$ 2 in the laboratory frame. The E_T selection at the detector level was made after the jet energies were corrected with the help of MC. Only events with two jets were accepted. In addition the events were required to satisfy the criteria: 7 GeV^2 $< Q^2 <$ 100 GeV^2, $y > 0.04$ and scattered electron energy $E_{e'} > 10$ GeV.

These selection criteria are listed in Table 8.1. A total number of 13869 events with two jets fulfilled these requirements.

In Fig. 8.4 and 8.5 the comparison of the shape from the data corrected to the hadron (parton) level with the hadron (parton) level predictions of the MC models is shown.

The variables η^{LAB}_{max} (η^{LAB}_{min}) are the pseudorapidity of the more forward (backward) of the two jets identified in laboratory frame. The Ariadne MC reproduces the distributions well. The other models also reasonably describe the shape, except Herwig which fails to reproduce the Q^2 distribution.

$7\ \text{GeV}^2 < Q^2 < 100\ \text{GeV}^2$
$E_{e'} > 10$ GeV
$p_{T,LAB} > 4$ GeV
$p_{T,HCM} > 4$ GeV
$-2 < \eta < 2$
number of identified jets = 2

Table 8.1: *Selection criteria of events for the cross section determination.*

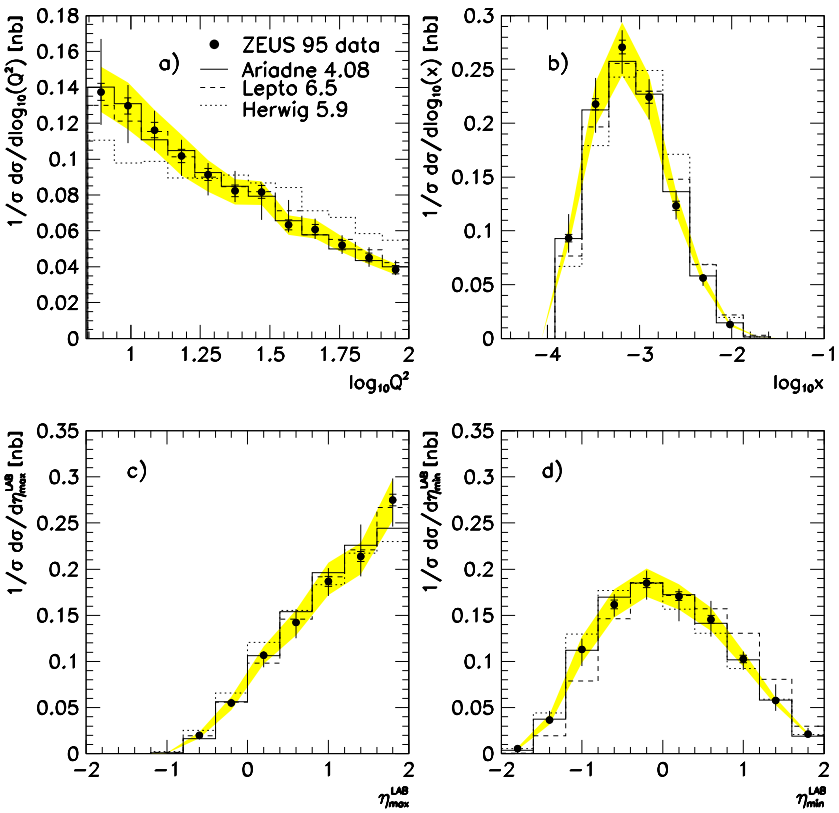

Figure 8.4: *Comparison of distributions a) Q^2, b) x, c) η_{max}^{LAB}, d) η_{min}^{LAB} between the data corrected to hadron level (black points) and the MC models Ariadne (solid line), Lepto (dashed line), Herwig (dotted line). The inner(outer) error bars indicate the statistical error (statistical and systematical errors added in quadrature). Shaded area shows jet energy scale uncertainty.*

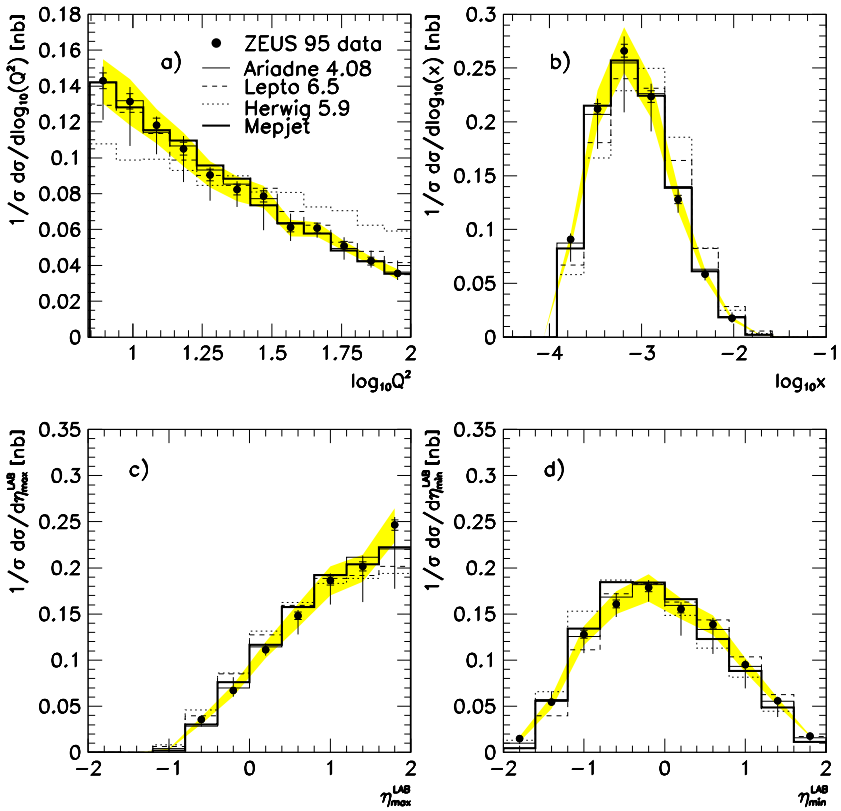

Figure 8.5: *Comparison of distributions a) Q^2, b) x, c) η^{LAB}_{max}, d) η^{LAB}_{min} between the data corrected to parton level (black points) and the MC models Ariadne (solid line), Lepto (dashed line, Herwig (dotted line) Mepjet 2.0 (solid thick line). The inner(outer) error bars indicate the statistical error (statistical and systematical errors added in quadrature). Shaded area shows jet energy scale uncertainty.*

In Fig. 8.6 the differential cross sections corrected to the hadron level and the hadron level MC predictions are shown. The variable $\xi = x(1 + m^2_{jj}/Q^2)$ (where m_{jj} is the invariant mass of two jets) is related to the momentum fraction of the gluon or quark emitted from the proton calculated in leading order QCD picture. The variables $p_{T,max}$ ($p_{T,min}$) are defined as the larger (smaller) of the transverse momenta of the two jets in the hadronic center of mass (HCM) system.
Ariadne MC reproduces the shape correctly (what can be seen after normalization to the unity) but it overestimates the dijet rate. Lepto and Herwig MC underestimate the rate, whereas reproduce reasonably the shapes, except Herwig which fails to describe the Q^2 distribution.

Fig. 8.6.c,d the differential cross sections are shown as a function of $p^2_{T,max}/Q^2$ and $p^2_{T,min}/Q^2$. It is worth mentioning that there are two scales relevant for dijet measurement. The first one is the momentum transfer squared of the virtual photon Q^2 and the second

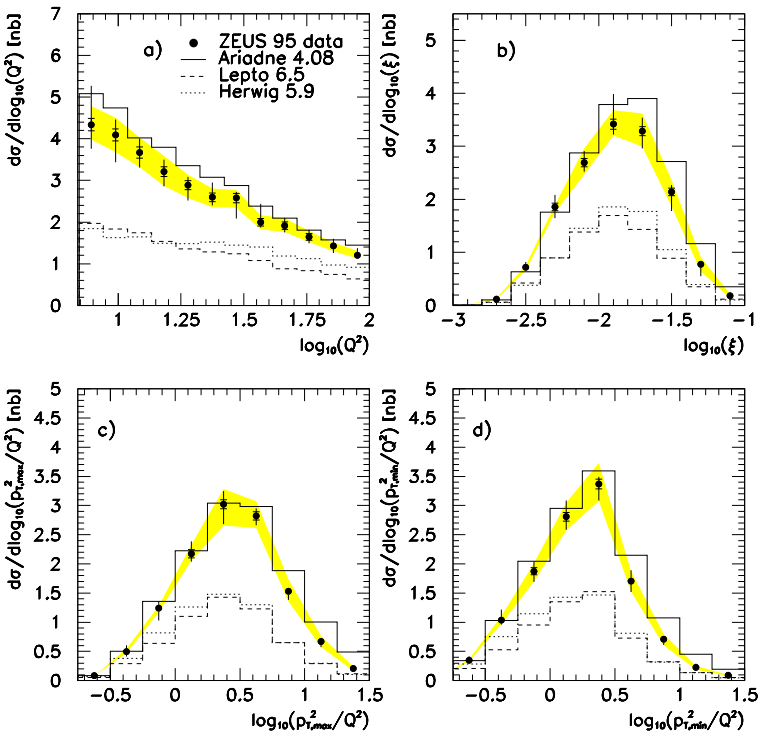

Figure 8.6: *Differential dijet cross section at hadron level versus a) Q^2, b) ξ, c) $p^2_{T,max}/Q^2$, d) $p^2_{T,min}/Q^2$. The inner(outer) bars indicate the statistical error (statistical and systematical errors added in quadrature). Shaded area shows jet energy scale uncertainty. The measured cross sections corrected to hadron level (black points) are compared to MC models Ariadne (solid line), Lepto (dashed line), Herwig (dotted line).*

one is the transverse momentum of the identified jets. The Q^2 is the standard scale in deep inelastic scattering and should be chosen high enough that the perturbative QCD can be applied. The transverse momentum of the jets has to be large in order to allow a good reconstruction of the jets. In Fig 8.6.c,d one can distinguish three different regions of p_T^2/Q^2. The Q^2 scale dominates for $p_T^2/Q^2 \ll 1$ and this region is supressed due to the jets and Q^2 selection cuts. For $p_T^2/Q^2 \approx 1$ Ariadne MC only slightly overestimates the measurement, whereas other models fail to reproduce it. The p_T scale dominates for $p_T^2/Q^2 \gg 1$ and none of the MC models reproduce the experimental data.

In Fig. 8.7 the differential cross sections corrected to the parton level are compared with the parton level MC predictions and the NLO QCDcalculations as provided by Mepjet 2.0 program. For Mepjet 2.0 the factorization (μ_F) and renormalization (μ_R) scales (see Section 2.5) were chosen to be $\mu_F^2 = \mu_R^2 = Q^2$ and the CTEQ4M proton structure function was used. The Mepjet 2.0 NLO calculations reproduce the shape of all variables adequately, whereas they underestimate the overall rate.

The purities, efficiencies and correction factors for the Q^2, ξ, $p^2_{T,max}/Q^2$ and $p^2_{T,min}/Q^2$

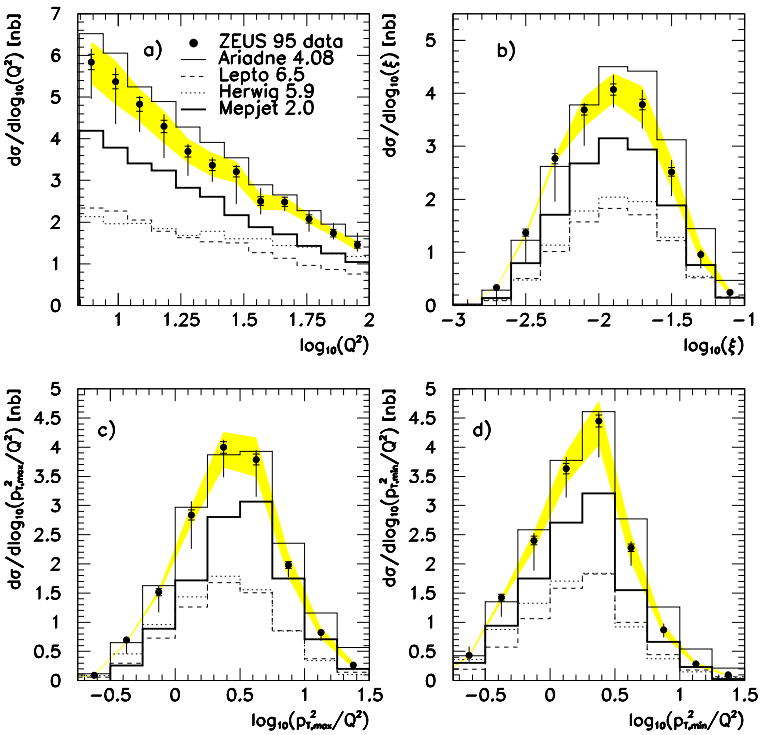

Figure 8.7: *Differential dijet cross section at parton level versus a) Q^2, b) ξ, c) $p^2_{T,max}/Q^2$, d) $p^2_{T,min}/Q^2$. The inner (outer) bars indicate the statistical error (statistical and systematical errors added in quadrature). Shaded area shows jet energy scale uncertainty. The measured cross sections corrected to parton level (black points) are compared to MC models Ariadne (solid line), Lepto (dashed line), Herwig (dotted line) and NLO calculations.*

differential cross section measurements are discussed in Appendix A (in Fig. A.1 and Fig. A.2), whereas the differential cross section values and errors are collected in Tab. A1 and Tab. A2.

Integrated over the selected kinematic region, the experimental total dijet cross sections at the hadron and parton levels are compared with those obtained by Ariadne, Lepto, Herwig and Mepjet 2.0 models in Tab. 8.2. The Ariadne MC overestimates both hadron and parton level total cross section by about 14%, whereas Lepto and Herwig MC underestimate it by about 50%. The QCD NLO calculations also underestimate total dijet cross section by 28%.

8.4 The Born cross section

Any measured quantity in NC ep scattering can be affected by the emission of radiative γ by the initial and/or final electron. In this section the size of radiative corrections for

results	parton level σ_{dijet} [nb]	hadron level σ_{dijet} [nb]
ZEUS 95 data	3.93 ± 0.04 (stat) $^{+0.34}_{-0.61}$ (sys)	3.04 ± 0.03(stat) $^{+0.36}_{-0.39}$ (sys)
Mepjet 2.0	2.84 ± 0.03 (stat) $^{+0.00}_{-0.45}$ (sys)	
Ariadne 4.08	4.42 ± 0.05 (stat)	3.49 ± 0.04 (stat)
Lepto 6.5	1.74 ± 0.02 (stat)	1.46 ± 0.02 (stat)
Herwig 5.9	1.91 ± 0.03 (stat)	1.60 ± 0.02 (stat)

Table 8.2: *Comparison of experimentally measured cross sections with MC predictions.*

the dijet NC DIS analysis is estimated.

Experimentally it is impossible to say whether a radiative photon is emitted before or after an interaction with the proton. However this is possible in the Monte Carlo simulations and here we decompose the radiative processes into initial state radiation(IR), final state radiation (FSR) and the virtual corrections. The radiative photon is close in direction to the emitting electron so for large Q^2 NC DIS one can even experimentally aproximately distinquish between ISR and FSR. Photons coming from FSR are often measured in the calorimeter close to the scattered electron. The most significant distortion of kinematical variables measurement comes from the ISR.

To check for the QED radiative effects the Django 6.24 [52] Monte Carlo program which combines Ariadne 4.08 [49] and Heralces 4.5.2 [53] was used. Two samples of Django MC, each of about 12 pb^{-1}, one with radiative corrections switched on and the other with radiative corrections switched off were generated. All the other parameters were kept exactly the same in both samples.

The generated total cross section in the phase space region of interest (see Table 8.1) with radiative corrections at the hadron (parton) level after the final cuts is 3.45 ± 0.04 (stat) nb (4.36 ± 0.05 (stat) nb), whereas it is 3.44 ± 0.04 (stat) nb (4.33 ± 0.05 (stat) nb) without radiative corrections. The cross section values generated with and without QED corrections, both at the hadron and parton levels, agree within statistical errors. By comparing these values it can be concluded that the radiative corrections contribute in 0.3% (0.7%) to hadron (parton) level total cross section.

In Fig. 8.8 the influence of radiative corrections on the differential cross sections is shown. The Q^2 and the x distributions in the phase space region of interest are shown for corrections switched off and on.

The conclusion from these studies is that the effect of QED radiative corrections is negligible in our dijet NC DIS analysis.

8.5 Systematic studies

To estimate the sensitivity of the measured dijet cross section the following checks were made:

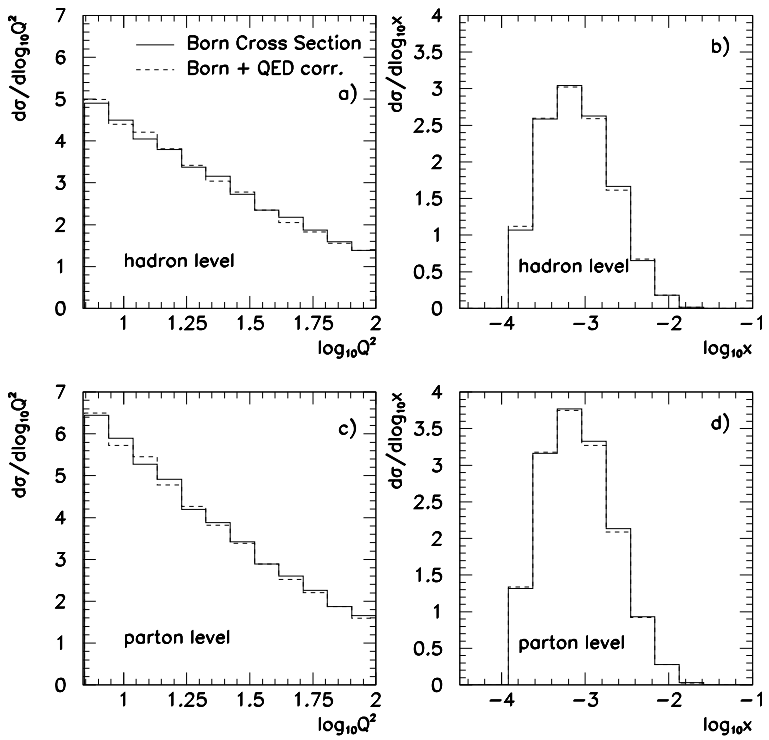

Figure 8.8: *Comparison of the differential cross sections generated with QED radiative corrections at the hadron and parton levels (solid line) to the differential cross section generated without QED radiative corrections (dashed line).*

- the energy jet corrections were obtained by comparing hadron (parton) and detector levels in Ariadne, Lepto and Herwig MC's;
- the energy jet scale of the calorimeter was changed by $\pm$ 4.0 %;
- the jet pseudorapidity region search was changed ± 0.2;
- $y_{JB} > 0.1$ was applied instead of $y_{JB} > 0.04$
- electron box cut was changed from: $\mid x_{elec} \mid > 14$ cm or $\mid y_{elec} \mid > 14$ cm to: $\mid x_{elec} \mid >$ 13 cm or $\mid y_{elec} \mid > 8$ cm in RCAL ;
- the lower Q^2 cut was varied by ± 0.5 GeV^2,
- the electron energy cut was changed by: +1 GeV,
- the $E - p_z > 40$ GeV was applied instead of $E - p_z > 35$ GeV,
- the vertex position was varied by: $\pm$ 10 cm,

- the electron energy scale was changed by $\pm$ 1.0%
- the jet E_T was changed by $\pm$0.8 GeV in accordance with the jet energy resolution,
- jet energy corrections obtained from P_T balancing method were applied instead of those obtained from comparison of hadron (parton) and detector levels in MC.

In Fig. 8.9 the dijet cross section differences at the hadron and parton levels caused by above mentioned cuts changes are shown. The thick solid line describes the total dijet cross section calculated in NLO approximation using Mepjet 2.0 program, whereas the thin solid line indicates the default (see cuts in Tab. 8.1) measured cross section.
The most significant errors come from the use of different MC models for corrections, the jet energy scale and resolution uncertainties.
As can be seen from Fig. 8.9.b the theoretical calculations are much below quite significant errors connected with corrections to the parton level.

To explore theoretical calculation uncertainties the following aspects were taken into account:

- different structure functions (CTEQ4M, MRSA, GRV),
- the factorization/renormalization scale was changed from $\mu_F^2 = \mu_R^2 = Q^2$ (from now on called Q scale) to $\mu_F^2 = \mu_R^2 = 0.25 * (P_T^{HCM})^2$, where P_T^{HCM} is the sum of the transverse momentum of the jets in the center-of-mass frame (from now on called P_T scale),
- the P_T scale was changed from: 1.0*P_T to: 0.5*P_T and 2.0*P_T.

Fig. 8.10 shows the influence of theoretical uncertainties on dijet NC DIS cross section and the results are listed in Tab. 8.3. The scale change in analytical NLO calculations has the highest impact.

8.6 High or asymmetric E_T jet cuts

In order to investigate to what extend the observed discrepancies between the analytical NLO calculations and the measurement depend on the jet selection criteria we have changed them as compared to the default ones (see Tab. 8.1). At first, the cut on the jet transverse momentum was increased and also the asymmetric cuts were used as proposed recently [74].

It was found that the higher jet transverse momentum the more uniquely the jets are identified and the different jet finding algorithms lead to the similar results. In Fig. 8.11.a we compare experimental and theoretical total cross sections dependence on higher p_T cuts for both jets transverse momenta in the hadronic center of mass frame, whereas the jet cut

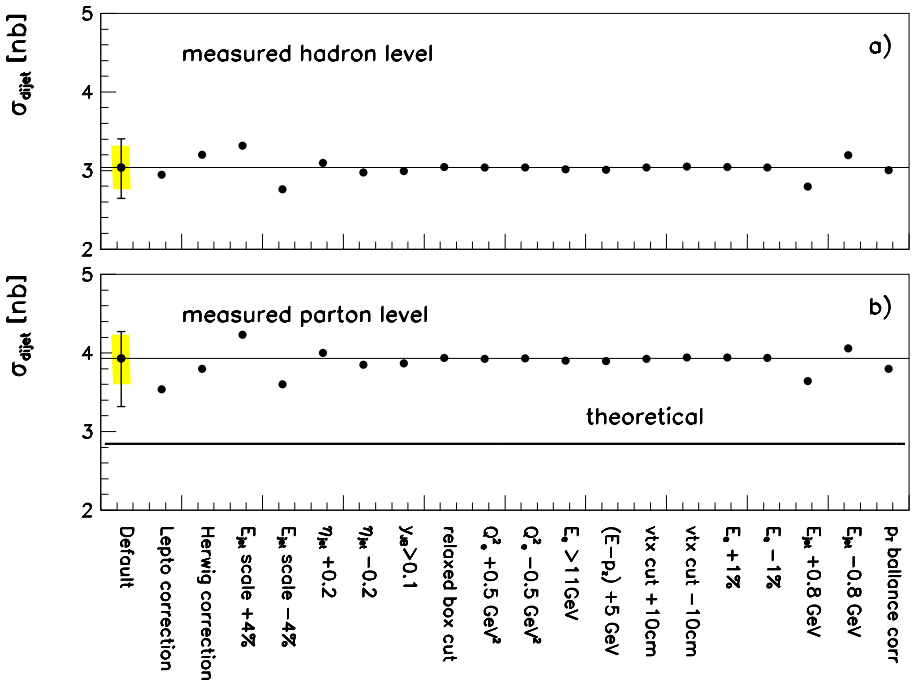

Figure 8.9: *Systematic uncertainties on the integrated dijet cross section measured at the hadron and parton level. The positive (negative) error bars on the default values were obtained by adding all positive (negative) contributions in quadrature. The shaded band shows the uncertainty from the jet energy scale. The thick solid line indicates theoretical predictions generated with Mepjet 2.0 MC using CTEQ4M structure function, Q scale and default selection criteria (see Tab. 8.1). The thin solid line indicates the default (see cuts in Tab. 8.1) measured value of cross section.*

structure function	scale	$\sigma_{Mepjet2.0} \pm$ stat [nb]
CTEQ4M	Q	2.84 ± 0.03
GRV	Q	2.90 ± 0.03
MRSA	Q	2.63 ± 0.03
CTEQ4M	P_T	2.43 ± 0.03
CTEQ4M	$0.5^* P_T$	2.49 ± 0.03
CTEQ4M	$2.0^* P_T$	2.48 ± 0.03

Table 8.3: *The comparison of theoretical integrated cross sections at the parton level calculated with different structure functions and different factorization/renormalization scales.*

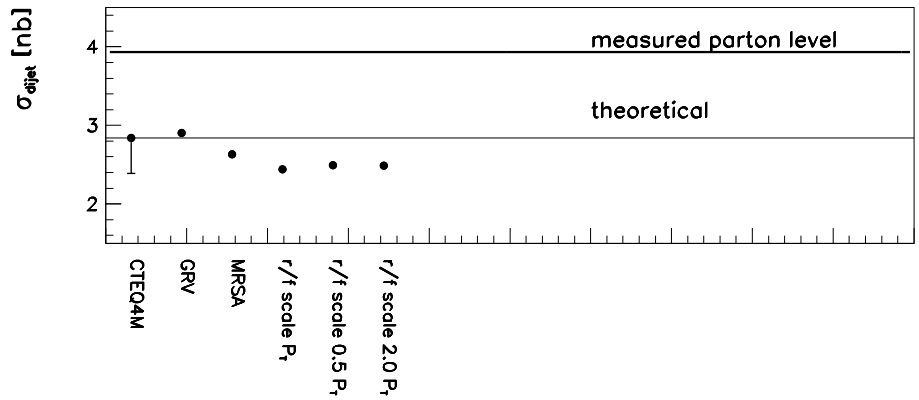

Figure 8.10: *Systematic uncertainties on the analytical calculations of integrated dijet cross section. Thick solid line indicates default (see cuts in Tab. 8.1) measured cross section, whereas thin solid line indicates the default (see cuts in Tab. 8.1) analytical predictions.*

	measurement	Mepjet 2.0 (P_T scale)	Mepjet 2.0 (Q scale)
$p_{T,HCM}$ [GeV]	$\sigma_{dijet} \pm$ stat [nb]	$\sigma_{Mepjet} \pm$ stat [nb]	$\sigma_{Mepjet} \pm$ stat [nb]
4	3.93 ± 0.04	2.44 ± 0.02	2.84 ± 0.03
5	2.56 ± 0.03	1.48 ± 0.02	1.71 ± 0.02
6	1.58 ± 0.02	0.87 ± 0.01	1.00 ± 0.02
7	0.97 ± 0.02	0.54 ± 0.01	0.60 ± 0.02
8	0.62 ± 0.01	0.35 ± 0.01	0.37 ± 0.02

Table 8.4: *The comparison of the measured and theoretical integrated cross sections at the parton level for different p_T cuts for both jets transverse momenta in the hadronic center of mass frame.*

in laboratory frame is not changed. The integrated dijet cross section, both theoretical and experimental, decreases as the cut increases, however, as indicated in Fig. 8.11.b the relative ratio of the two is roughly constant. The results are summarized in Tab. 8.4. The corresponding measured integrated dijet cross sections at hadron level and hadronization corrections, calculated as the ratio of hadron and parton level cross sections, are listed in Tab. 8.5.

The NLO QCD dijet cross section calculations for symmetric p_T jet cuts are not reliable but in the experiment this cross section can be measured accurately. This problem of analytical calculations is a feature of any fixed order calculation which gives large negative cross sections in the phase space region where both jets have almost identical transverse momenta. The problem in the prediction of the dijet rates for symmetric cuts on the

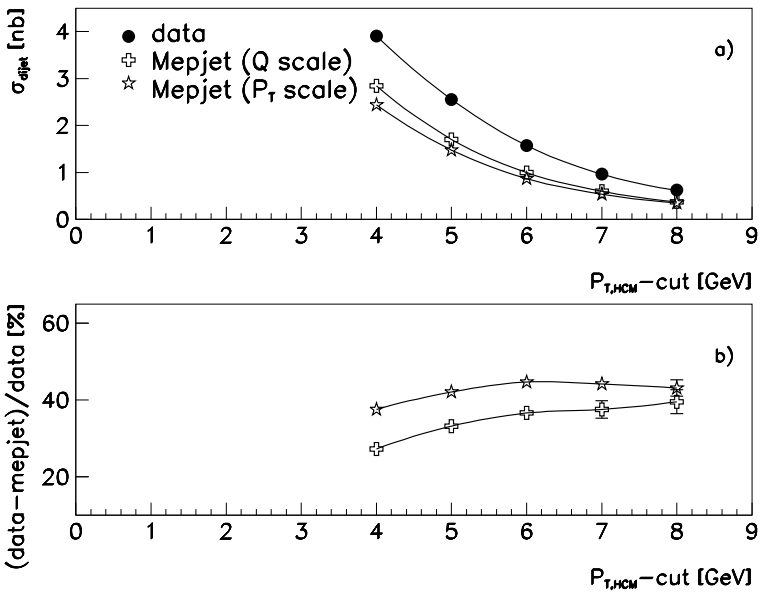

Figure 8.11: *Dependence of the total cross section on higher p_T cuts for both jets transverse momenta in hadronic center of mass frame (a). Measured parton level cross sections (black points) are compared to NLO calculations generated with Q scale (white crosses) and p_T scale (white stars). The relative difference of the measured and predicted cross sections is shown in (b). The error bars indicate the statistical error only.*

$p_{T,HCM}$ [GeV]	$\sigma_{dijet} \pm$ stat [nb]	hadronization corr.
4	3.04 ± 0.03	1.29
5	1.97 ± 0.02	1.30
6	1.23 ± 0.02	1.28
7	0.78 ± 0.01	1.24
8	0.50 ± 0.01	1.25

Table 8.5: *The integrated dijet cross sections at the hadron level for different p_T cuts for both jets transverse momenta in the hadronic center of mass frame and the hadronization corrections calculated as the ratio of parton (see Tab. 8.4) and hadron level cross sections.*

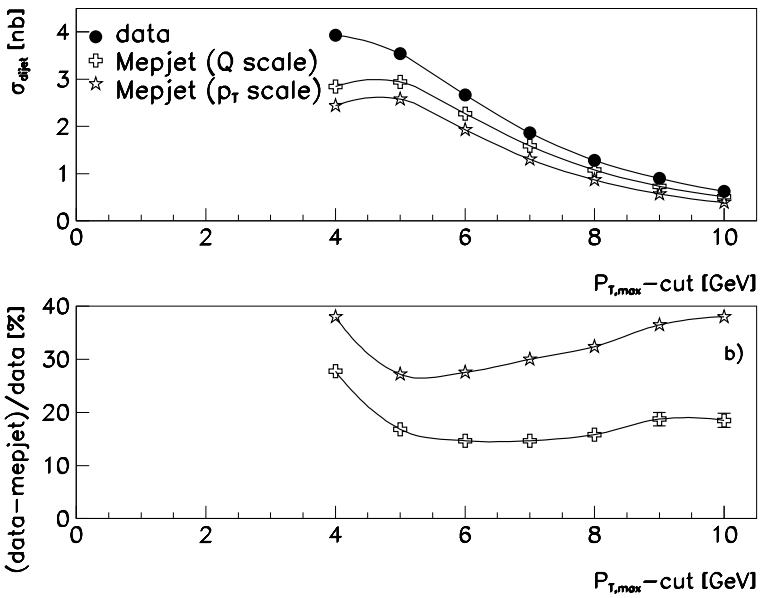

Figure 8.12: *Dependence of the total cross section on an additional p_T cut on the larger of the jet transverse momenta in the hadronic center of mass frame (a). Measured parton level cross sections (black points) are compared to NLO calculations generated with Q scale (white crosses) and p_T scale (white stars). The relative difference of the measured and predicted cross sections is shown in (b). The error bars indicate the statistical error only.*

jet transverse momenta (eg. see Tab. 8.1) has been noted for the phase space slicing method [75] and discussed in detail for this and the subtraction method in [76]. A correct treatment of this phase space region would need a resummation to all orders [77].
Recently, it was proposed [74] to measure the dijet rate using asymmetric cuts on the transverse momenta of the two jets. Following this suggestion we introduced an additional cut on the larger p_T of the jets in hadronic center of mass frame. The results, Fig. 8.12(a,b), show that as the cut increases both the measured and theoretical dijet cross sections decrease but the relative ratio still is pronounced. The results are listed in Tab. 8.6.
Corresponding measured integrated dijet cross sections at hadron level and hadronization corrections, calculated as the ratio of hadron and parton level cross sections, are listed in Tab. 8.7.

	measurement	Mepjet 2.0 (P_T scale)	Mepjet 2.0 (Q scale)
$p_{T,max}$ [GeV]	$\sigma_{dijet} \pm$ stat [nb]	$\sigma_{Mepjet} \pm$ stat [nb]	$\sigma_{Mepjet} \pm$ stat [nb]
4	3.93 ± 0.04	2.44 ± 0.02	2.84 ± 0.03
5	3.54 ± 0.04	2.58 ± 0.02	2.94 ± 0.03
6	2.66 ± 0.03	1.93 ± 0.02	2.27 ± 0.02
7	1.87 ± 0.03	1.31 ± 0.01	1.59 ± 0.02
8	1.28 ± 0.02	0.87 ± 0.01	1.08 ± 0.02
9	0.90 ± 0.02	0.57 ± 0.01	0.73 ± 0.02
10	0.63 ± 0.01	0.39 ± 0.01	0.51 ± 0.02

Table 8.6: *The comparison of the measured and the theoretical integrated cross sections at the parton level for an additional p_T cut on the larger of the jet transverse momenta the in hadronic center of mass frame.*

$p_{T,max}$ [GeV]	$\sigma_{dijet} \pm$ stat [nb]	hadronization corr.
4	3.04 ± 0.03	1.29
5	2.74 ± 0.03	1.29
6	2.10 ± 0.02	1.27
7	1.50 ± 0.02	1.24
8	1.05 ± 0.02	1.23
9	0.74 ± 0.01	1.23
10	0.52 ± 0.01	1.22

Table 8.7: *The integrated dijet cross sections at the hadron level for an additional p_T cut on the larger of the jet transverse momenta in the hadronic center of mass frame the hadronization corrections calculated as the ratio of parton (see Tab. 8.6) and hadron level cross sections.*

9 Determination of dijet cross section using k_T algorithm

In this section the differential and the integrated dijet cross sections for the jets identified in the laboratory frame with k_T type algorithm are presented. The experimental results are compared to the Monte Carlo models predictions and NLO theoretical calculations.

Since a jet is not a fundamental QCD object, it has to be found using a particular jet finding algorithm. All the presented analysis was repeated for jets found with k_T algorithm, as described in Section 6.2 . The k_T algorithm was applied in the laboratory frame and the same selection cuts, as in the case of the cone algorithm, were applied (see Table 8.1).

In Fig. 9.1 and Fig. 9.2 the experimental distributions of kinematical and jet variables are compared to the Monte Carlo models (Ariadne, Lepto and Herwig) at the detector level. From these models Ariadne is closest to the data, however $E - p_z$ is not reproduced by any MC. Herwig fails to reproduce the Q^2 distribution and high E_T jets tail is overestimated by all the models. As in the cone algorithm case, Ariadne gives the best overall description of the data and will be used for default corrections to the hadron and parton levels.

In Fig. 9.3 and Fig. 9.4 the measured differential cross sections at the hadron (parton) level and hadron (parton) level Monte Carlo predictions are shown. Ariadne reproduces the shape correctly but overestimates the rate. Lepto and Herwig models underestimate the rate, whereas reproduce roughly the shapes, except that Herwig fails to describe the Q^2 distribution. NLO analytical calculations show reasonable agreement in shape but also underestimate the cross section.
Relevant purities, efficiencies, correction factors obtained by comparing true (hadronic or partonic) and detector levels are shown in Appendix A in Fig. A.3 and Fig. A.4, whereas differential cross section values and errors are collected in Tab. A.3 and Tab. A.4.

Integrated over the selected kinematic region, the total dijet cross sections at the hadron and parton levels and those obtained with Ariadne, Lepto, Herwig and Mepjet 2.0 are compared in Tab. 9.1. Ariadne MC overestimates both the hadron and parton level total cross section by about 17%, whereas Lepto and Herwig MC underestimate it by about 50%. QCD NLO calculations also underestimate the total dijet cross section by 24%.

In the next plots the systematic errors in the integrated cross section determination at the hadron and parton levels (Fig. 9.5) as well as theoretical calculation uncertainties (Fig. 9.6) are shown.
The most significant errors, in the measurement, come from the use of different Monte Carlo models for corrections, the jet energy scale and resolution uncertainty, whereas the scale change in theoretical NLO calculations causes highest dijet rate changes.

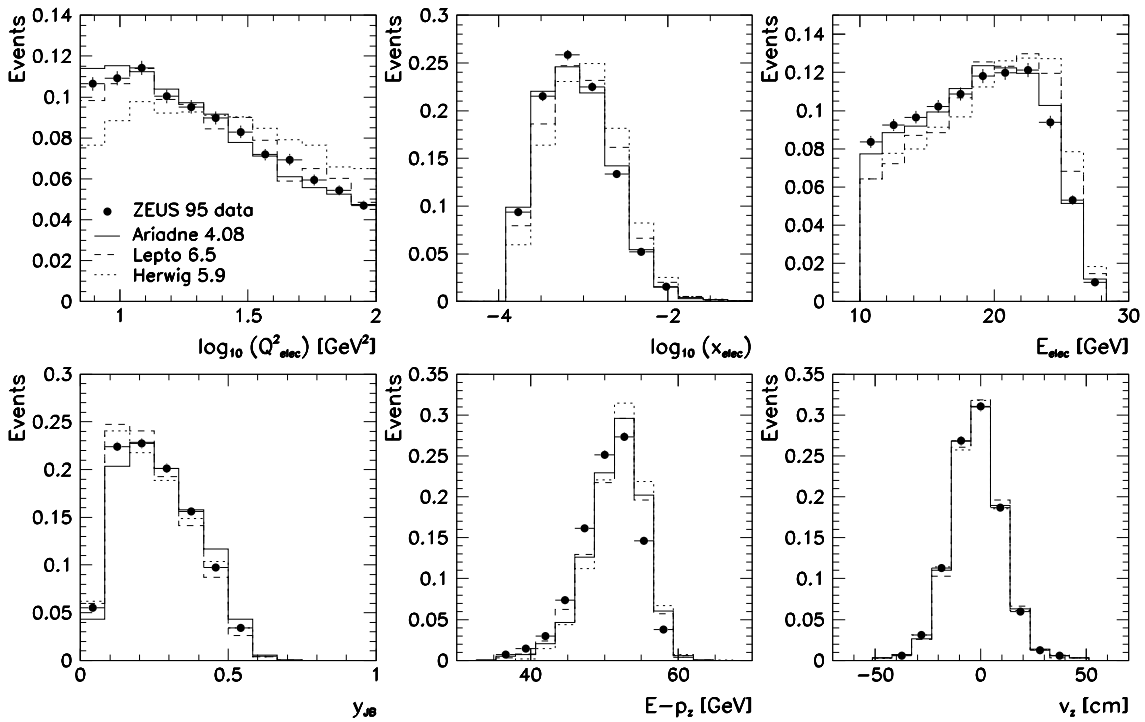

Figure 9.1: *Distribution comparison of kinematical variables Q^2_{elec}, x_{elec}, E_{elec} (reconstructed with the electron method), y_{JB} (reconstructed with the Jacquet-Blondel method), $E - p_z$ and v_z (reconstruction vertex)) between data (black points), Ariadne (solid line), Lepto (dashed line) and Herwig (dotted line) at the detector level. Only statistical errors are shown. Jets were reconstructed using the k_T algorithm.*

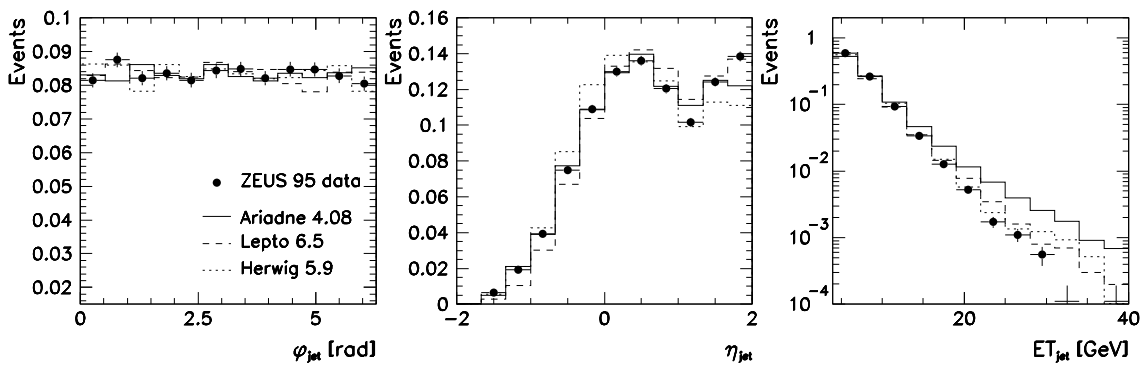

Figure 9.2: *Jet variable distribution comparison: azimuthal angle (ϕ), pseudorapidity (η), transverse energy (E_T) between data (black points), Ariadne (solid line), Lepto (dashed line) and Herwig (dotted line) at the detector level. Only statistical errors are shown. Jets were reconstructed using the k_T algorithm.*

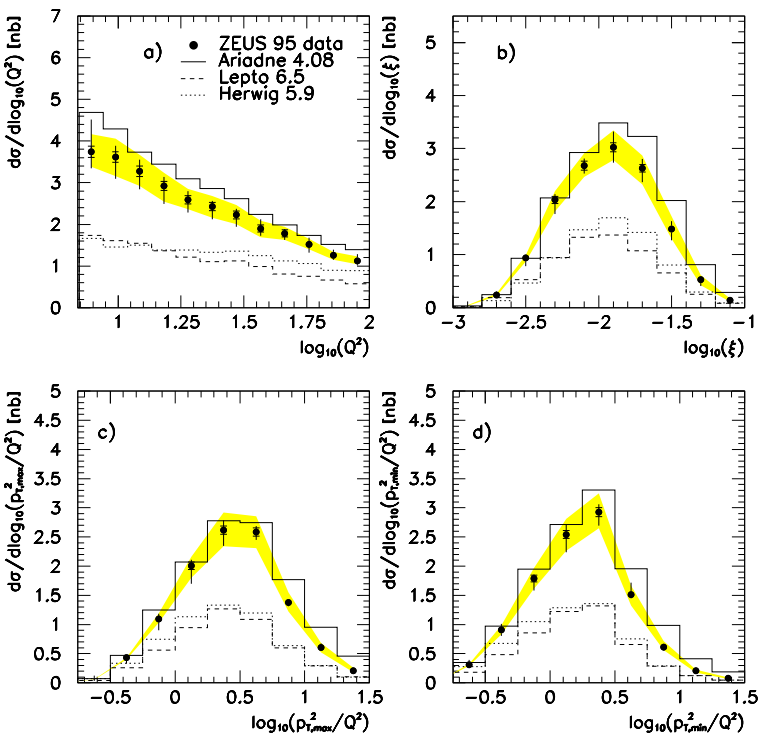

Figure 9.3: *Differential dijet cross section at hadron level versus a) Q^2, b) ξ, c) $p^2_{T,max}/Q^2$, d) $p^2_{T,min}/Q^2$. The inner(outer) bars indicate the statistical error (statistical and systematical errors added in quadrature). Shaded area shows jet energy scale uncertainty. The measured cross sections corrected to hadron level (black points) are compared to MC models Ariadne (solid line), Lepto (dashed line), Herwig (dotted line). Jets were reconstructed using the k_T algorithm.*

results	parton level σ_{dijet} [nb]	hadron level σ_{dijet} [nb]
ZEUS 95 data	$3.74\pm 0.04(\text{stat})^{+0.38}_{-0.62}$ (sys)	$2.74\pm 0.03(\text{stat})^{+0.34}_{-0.39}$ (sys)
Mepjet 2.0	2.85 ± 0.03 (stat)$^{+0.01}_{-0.47}$ (sys)	
Ariadne 4.08	4.34 ± 0.05 (stat)	3.23 ± 0.04 (stat)
Lepto 6.5	1.71 ± 0.02 (stat)	1.30 ± 0.02 (stat)
Herwig 5.9	1.90 ± 0.03 (stat)	1.48 ± 0.02 (stat)

Table 9.1: *Comparison of experimentally measured cross sections with MC predictions. Jets were reconstructed using the k_T algorithm.*

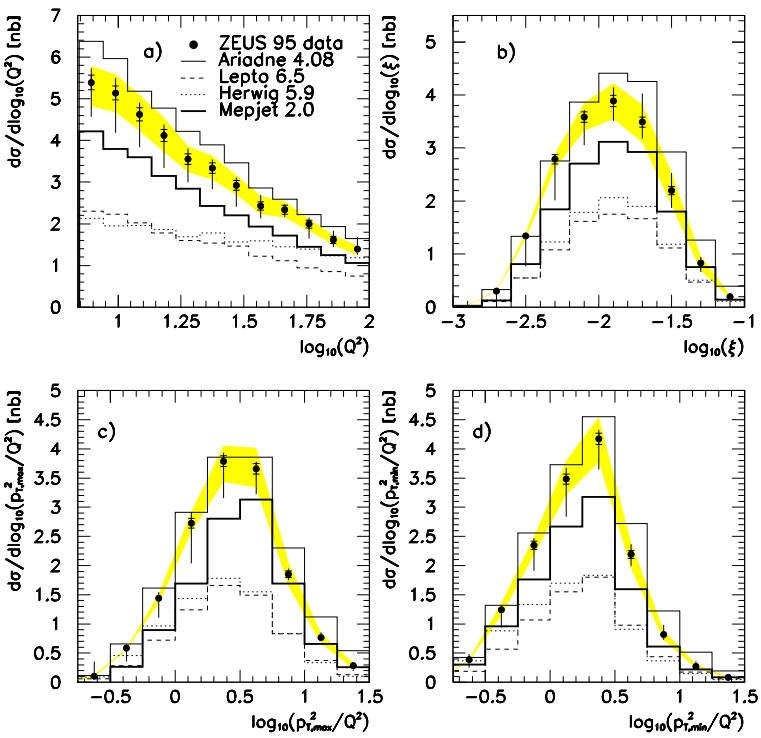

Figure 9.4: *Differential dijet cross section at parton level versus a) Q^2, b) ξ, c) $p^2_{T,max}/Q^2$, d) $p^2_{T,min}/Q^2$. The inner (outer) bars indicate the statistical error (statistical and systematical errors added in quadrature). Shaded area shows jet energy scale uncertainty. The measured cross sections corrected to parton level (black points) are compared to MC models Ariadne (solid line), Lepto (dashed line), Herwig (dotted line) and NLO calculations. Jets were reconstructed using the k_T algorithm.*

structure function	scale	$\sigma_{Mepjet2.0} \pm$ stat [nb]
CTEQ4M	Q	2.85 ± 0.03
GRV	Q	2.92 ± 0.03
MRSA	Q	2.62 ± 0.03
CTEQ4M	P_T	2.48 ± 0.02
CTEQ4M	$0.5^* P_T$	2.47 ± 0.02
CTEQ4M	$2.0^* P_T$	2.47 ± 0.02

Table 9.2: *Comparison of theoretical integrated cross sections at the parton generated with different structure functions and different factorization/renormalization scales. Jets were reconstructed using the k_T algorithm.*

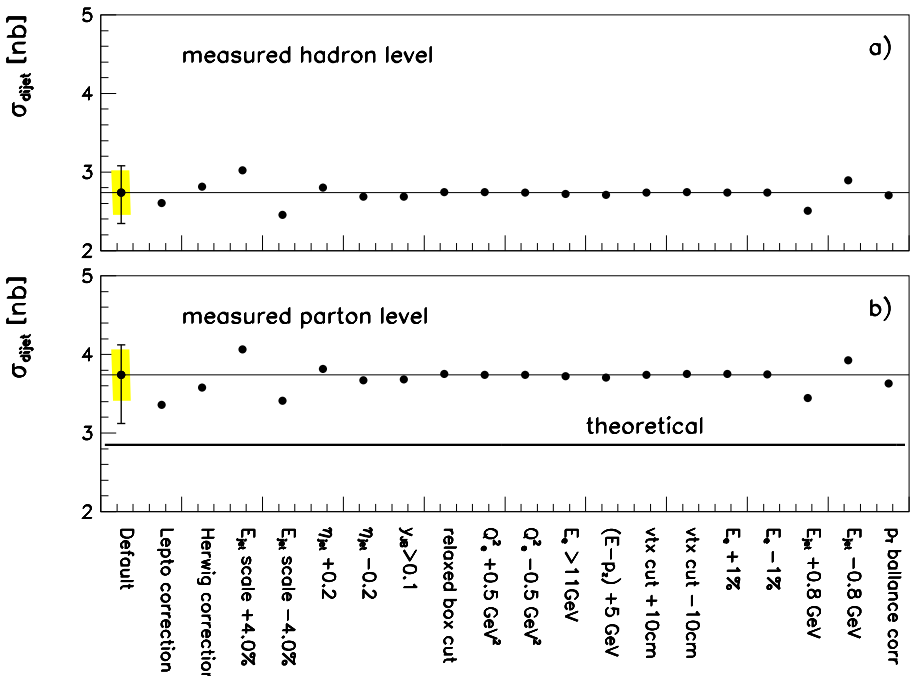

Figure 9.5: *Systematic uncertainties on the integrated dijet cross section measured at the hadron and parton level. The positive (negative) error bars on the default values were obtained by adding all positive (negative) contributions in quadrature. The shaded band shows the uncertainty from the jet energy scale. The thick solid line indicates theoretical predictions generated with Mepjet 2.0 MC using CTEQ4M structure function, Q scale and default selection criteria (see Tab. 8.1). The thin solid line indicates the default (see cuts in Tab. 8.1) measured value of cross section. Jets were reconstructed using the k_T algorithm.*

As in the case of the cone algorithm studies, the influence of higher and asymmetric transverse momentum jet cuts on the relative difference between the theory NLO calculations and experimental measurement was investigated.
In Fig. 9.7.a the experimental and the theoretical integrated cross sections dependence on higher p_T cuts on the transverse momenta of both jets in the hadronic centre of mass were compared without the change of the jets cut in the laboratory frame. The dijet cross section, both theoretical and experimental, decreases as the cut increases, however as indicated in Fig. 9.7.b the relative ratio is of the two remains approximately constant. The results are listed in Tab. 9.3.
Corresponding measured integrated dijet cross sections at hadron level and hadronization corrections are listed in Tab. 9.4.

In Fig. 9.8.a an additional cut on the larger p_T of the jets in hadronic center of mass frame was introduced. The results show that as p_T increases both the measured

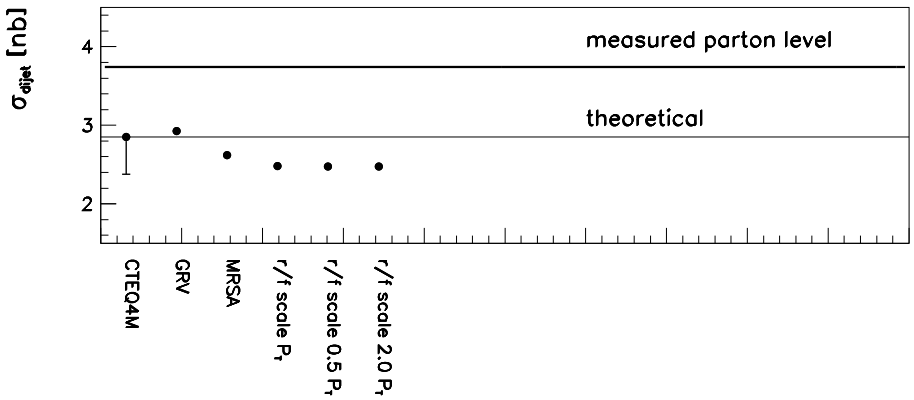

Figure 9.6: *Systematic uncertainties on the analytical calculations of integrated dijet cross section. Thick solid line indicates default measured cross section, whereas thin solid line indicates the default (see cuts in Tab. 8.1) analytical predictions. Jets were reconstructed using the k_T algorithm.*

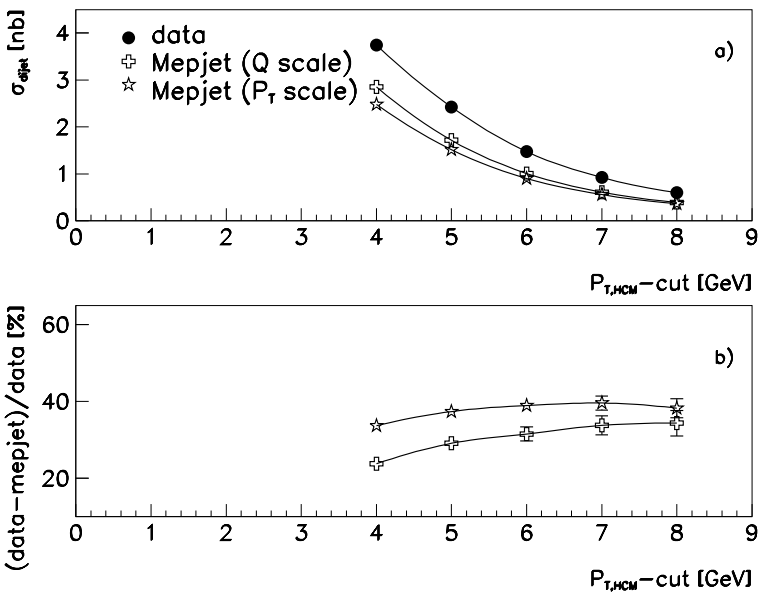

Figure 9.7: *Dependence of the total cross section on higher p_T cuts on both jets transverse momenta in hadronic center of mass frame (a). Measured parton level cross sections (black points) are compared to NLO calculations generated with Q scale (white crosses) and p_T scale (white stars). The relative difference of the measured and predicted cross sections is shown in (b). The error bars indicate the statistical error only. Jets were reconstructed using the k_T algorithm.*

	measurement	Mepjet 2.0 (P_T scale)	Mepjet 2.0 (Q scale)
$p_{T,HCM}$ [GeV]	$\sigma_{dijet} \pm$ stat [nb]	$\sigma_{Mepjet} \pm$ stat [nb]	$\sigma_{Mepjet} \pm$ stat [nb]
4	3.74 ± 0.04	2.48 ± 0.02	2.85 ± 0.03
5	2.42 ± 0.03	1.52 ± 0.02	1.72 ± 0.02
6	1.48 ± 0.02	0.90 ± 0.01	1.01 ± 0.02
7	0.93 ± 0.02	0.56 ± 0.01	0.61 ± 0.02
8	0.60 ± 0.01	0.37 ± 0.01	0.39 ± 0.02

Table 9.3: *Comparison between measured and theoretical integrated cross sections at the parton level for an additional p_T cut on the jet transverse momenta the in hadronic center of mass frame. Jets were reconstructed using the k_T algorithm.*

$p_{T,HCM}$ [GeV]	$\sigma_{dijet} \pm$ stat [nb]	hadronization corr.
4	2.74 ± 0.03	1.36
5	1.78 ± 0.03	1.37
6	1.10 ± 0.02	1.35
7	0.71 ± 0.01	1.30
8	0.46 ± 0.01	1.31

Table 9.4: *The integrated dijet cross sections at the hadron level for different p_T cuts for both jets transverse momenta in the hadronic center of mass frame and the hadronization corrections calculated as the ratio of parton (see Tab. 9.3) and hadron level cross sections.*

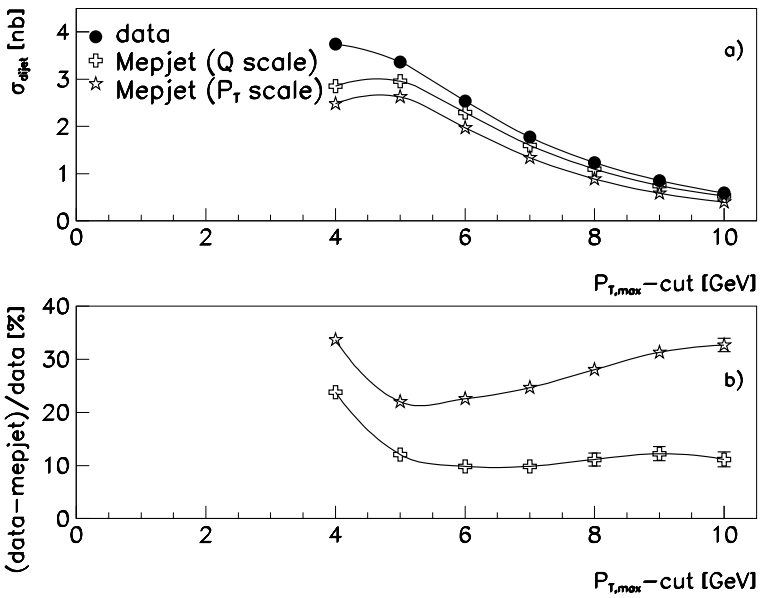

Figure 9.8: *Dependence of the total cross section on an additional p_T cut on the larger of the jet transverse momenta in hadronic center of mass frame (a). Measured parton level cros sections (black points) are compared to NLO calculations generated with Q scale (white crosses) and p_T scale (white stars). The relative difference of the measured and predicted cross sections is shown in (b). The error bars indicate the statistical error only. Jets were reconstructed using the k_T algorithm.*

and the theoretical dijet cross sections decrease and the relative ratio Fig. 9.8.b remains substantial. The results are listed in Tab. 9.5.
Corresponding measured integrated dijet cross sections at hadron level and hadronization corrections are listed in Tab. 9.6.

The results obtained with the cone and the k_T jet finding algorithms are similar. The shape of kinematical and jet variables' distributions is reasonably reproduced by Ariadne MC and NLO analytical calculations and roughly described by Lepto, Herwig models. Again Herwig fails to reproduce the Q^2 distribution. Ariadne overestimates the dijet rate, whereas Lepto, Herwig and NLO calculations underestimate it.
Neither an increase of the jet p_T cuts nor the use of asymmetric cuts leads to the agreement between data and NLO calculations.

The gluon density function was not unfolded, because no agreement between NLO analytical calculations and measured data was obtained neither by changing jet selection criteria nor by applying different jet finding procedures.

One should note the recent observation of H1 Collaboration [25] [26], which found that the two jet cross section is well reproduced by the theoretical predictions. However their

	measurement	Mepjet 2.0 (P_T scale)	Mepjet 2.0 (Q scale)
$p_{T,max}$ [GeV]	$\sigma_{dijet} \pm$ stat [nb]	$\sigma_{Mepjet} \pm$ stat [nb]	$\sigma_{Mepjet} \pm$ stat [nb]
4	3.74 ± 0.04	2.48 ± 0.02	2.85 ± 0.03
5	3.36 ± 0.03	2.62 ± 0.02	2.96 ± 0.02
6	2.54 ± 0.03	1.97 ± 0.02	2.29 ± 0.02
7	1.78 ± 0.02	1.34 ± 0.01	1.60 ± 0.02
8	1.24 ± 0.02	0.89 ± 0.01	1.10 ± 0.02
9	0.86 ± 0.01	0.59 ± 0.01	0.75 ± 0.02
10	0.60 ± 0.01	0.40 ± 0.01	0.53 ± 0.02

Table 9.5: *The comparison of the measured and the theoretical integrated cross sections at the parton level for an additional p_T cut on the larger of the jet transverse momenta in the hadronic center of mass frame.*

$p_{T,max}$ [GeV]	$\sigma_{dijet} \pm$ stat [nb]	hadronization corr.
4	2.74 ± 0.03	1.36
5	2.47 ± 0.03	1.36
6	1.93 ± 0.02	1.32
7	1.39 ± 0.02	1.28
8	0.98 ± 0.02	1.26
9	0.69 ± 0.01	1.23
10	0.49 ± 0.01	1.21

Table 9.6: *The integrated dijet cross sections at the hadron level for an additional p_T cut on the larger of the jet transverse momenta in the hadronic center of mass frame the hadronization corrections calculated as the ratio of parton (see Tab. 9.5) and hadron level cross sections.*

conclusions are based on assumption that hadronization does not effect significantly (9-25 % for medium momentum transfer squared whereas 4-8 % for high momentum transfer squared and high and asymmetric transverse momentum jet cuts) the parton level and therefore they can compare hadron level with the parton level NLO QCD calculations.

10 Dijet decorrelation as a probe of BFKL dynamics

In inclusive dijet production the azimuthal angle between the two highest pseudorapidity jets ($\Delta\phi$) in hadronic centre of mass (HCM) frame in different bins of x was analyzed and compared to MC models.

Jets were identified using a cone (k_T) algorithm in the laboratory frame. At the detector level, the jet finding was performed using calorimeter cells remaining after the removal of these which contained energy deposited by the scattered electron. The same algorithm was also used for hadrons and partons of the MC samples. The reconstructed jets were required to have a minimum transverse energy $E_T > 4$ GeV in both the laboratory and the hadronic center of mass (HCM) frames. Although a lower E_T cut is preferable, since at small values of ξ (longitudinal fraction of the proton's momentum carried by the interacting gluon) the BFKL dynamics effects are expected to be more pronounced, it would ruined the clear jet identification.
The jets were also required to have pseudorapidity in the range -2 $< \eta_{LAB} <$ 2.2 in the laboratory frame, which separates them from possible proton remnant contamination, and in HCM frame $\eta_{HCM} > 0.0$ to select only jets in the photon fragmentation hemisphere. Events with at least two jets were accepted. In addition to the jet selection criteria the following requirements were set: $Q^2 > 8$ GeV^2, $y > 0.04$ and scattered electron energy $E_{e'} > 10$ GeV.
The selection criteria are listed in Table 10.1.

$Q^2 > 8$ GeV^2
$E_{e'} > 10$ GeV
$p_{T,LAB} > 4$ GeV
$p_{T,HCM} > 4$ GeV
-2 $< \eta_{LAB} <$ 2.2
$\eta_{HCM} > 0.$
number of identified jets >= 2

Table 10.1: *Selection phase space region for the dijet decorrelation measurement.*

In Fig. 10.1 and Fig. 10.2 the comparison at the hadron and parton levels of data and MC models for cone and kt algorithms is shown. All the distributions are normalized to unity. This way the different absolute normalization of data and MC can be forgotten and the shape of the dijet azimuthal distribution can be studied.

Ariadne approach is called BFKL-like because gluons emitted in the cascade do not obey a strong ordering in the transverse momentum while the other two programs are based on DGLAP evolution equations. So one could expect the Ariadne dijets to be more decorrelated.

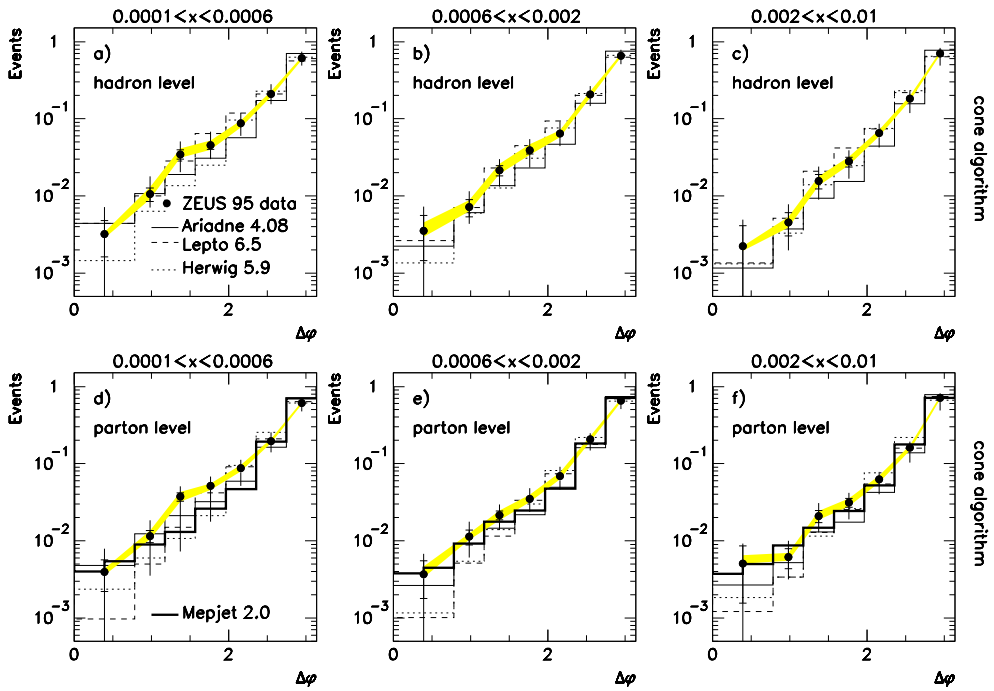

Figure 10.1: *Comparison of $\Delta\phi$ distribution for data and Ariadne (solid line), Lepto (dashed line) and Herwig (dotted line) in three different bins of x at the hadron (a,b,c) and parton (d,e,f) levels. All the histograms are normalized to unity. The inner (outer) error bars indicate the statistical error (statistical and systematical errors added in quadrature). Shaded area shows jet energy scale uncertainty. Jets were identified using the cone algorithm.*

In the highest $\Delta\phi$ bin Ariadne predictions overshoots Lepto and Herwig. For the medium $\Delta\phi$ bins Ariadne curve is below the DGLAP based models. In lower $\Delta\phi$ bins Ariadne overshoots the other models, however these bins are of the smallest statistical significance and data points show huge errors mainly coming from the use of different models for correcting for detector and hadronization effects.

The data can not distinguish between different models neither on hadron nor parton levels. Relative difference between data and various models does not change significantly with decreasing x.
At the parton level the measured shape of the $\Delta\phi$ distribution is reproduced within the errors by NLO conventional QCD calculations obtained with the program Mepjet 2.0. As it has already been mentioned (see Section 8.6) NLO predictions may not be reliable for symmetric transverse momentum jet cuts since one can observe the existence of large positive and negative terms for nearly back-to-back jets. To minimize their influence i.e. to cancel them a wide bin around $\Delta\phi$ has to be used. Since the asymmetric jet cuts studies also have not led to the satisfactory agreement between NLO calculations and the

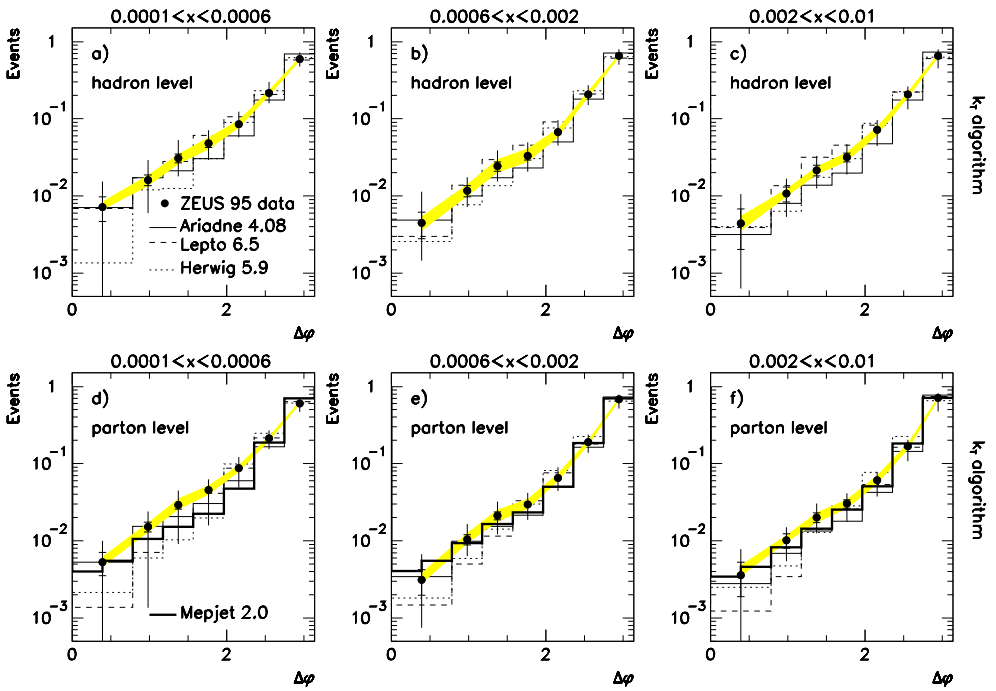

Figure 10.2: *Comparison of $\Delta\phi$ distribution for data and Ariadne (solid line), Lepto (dashed line) and Herwig (dotted line) in three different bins of x at the hadron (a,b,c) and parton (d,e,f) levels. All the histograms are normalized to unity. The inner (outer) error bars indicate the statistical error (statistical and systematical errors added in quadrature). Shaded area shows jet energy scale uncertainty. Jets were identified using the k_T algorithm.*

data (see Section 8.6 and 9) they were not used in the decorrelation studies.

The calculations in LO BFKL resummation were made for different kinematical region [29] than that for which most of the experimental analysis of two jet production (including this one) were done. Since BFKL calculations in our kinematical region were not available they were not compared to the data.

It should be pointed out that the decorrelation effect was calculated only in LO BFKL resummation and its prediction can be significantly changed in NLO BFKL approximation.

11 Summary

In this thesis the results of the measurement of the neutral current DIS dijet cross section is presented. The analysis is based on the data sample corresponding to 6.1 pb^{-1} collected in 1995 with the ZEUS detector at the HERA accelerator.

Jets were reconstructed in the laboratory frame using the cone algorithm. The reconstructed jets were required to have a minimum transverse energy E_T of 4 GeV in both the laboratory and the hadronic center of mass frames and a pseudorapidity in the range -2 $< \eta <$ 2 in the laboratory frame. Only two jet events satisfying the following selection criteria: 7 GeV^2 $< Q^2 <$ 100 GeV^2, $y > 0.04$ and scattered positron energy $E_{e'} > 10$ GeV were accepted.

The jet shape studies were performed. The integrated and the differential jet shapes were compared to the Monte Carlo models (Ariadne,Lepto,Herwig) predictions. Ariadne model fairly well describes the data, whereas Lepto and Herwig are in qualitative agreement with data. Moderate increase of a jet's width with increasing jet transverse energy is observed. This is in agreement with the QCD predictions.

Since the jet energy scale in data and Monte Carlo is different and represents the major contribution to systematic error in the jet studies, the new method based on P_T balancing in event was applied and it was found that this difference amounts to 4.0%.

The shapes of measured differential cross sections at the hadron and the parton levels are reasonably well reproduced by Ariadne and NLO (at the parton level) analytical calculations. Lepto and Herwig are in rough agreement with the data, except Q^2 distribution which is not reproduced by Herwig.
The measured integrated dijet cross sections at the hadron and parton levels are:

$$\sigma_{exp}^{hadr} = 3.04 \pm 0.03(stat)^{+0.36}_{-0.39}(sys)$$

$$\sigma_{exp}^{part} = 3.93 \pm 0.04(stat)^{+0.34}_{-0.61}(sys)$$

and were compared to MC predictions. Ariadne overestimates measured cross sections by about 14% whereas Herwig and Lepto underestimate it by about 50%. At the parton level QCD NLO analytical calculations underestimate the total cross section by about 28%.
The hadronization uncertainties estimated on the basis of different Monte Carlo models, and the energy scale uncertainties are the major contributions to the systematic error.

The observed discrepancy between the data and theory led to further investigations. Higher transverse energy cuts and asymmetrical transverse energy cuts were applied. These cuts decrease both the measured and the calculated cross sections and the difference between them remains substantial.

The analysis was repeated with the same cuts but for jets found using k_T algorithm. The measured integrated dijet cross sections at the hadron and parton levels are in this case:

$$\sigma_{exp}^{hadr} = 2.74 \pm 0.03(stat)^{+0.34}_{-0.39}(sys)$$

$$\sigma_{exp}^{part} = 3.74 \pm 0.04(stat)^{+0.38}_{-0.62}(sys)$$

and were compared to MC predictions. Ariadne MC overestimates both the hadron and parton level total cross sections by about 17%, whereas Lepto and Herwig MC underestimate them by about 50%. QCD NLO calculations at the parton level also underestimate the total dijet cross section by about 24%.

Therefore both cone and k_T algorithms lead to the very similar results and the difference between measured and QCD calculated cross sections cannot be accounted for by different jet selection criteria (higher E_T cuts and asymmetric E_T cuts).

From the analysis of the two jet events data one could extract the proton gluonic structure function assuming that QCD predictions reproduce data. Since however we do observe a clear disagreement between the two this extraction would be meaningless.

In inclusive NC DIS dijet production the jet decorrelation as a possible sign of BFKL dynamics was investigated. This effect was predicted in LO BFKL resummation and is expected to be much stronger than in conventional DGLAP approach. However, the NLO conventional QCD calculations show, within the errors, the shape agreement with the data. Since LO BFKL calculations were not available in the kinematical region proposed in this thesis they were not compared to the data.
It should be pointed out that NLO BFKL calculations can lead to significant corrections to decorrelation effect.

Acknowledgments

I would like to thank my supervisor Professor Andrzej Eskreys for his guidance during my Ph.D studies and for giving me the opportunity to work within the ZEUS Collaboration at DESY. I am also very grateful for a careful reading of the manuscript.

I am grateful to Dr. José Repond for the numerous discussions on the details of the analysis.

I wish to thank my colleagues with whom I closely worked, Michael Riveline and Douglas Chapin, for fruitful cooperation and discussions on various issues concerning the analysis. I would like also to thank Douglas Chapin for correcting my English style.

I wish to thank Dr. Janusz Chwastowski, Dr. Mariusz Przybycień, Leszek Adamczyk, Dr Leszek Zawiejski and Professor Witold Krasny, for many discussions and support in solving numerous problems.

I am grateful to Dr. Krzysztof Golec-Biernat and Professor Jan Kwieciński for explaining the theoretical aspects of analysis to me.

I thank Agnieszka Czermak for hard work on my English style.

Last but not least, I would like to thank my parents for their continuous love, support, encouragement and understanding. This work would not have been possible without them.

Bibliography

[1] J.D.Bjorken, *Phys.Rev.* **179** (1969) 1547.

[2] A.D.Martin *Contemporary Physics 1995*,Volume **36**,numer 5,pages 335-353.

[3] L.N.Hand, *Phys.Rev.* **120** (1963) 1834.
F.J.Gilman, *Phys.Rev.* **167**(1967)1365.

[4] A.Bodek,et al., *Phys.Rev.* **D20** (1979) 1471.

[5] C.G.Callan and D.J.Gross, *Phys.Rev.* **22** (1969) 156.

[6] R.Taylor, *Inelastic Electron-Nucleon Experiments* Int'l Symposium on Lepton and Photon Interactions at High Energy(1975) 679.

[7] ZEUS Collaboration, M. Derrick et al., *Phys.Lett.* **B363** (1995) 201.

[8] J.Blümlein, *Z.Phys.* **C47** (1990) 89.

[9] L.Montanet et al, *Phys.Rev.* **50** (1994) 1173-1825

[10] J.Kripfganz, H.J.Möhring, H.Spiesberger, *Z.Phys.* **C49** (1991) 501.

[11] R.Brock et al., *Rev.Mod.Phys.* **67**(1995)157.

[12] G.Altarelli and G.Parisi, *Nucl. Phys.* **B126** (1977) 298.
V.N.Gribov and L.N.Lipatov, *Sov. Jour. Nucl. Phys.* **15** (1972) 438.

[13] Yu.Dokshitzer, *Soviet Phys.* JETP **46** (1977) 641.

[14] A.Mueller, *Nucl.Phys. B(Proc.Suppl.)* **18C** (1990) 125.

[15] Y.Balitskij and L.Lipatov, Sov.J.Nucl Phys. **28** (1978) 822.
E.Kuraev,L.Lipatov and V.Fadin, Sov.Phys.JETP **44** (1976) 443.
E.Kuraev,L.Lipatov and V.Fadin, Sov.Phys.JETP **45** (1977) 199.

[16] V.S.Fadin, L.N.Lipatov, *Phys.Lett.* **B429** (1998) 127.

[17] L.V.Gribov, E.M.Levin and M.G.Ryskin, *Phys.Rep.* **100** (1983) 1.
E.M.Levin, Orsay Lectures, LPTHE 91/02(1991).

[18] J.Bartels and M.G.Ryskin, *DESY preprint 93-081(1993).*

[19] A.D.Martin, R.G.Roberts, W.J.Stirling, *Phys.Lett.* **B354** (1995) 155.
A.D.Martin, R.G.Roberts, W.J.Stirling, *RAL-TR-96-037* (1996).

[20] M.Gluck, E.Reya, A.Vogt, *Z.Phys.* **C67**(1995)433.

[21] H.Abramowicz, in *Proceedings of the International Conference on High Energy Physics* (Warsaw, Poland, 1996)
H1 Collab., S.Aid et al., *Nucl.Phys.* **B470**(1996)3.

[22] ZEUS Collab., M.Derrick et al.,ICHEP96,pa02-047.

[23] D.Graudenz, M.Hampel, A.Vogt, Ch.Berger *The Mellin Transform Technique for the Extraction of the Gluon Density*, hep-ph/9506333.

[24] H1 Collaboration, S.Aid et al., DESY 95-086 (1995).

[25] H1 Collaboration, S.Aid et al., DESY 98-076 (1998)

[26] H1 Collaboration, *Measurement of Dijet Cross Sections in Deep-Inelastic Scattering at HERA and a Direct DEtermination of the Gluon Density in the Proton*, Submitted to the 29th Conference on High-Energy Physics ICHEP98.

[27] ZEUS Collaboration, J.Breitweg et al., *DESY 98-050.*

[28] H1 Collaboration, C.Adlof et al., *Nucl.Phys.* **B485** (1997) 3.

[29] A.J.Askew,D.Graudenz,J.Kwiecinski,A.D.Martin *Phys.Lett.* **B338** (1994) 92-97.

[30] G.Wolf HERA Physics *DESY 94-022*

[31] ZEUS Collaboration, *The ZEUS detector*, Status Report 1993, DESY

[32] J.Kruger, *Internal Report* DESY F35-92-02 Januay 1992.

[33] C.Alvisi et al., *Nucl.Instr and Meth.* **A305** (1991) 30.

[34] B.Foster et al., *Nucl.Instr and Math.* **A338** (1994) 254.

[35] ZEUS Collaboration, *Proposal for a Hadron-Electron Separator in the ZEUS Forward and Barrel Calorimeters.* ZEUS-Note 91-044.

[36] A.Bamberger, et all., *The Small Angle Rear Track Detector for ZEUS.* ZEUS Note 95-095.

[37] A.Bornheim et, all *The Presampler for FCAL and RCAL in ZEUS.* ZEUS Note 95-130.

[38] K.Piotrzkowski, M.Zachara *Determination of the ZEUS luminosity in '93.* ZEUS Note 94-167.

[39] K.Piotrzkowski, *Experimental Aspects of the Luminosity Measurenment in the ZEUS Experiment* DESY-F35D-93-06, Oct 1993, Ph.D.Thesis

[40] H.Bethe and W.Heitler, *Proc.Roy.Soc.* **A146** (1934) 83.

[41] I.Ali et all., *The ZEUS calorimeter first level trigger*, DESY 94-183.

[42] H.Uijterwaal *The second level trigger for ZEUS.* Ph.D.Thesis

[43] W.H.Smith et all. *Global First Level Trigger Timing*, ZEUS-Note 90-11

[44] R.Brun et al., *GEANT 3.13* CERN DD/EE/84-1(1987).

[45] S.M.Fisher and P.Palazzi *The ADAMO Data System* Programmers Manual.

[46] H.Uijterwall and R. van De Woudenberg (Ed), *ZGANA1.7,Analysis code for the ZG31T1 Monte Carlo.* Documentation.

[47] G.Ingelman, *LEPTO 6.1 – The Lund Monte Carlo for deep inelastic lepton–nucleon scattering*, Proc. of the DESY Workshop 'Physics at HERA. Ed. W.Buchmüller and G.Ingelman. Hamburg (1991) 1366.

[48] M.Bengtsson, T.Sjöstrand, *Z.Phys.* **C37**(1988) 465.

[49] L. Lönnblad, *ARIADNE v. 4*, program and manual, *Comp.Phys.Comm.* **71** (1992) 15.

[50] JETSET 6.3: T.Sjöstrand, *Comput. Phys.Commun.* **39** (1986) 347.
T.Sjöstrand and M.Bengtesson, *Comput.Phys.Commun.* **43** (1987) 347.

[51] B.Anderson et al., *Phys.Pep.* **97** (1983) 31.

[52] K. Charchuła, G. Schuler and H. Spiesberger, *Comp.Phys.Comm.*,**81** (1994) 381.

[53] A. Kwiatkowski, H. Spiesberger and H. J. Möhring, *Comp.Phys.Comm.*,**69** (1992) 155.

[54] G.Marchesini et al. Herwig a Monte Carlo event generator for simulating Hadron Emission Reactions With Interfering Gluons" *DESY 91-048.*

[55] G.Marchesini and B.R.Webber, *Nucl. Phys.* **B 310** (1988) 461.

[56] E.Mirkes *Theory of Jets in Deep Inelastic Scattering hep-ph/9711224.*

[57] F.Jacket and A.Blondel, in *An ep facility for Europe*, Proc.Hamburg(1979)391.

[58] S.Bentvelsen, J.Engelen and P.Kooijman, Reconstruction of (x, Q^2) and Extraction of Structure functions in Neutral Current Scattering at HERA, Proc. of the Workshop on Physics at HERA Vol.1(1991)23,Ed.W.Buchmüller and G.Ingelman

[59] ELEC5 electron finder, Phantom user library.

[60] LOCAL electron finder, Phantom user library.

[61] R.Gläser et al., *ZEUS Software Release - November 1990*, ZEUS-Note 90-114 (1990).

[62] E.Tscheslog *ZEUS Reconstruction Program Organization and Control*, ZEUS-Note 91-037 (1991).

[63] E.Gallo *The TLT and DST filters for the DIS group in 1995.* ZEUS-Note 96-001.

[64] ZEUS Collaboration, PHANTOM-Physics analysis techniques, operations and methods - Collection of subroutines/functions and packages of routines for data analysis.

[65] JADE Collaboration, W.Bartel et al., *Zeit.Phys.* **C33** (1986) 23.
S.Bethke et al., *Phys.Lett.* **213B** (1988) 235.

[66] S.D.Ellis, D.E.Soper *Phys.Rev.* **D48**(1993) 3160.

[67] G.Sternam and S.Weinberg, *Phys.Rev.* **Lett39** (1977) 1436.

[68] J.Hurth et al., Proc . of the 1990 DPF Summer Study on High Energy Physics, Snowmass, Colorado, edited by E.L.Berger World Scientific, Singapore, (1992) p.134

[69] P.d.Jong, 'Status of the Uranimu Calorimeter Reconstruction Software', ZEUS-Note 92-019.

[70] CDF Collab., F.Abe et al., *Phys.Rev.* **D45** (1992) 1448.

[71] S.D.Ellis, Z.Kunszt D.E.Soper, *Phys.Rev.Lett.* **69** (1992) 3615.

[72] G.Kramer, S.G.Salesch, *Phys.Lett.* **B317** (1993) 218.
S.G.Salesch, DESY 93-196 (1993).
G.Kramer, S.G.Salesch, *Phys.Lett.* **B333** (1994) 519.

[73] J.Repond, *Jet Energy Corrections*, ZEUS Note 96-133.

[74] G.Kramer, J.Pötter *Low Q^2 Jet Production at HERA in Next-to-Leading Order QCD"*, DESY-98-046, hep-ph/9804352.

[75] M.Klasen and G.Kramer, *Phys.Lett.* **B507** (1996) 385.

[76] S.Frixione and G.Ridolfi *Nucl.Phys.* **B507** (1997) 315.

[77] S.Catani and B.Webber, JHEP 10 (1997) 005.

A Appendix

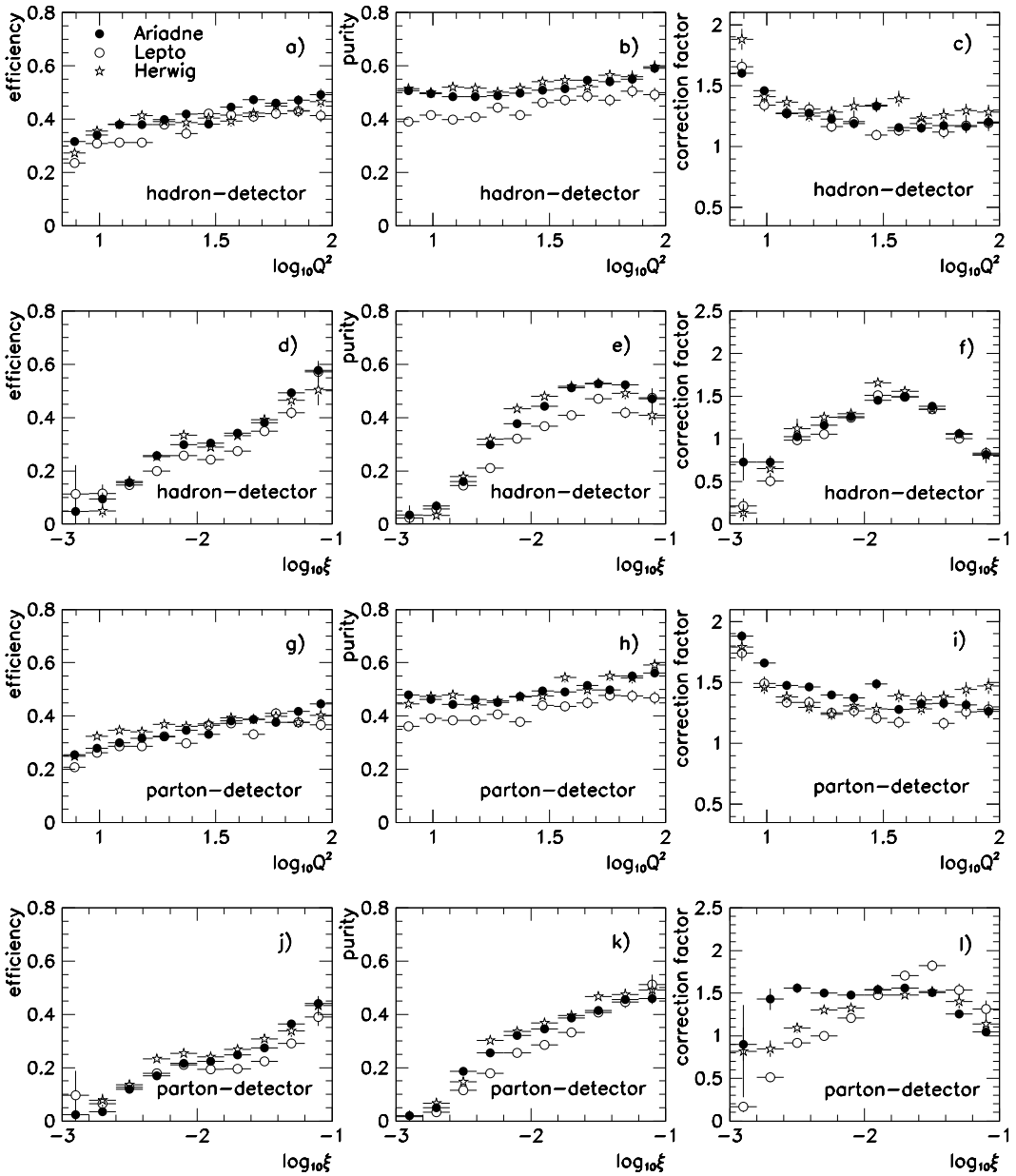

Figure A.1: *Purity, efficiency and correction factors versus Q^2, ξ calculated based on Ariadne(black points), Lepto(open dots) and Herwig(stars) MC hadron-detector (a,b,c,d,e,f) and parton-detector (g,h,i,j,k,l) comparison. At low values of ξ both the purities and the efficiencies of the measurement are low, thus introducing large experimental uncertainties. Jets were reconstructed using the cone algorithm.*

	hadron level				parton level			
Q^2	$\frac{d\sigma}{dlog_{10}Q^2}$	$\pm$ stat	$\pm$ sys	$\pm$ corr.syst [nb]	$\frac{d\sigma}{dlog_{10}Q^2}$	$\pm$ stat	$\pm$ sys	$\pm$ corr.syst [nb]
7.00 - 8.74	4.34	$\pm$ 0.15	$^{+0.92}_{-0.56}$	$^{+0.35}_{-0.45}$	5.84	$\pm$ 0.18	$^{+0.26}_{-0.87}$	$^{+0.52}_{-0.49}$
8.74 - 10.90	4.09	$\pm$ 0.14	$^{+0.34}_{-0.64}$	$^{+0.41}_{-0.41}$	5.37	$\pm$ 0.17	$^{+0.28}_{-1.00}$	$^{+0.54}_{-0.51}$
10.90 - 13.61	3.67	$\pm$ 0.13	$^{+0.31}_{-0.33}$	$^{+0.35}_{-0.36}$	4.83	$\pm$ 0.17	$^{+0.12}_{-0.64}$	$^{+0.41}_{-0.37}$
13.61 - 16.98	3.21	$\pm$ 0.12	$^{+0.26}_{-0.33}$	$^{+0.34}_{-0.38}$	4.30	$\pm$ 0.15	$^{+0.25}_{-0.75}$	$^{+0.40}_{-0.37}$
16.98 - 21.20	2.89	$\pm$ 0.11	$^{+0.17}_{-0.35}$	$^{+0.30}_{-0.25}$	3.70	$\pm$ 0.13	$^{+0.12}_{-0.57}$	$^{+0.28}_{-0.31}$
21.20 - 26.46	2.60	$\pm$ 0.10	$^{+0.34}_{-0.16}$	$^{+0.24}_{-0.21}$	3.37	$\pm$ 0.13	$^{+0.14}_{-0.38}$	$^{+0.27}_{-0.30}$
26.46 - 33.02	2.58	$\pm$ 0.11	$^{+0.09}_{-0.48}$	$^{+0.23}_{-0.19}$	3.21	$\pm$ 0.13	$^{+0.10}_{-0.77}$	$^{+0.27}_{-0.24}$
33.02 - 41.21	2.00	$\pm$ 0.09	$^{+0.43}_{-0.09}$	$^{+0.18}_{-0.17}$	2.50	$\pm$ 0.10	$^{+0.29}_{-0.30}$	$^{+0.21}_{-0.17}$
41.21 - 51.44	1.92	$\pm$ 0.09	$^{+0.17}_{-0.14}$	$^{+0.16}_{-0.17}$	2.48	$\pm$ 0.11	$^{+0.06}_{-0.19}$	$^{+0.20}_{-0.13}$
51.44 - 64.20	1.64	$\pm$ 0.08	$^{+0.15}_{-0.13}$	$^{+0.13}_{-0.15}$	2.08	$\pm$ 0.10	$^{+0.17}_{-0.29}$	$^{+0.12}_{-0.11}$
64.20 - 80.12	1.43	$\pm$ 0.08	$^{+0.16}_{-0.15}$	$^{+0.12}_{-0.08}$	1.74	$\pm$ 0.09	$^{+0.22}_{-0.12}$	$^{+0.08}_{-0.10}$
80.12 - 100.0	1.21	$\pm$ 0.07	$^{+0.15}_{-0.05}$	$^{+0.08}_{-0.11}$	1.46	$\pm$ 0.08	$^{+0.28}_{-0.14}$	$^{+0.15}_{-0.09}$
ξ	$\frac{d\sigma}{dlog_{10}\xi}$	$\pm$ stat	$\pm$ sys	$\pm$ corr.syst[nb]	$\frac{d\sigma}{dlog_{10}\xi}$	$\pm$ stat	$\pm$ sys	$\pm$ corr.syst [nb]
0.0010 - 0.0016	0.02	$\pm$ 0.01	$^{+0.01}_{-0.02}$	$^{+0.00}_{+0.00}$	0.04	$\pm$ 0.01	$^{+0.02}_{-0.03}$	$^{+0.00}_{+0.00}$
0.0016 - 0.0025	0.12	$\pm$ 0.01	$^{+0.02}_{-0.04}$	$^{+0.01}_{-0.02}$	0.34	$\pm$ 0.04	$^{+0.03}_{-0.22}$	$^{+0.01}_{-0.02}$
0.0025 - 0.0040	0.72	$\pm$ 0.04	$^{+0.09}_{-0.05}$	$^{+0.07}_{-0.04}$	1.37	$\pm$ 0.07	$^{+0.04}_{-0.59}$	$^{+0.08}_{-0.01}$
0.0040 - 0.0063	1.86	$\pm$ 0.07	$^{+0.22}_{-0.20}$	$^{+0.11}_{-0.04}$	2.77	$\pm$ 0.09	$^{+0.17}_{-0.81}$	$^{+0.06}_{-0.06}$
0.0063 - 0.0100	2.69	$\pm$ 0.08	$^{+0.20}_{-0.15}$	$^{+0.23}_{-0.27}$	3.69	$\pm$ 0.10	$^{+0.08}_{-0.67}$	$^{+0.32}_{-0.25}$
0.0100 - 0.0158	3.42	$\pm$ 0.10	$^{+0.56}_{-0.17}$	$^{+0.21}_{-0.26}$	4.07	$\pm$ 0.11	$^{+0.25}_{-0.32}$	$^{+0.25}_{-0.31}$
0.0158 - 0.0251	3.29	$\pm$ 0.09	$^{+0.24}_{-0.31}$	$^{+0.29}_{-0.33}$	3.79	$\pm$ 0.10	$^{+0.26}_{-0.44}$	$^{+0.36}_{-0.34}$
0.0251 - 0.0398	2.14	$\pm$ 0.07	$^{+0.11}_{-0.36}$	$^{+0.28}_{-0.23}$	2.52	$\pm$ 0.08	$^{+0.21}_{-0.45}$	$^{+0.32}_{-0.27}$
0.0398 - 0.0631	0.77	$\pm$ 0.03	$^{+0.05}_{-0.22}$	$^{+0.13}_{-0.14}$	0.96	$\pm$ 0.04	$^{+0.08}_{-0.26}$	$^{+0.15}_{-0.17}$
0.0631 - 0.1000	0.18	$\pm$ 0.01	$^{+0.05}_{-0.04}$	$^{+0.04}_{-0.04}$	0.25	$\pm$ 0.02	$^{+0.06}_{-0.07}$	$^{+0.05}_{-0.05}$

Table A.1: *Differential cross section at hadron and parton levels for Q^2 and ξ distributions. There are 12 equidistant bins in $log_{10}Q^2$ ($7GeV^2 < Q^2 < 100GeV^2$) and 10 in $log_{10}\xi$ ($0.001 < \xi < 0.1$). Jets were reconstructed using the cone algorithm.*

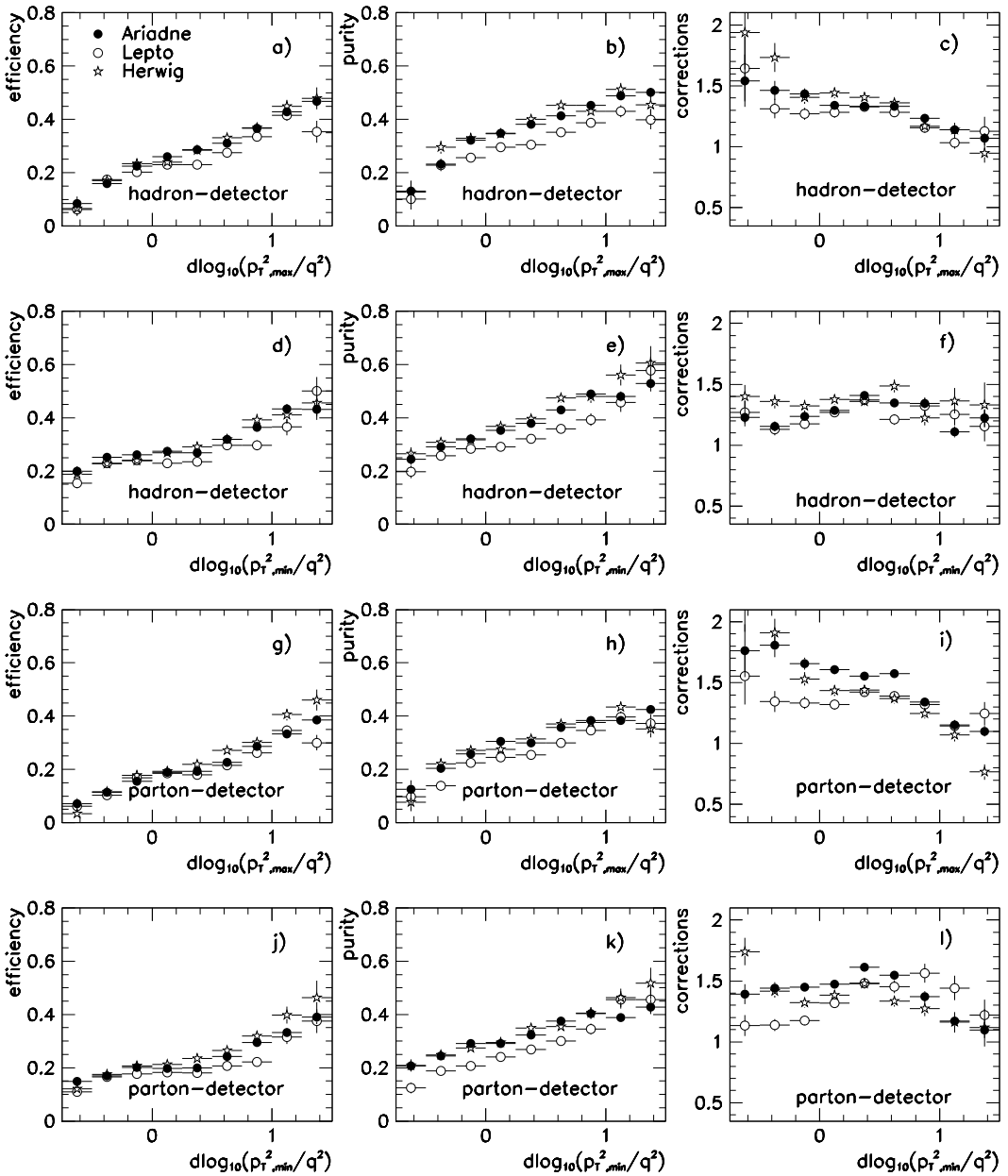

Figure A.2: *Purity, efficiency and correction factors versus $p^2_{T,max}/Q^2$, $p^2_{T,min}/Q^2$ calculated based on Ariadne(black points), Lepto(open dots) and Herwig(stars) MC hadron-detector (a,b,c,d,e,f) and parton-detector (g,h,i,j,k,l) comparison. At low values of p^2_T/Q^2 both the purities and the efficiencies of the measurement are low, thus introducing large experimental uncertainties. Jets were reconstructed using the cone algorithm.*

	hadron level				parton level			
$p^2_{T,max}/Q^2$	$\frac{d\sigma}{dlog_{10}(p^2_{T,max}/Q^2)}$	$\pm$ stat	$\pm$ sys	$\pm$ corr.syst[nb]	$\frac{d\sigma}{dlog_{10}(p^2_{T,max}/Q^2)}$	$\pm$ stat	$\pm$ sys	$\pm$ corr.syst[nb]
0.18 - 0.32	0.09	$\pm$ 0.02	$^{+0.03}_{-0.02}$	$^{+0.01}_{+0.01}$	0.09	$\pm$ 0.02	$^{+0.05}_{-0.01}$	$^{+0.00}_{-0.02}$
0.32 - 0.56	0.49	$\pm$ 0.03	$^{+0.11}_{-0.07}$	$^{+0.02}_{-0.06}$	0.70	$\pm$ 0.05	$^{+0.04}_{-0.23}$	$^{+0.05}_{+0.02}$
0.56 - 1.00	1.24	$\pm$ 0.05	$^{+0.10}_{-0.20}$	$^{+0.07}_{-0.03}$	1.52	$\pm$ 0.06	$^{+0.09}_{-0.34}$	$^{+0.05}_{-0.04}$
1.00 - 1.78	2.17	$\pm$ 0.07	$^{+0.20}_{-0.12}$	$^{+0.12}_{-0.15}$	2.84	$\pm$ 0.09	$^{+0.22}_{-0.58}$	$^{+0.17}_{-0.16}$
1.78 - 3.16	3.02	$\pm$ 0.08	$^{+0.21}_{-0.33}$	$^{+0.36}_{-0.27}$	4.00	$\pm$ 0.10	$^{+0.09}_{-0.50}$	$^{+0.35}_{-0.26}$
3.16 - 5.62	2.82	$\pm$ 0.07	$^{+0.11}_{-0.14}$	$^{+0.21}_{-0.25}$	3.79	$\pm$ 0.09	$^{+0.13}_{-0.63}$	$^{+0.30}_{-0.38}$
5.62 - 10.00	1.53	$\pm$ 0.05	$^{+0.03}_{-0.14}$	$^{+0.17}_{-0.21}$	1.98	$\pm$ 0.06	$^{+0.03}_{-0.20}$	$^{+0.22}_{-0.20}$
10.00 - 17.78	0.67	$\pm$ 0.03	$^{+0.02}_{-0.09}$	$^{+0.09}_{-0.10}$	0.82	$\pm$ 0.03	$^{+0.02}_{-0.13}$	$^{+0.10}_{-0.09}$
17.78 - 31.62	0.21	$\pm$ 0.01	$^{+0.02}_{-0.03}$	$^{+0.04}_{-0.03}$	0.27	$\pm$ 0.02	$^{+0.03}_{-0.09}$	$^{+0.05}_{-0.05}$
$p^2_{T,min}/Q^2$	$\frac{d\sigma}{dlog_{10}(p^2_{T,min}/Q^2)}$	$\pm$ stat	$\pm$ sys	$\pm$ corr.sys[nb]	$\frac{d\sigma}{dlog_{10}(p^2_{T,min}/Q^2)}$	$\pm$ stat	$\pm$ sys	$\pm$ corr.sys[nb]
0.18 - 0.32	0.35	$\pm$ 0.03	$^{+0.06}_{-0.01}$	$^{+0.02}_{-0.02}$	0.43	$\pm$ 0.03	$^{+0.15}_{-0.10}$	$^{+0.02}_{-0.01}$
0.32 - 0.56	1.03	$\pm$ 0.05	$^{+0.18}_{-0.06}$	$^{+0.06}_{-0.07}$	1.42	$\pm$ 0.06	$^{+0.01}_{-0.32}$	$^{+0.08}_{-0.02}$
0.56 - 1.00	1.87	$\pm$ 0.06	$^{+0.15}_{-0.18}$	$^{+0.18}_{-0.14}$	2.40	$\pm$ 0.07	$^{+0.10}_{-0.51}$	$^{+0.16}_{-0.15}$
1.00 - 1.78	2.81	$\pm$ 0.07	$^{+0.27}_{-0.21}$	$^{+0.23}_{-0.24}$	3.63	$\pm$ 0.09	$^{+0.18}_{-0.49}$	$^{+0.26}_{-0.29}$
1.78 - 3.16	3.37	$\pm$ 0.09	$^{+0.09}_{-0.27}$	$^{+0.29}_{-0.36}$	4.45	$\pm$ 0.10	$^{+0.11}_{-0.61}$	$^{+0.41}_{-0.35}$
3.16 - 5.62	1.71	$\pm$ 0.05	$^{+0.18}_{-0.18}$	$^{+0.18}_{-0.17}$	2.28	$\pm$ 0.07	$^{+0.08}_{-0.30}$	$^{+0.26}_{-0.26}$
5.62 - 10.00	0.71	$\pm$ 0.03	$^{+0.02}_{-0.09}$	$^{+0.10}_{-0.09}$	0.87	$\pm$ 0.04	$^{+0.10}_{-0.12}$	$^{+0.10}_{-0.08}$
10.00 - 17.78	0.23	$\pm$ 0.02	$^{+0.06}_{-0.03}$	$^{+0.04}_{-0.03}$	0.28	$\pm$ 0.02	$^{+0.06}_{-0.04}$	$^{+0.03}_{-0.04}$
17.78 - 31.62	0.09	$\pm$ 0.01	$^{+0.01}_{-0.02}$	$^{+0.01}_{-0.01}$	0.10	$\pm$ 0.01	$^{+0.01}_{-0.01}$	$^{+0.01}_{-0.01}$

Table A.2: *Differential cross section at hadron and parton levels for $p^2_{T,max}/Q^2$ and $p^2_{T,min}/Q^2$ distributions. There are 9 equidistant bins in $log_{10}(p^2_T/Q^2)$ ($-0.75 < log_{10}(p^2_T/Q^2) < 1.5$). Jets were reconstructed using the cone algorithm.*

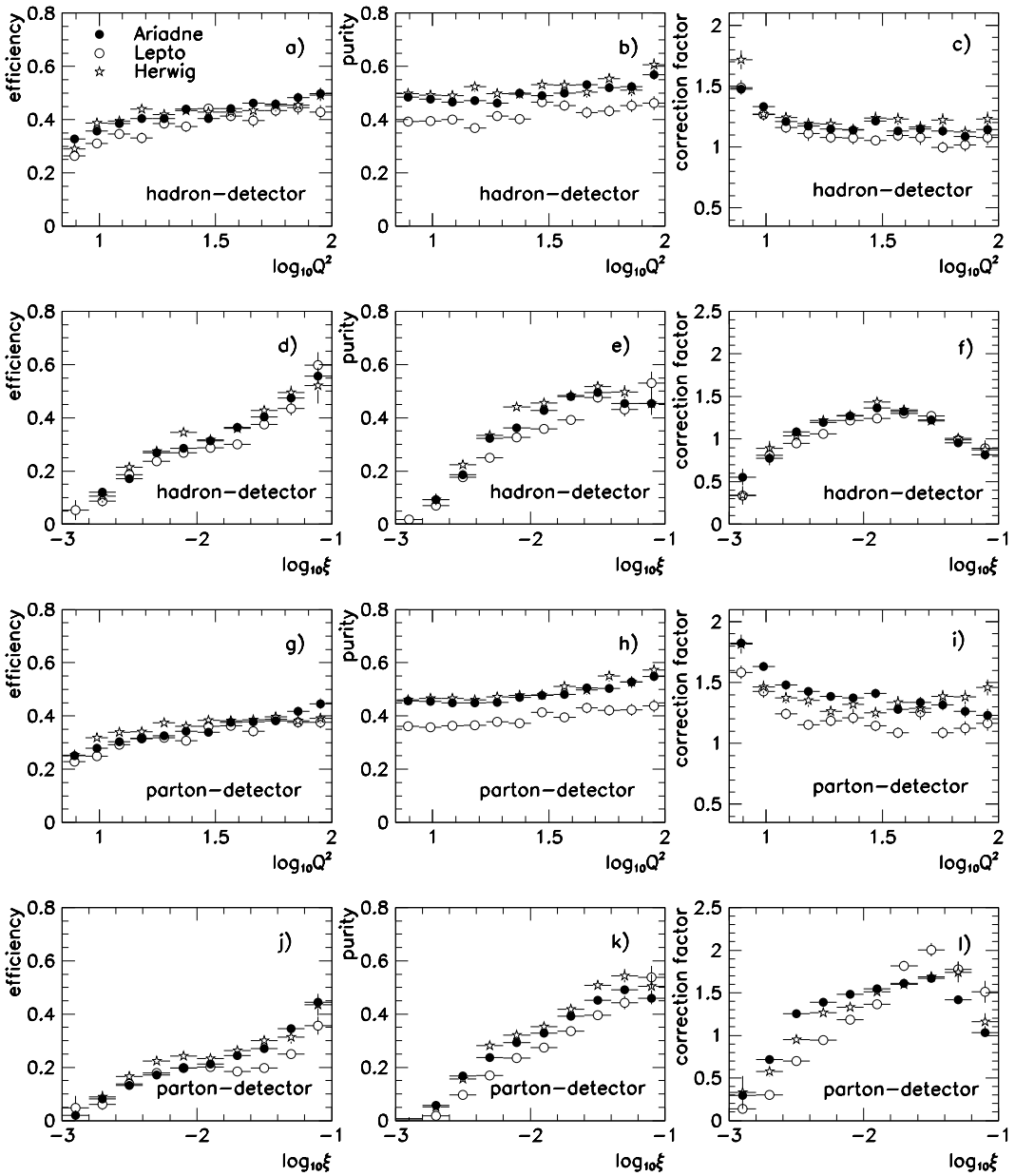

Figure A.3: *Purity, efficiency and correction factors versus Q^2, ξ calculated based on Ariadne(black points), Lepto(open dots) and Herwig(stars) MC hadron-detector (a,b,c,d,e,f) and parton-detector (g,h,i,j,k,l) comparison. At low values of ξ both the purities and the efficiencies of the measurement are low, thus introducing large experimental uncertainties. Jets were reconstructed using the k_T algorithm.*

	hadron level				parton level			
Q^2	$\frac{d\sigma}{dlog_{10}Q^2}$	$\pm$ stat	$\pm$ sys	$\pm$ corr.syst [nb]	$\frac{d\sigma}{dlog_{10}Q^2}$	$\pm$ stat	$\pm$ sys	$\pm$ corr.syst [nb]
7.00 - 8.73	3.74	$\pm$ 0.13	$^{+0.76}_{-0.38}$	$^{+0.36}_{-0.42}$	5.39	$\pm$ 0.17	$^{+0.29}_{-0.81}$	$^{+0.57}_{-0.39}$
8.73 - 10.90	3.61	$\pm$ 0.13	$^{+0.24}_{-0.50}$	$^{+0.46}_{-0.44}$	5.14	$\pm$ 0.17	$^{+0.32}_{-0.94}$	$^{+0.46}_{-0.45}$
10.90 - 13.61	3.27	$\pm$ 0.13	$^{+0.26}_{-0.41}$	$^{+0.35}_{-0.39}$	4.63	$\pm$ 0.16	$^{+0.23}_{-0.77}$	$^{+0.40}_{-0.46}$
13.61 - 16.98	2.92	$\pm$ 0.11	$^{+0.19}_{-0.42}$	$^{+0.37}_{-0.31}$	4.12	$\pm$ 0.14	$^{+0.22}_{-0.77}$	$^{+0.40}_{-0.43}$
16.98 - 21.20	2.59	$\pm$ 0.10	$^{+0.17}_{-0.29}$	$^{+0.23}_{-0.26}$	3.55	$\pm$ 0.13	$^{+0.21}_{-0.54}$	$^{+0.31}_{-0.32}$
21.20 - 26.46	2.42	$\pm$ 0.10	$^{+0.09}_{-0.28}$	$^{+0.27}_{-0.25}$	3.34	$\pm$ 0.13	$^{+0.16}_{-0.49}$	$^{+0.28}_{-0.30}$
26.46 - 33.02	2.23	$\pm$ 0.10	$^{+0.11}_{-0.27}$	$^{+0.22}_{-0.24}$	2.92	$\pm$ 0.12	$^{+0.15}_{-0.49}$	$^{+0.23}_{-0.24}$
33.02 - 41.21	1.90	$\pm$ 0.08	$^{+0.20}_{-0.15}$	$^{+0.21}_{-0.19}$	2.43	$\pm$ 0.10	$^{+0.24}_{-0.27}$	$^{+0.19}_{-0.24}$
41.21 - 51.44	1.78	$\pm$ 0.09	$^{+0.06}_{-0.12}$	$^{+0.15}_{-0.16}$	2.34	$\pm$ 0.11	$^{+0.08}_{-0.14}$	$^{+0.19}_{-0.20}$
51.44 - 64.20	1.52	$\pm$ 0.08	$^{+0.14}_{-0.19}$	$^{+0.12}_{-0.13}$	1.99	$\pm$ 0.10	$^{+0.12}_{-0.33}$	$^{+0.16}_{-0.13}$
64.20 - 80.12	1.26	$\pm$ 0.07	$^{+0.11}_{-0.09}$	$^{+0.10}_{-0.09}$	1.62	$\pm$ 0.09	$^{+0.20}_{-0.15}$	$^{+0.12}_{-0.11}$
80.12 - 100.0	1.13	$\pm$ 0.07	$^{+0.14}_{-0.09}$	$^{+0.09}_{-0.10}$	1.39	$\pm$ 0.08	$^{+0.27}_{-0.11}$	$^{+0.15}_{-0.08}$
ξ	$\frac{d\sigma}{dlog_{10}\xi}$	$\pm$ stat	$\pm$ sys	$\pm$ corr.syst[nb]	$\frac{d\sigma}{dlog_{10}\xi}$	$\pm$ stat	$\pm$ sys	$\pm$ corr.syst [nb]
0.0010 - 0.0016	0.04	$\pm$ 0.01	$^{+0.00}_{-0.02}$	$^{+0.01}_{-0.01}$	0.03	$\pm$ 0.01	$^{+0.01}_{-0.02}$	$^{+0.01}_{-0.01}$
0.0016 - 0.0025	0.24	$\pm$ 0.02	$^{+0.07}_{-0.04}$	$^{+0.02}_{-0.02}$	0.30	$\pm$ 0.02	$^{+0.05}_{-0.17}$	$^{+0.01}_{-0.01}$
0.0025 - 0.0040	0.94	$\pm$ 0.05	$^{+0.01}_{-0.14}$	$^{+0.07}_{-0.05}$	1.34	$\pm$ 0.06	$^{+0.02}_{-0.57}$	$^{+0.05}_{-0.07}$
0.0040 - 0.0063	2.03	$\pm$ 0.07	$^{+0.08}_{-0.26}$	$^{+0.21}_{-0.16}$	2.79	$\pm$ 0.09	$^{+0.03}_{-0.77}$	$^{+0.18}_{-0.11}$
0.0063 - 0.0100	2.68	$\pm$ 0.08	$^{+0.10}_{-0.12}$	$^{+0.21}_{-0.24}$	3.58	$\pm$ 0.10	$^{+0.09}_{-0.52}$	$^{+0.26}_{-0.27}$
0.0100 - 0.0158	3.02	$\pm$ 0.08	$^{+0.29}_{-0.27}$	$^{+0.24}_{-0.32}$	3.89	$\pm$ 0.11	$^{+0.23}_{-0.36}$	$^{+0.34}_{-0.33}$
0.0158 - 0.0251	2.63	$\pm$ 0.07	$^{+0.16}_{-0.25}$	$^{+0.31}_{-0.24}$	3.49	$\pm$ 0.09	$^{+0.53}_{-0.29}$	$^{+0.38}_{-0.34}$
0.0251 - 0.0398	1.49	$\pm$ 0.06	$^{+0.13}_{-0.21}$	$^{+0.19}_{-0.24}$	2.20	$\pm$ 0.08	$^{+0.33}_{-0.32}$	$^{+0.28}_{-0.34}$
0.0398 - 0.0631	0.53	$\pm$ 0.03	$^{+0.05}_{-0.11}$	$^{+0.10}_{-0.09}$	0.84	$\pm$ 0.04	$^{+0.11}_{-0.17}$	$^{+0.14}_{-0.12}$
0.0631 - 0.1000	0.14	$\pm$ 0.01	$^{+0.03}_{-0.02}$	$^{+0.02}_{-0.04}$	0.20	$\pm$ 0.02	$^{+0.05}_{-0.04}$	$^{+0.04}_{-0.04}$

Table A.3: *Differential cross section at hadron and parton levels for Q^2 and ξ distributions. There are 12 equidistant bins in $log_{10}Q^2$ ($7GeV^2 < Q^2 < 100GeV^2$) and 10 in $log_{10}\xi$ ($0.001 < \xi < 0.1$) Jets were reconstructed using the k_T algorithm.*

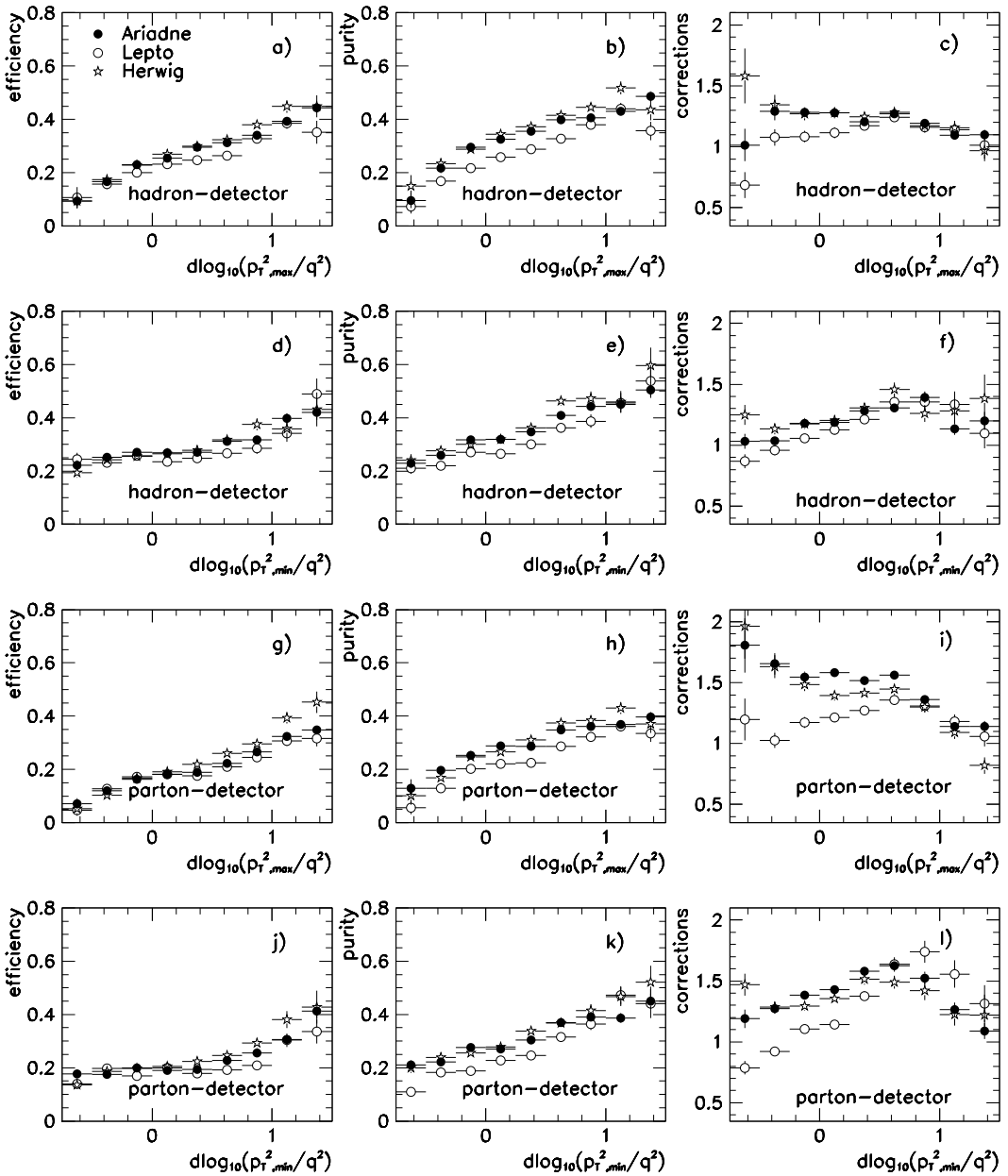

Figure A.4: *Purity, efficiency and correction factors versus $p^2_{T,max}/Q^2$, $p^2_{T,min}/Q^2$ calculated based on Ariadne(black points), Lepto(open dots) and Herwig(stars) MC hadron-detector(a,b,c,d,e,f) and parton-detector (g,h,i,j,k,l) comparison. At low values of p^2_T/Q^2 both the purities and the efficiencies of the measurement are low, thus introducing large experimental uncertainties. Jets were reconstructed using the k_T algorithm.*

	hadron level				parton level			
$p^2_{T,max}/Q^2$	$\frac{d\sigma}{dlog_{10}(p^2_{T,max}/Q^2)}$	$\pm$ stat	$\pm$ sys	$\pm$ corr.syst[nb]	$\frac{d\sigma}{dlog_{10}(p^2_{T,max}/Q^2)}$	$\pm$ stat	$\pm$ sys	$\pm$ corr.syst[nb]
0.18 - 0.32	0.05	$\pm$ 0.01	$^{+0.07}_{-0.02}$	$^{+0.00}_{+0.00}$	0.10	$\pm$ 0.02	$^{+0.25}_{-0.03}$	$^{+0.01}_{-0.02}$
0.32 - 0.56	0.43	$\pm$ 0.03	$^{+0.02}_{-0.10}$	$^{+0.03}_{+0.00}$	0.59	$\pm$ 0.04	$^{+0.05}_{-0.23}$	$^{+0.04}_{+0.01}$
0.56 - 1.00	1.09	$\pm$ 0.05	$^{+0.08}_{-0.18}$	$^{+0.06}_{-0.10}$	1.44	$\pm$ 0.06	$^{+0.09}_{-0.33}$	$^{+0.08}_{-0.08}$
1.00 - 1.78	2.01	$\pm$ 0.06	$^{+0.08}_{-0.31}$	$^{+0.21}_{-0.15}$	2.73	$\pm$ 0.08	$^{+0.17}_{-0.68}$	$^{+0.15}_{-0.20}$
1.78 - 3.16	2.62	$\pm$ 0.07	$^{+0.15}_{-0.26}$	$^{+0.28}_{-0.30}$	3.79	$\pm$ 0.09	$^{+0.11}_{-0.62}$	$^{+0.35}_{-0.27}$
3.16 - 5.62	2.59	$\pm$ 0.07	$^{+0.08}_{-0.12}$	$^{+0.28}_{-0.27}$	3.66	$\pm$ 0.09	$^{+0.08}_{-0.42}$	$^{+0.32}_{-0.36}$
5.62 - 10.00	1.38	$\pm$ 0.05	$^{+0.04}_{-0.05}$	$^{+0.16}_{-0.17}$	1.85	$\pm$ 0.06	$^{+0.08}_{-0.09}$	$^{+0.20}_{-0.22}$
10.00 - 17.78	0.60	$\pm$ 0.03	$^{+0.07}_{-0.02}$	$^{+0.08}_{-0.08}$	0.76	$\pm$ 0.03	$^{+0.09}_{-0.04}$	$^{+0.10}_{-0.08}$
17.78 - 31.62	0.21	$\pm$ 0.01	$^{+0.01}_{-0.03}$	$^{+0.03}_{-0.05}$	0.28	$\pm$ 0.02	$^{+0.01}_{-0.09}$	$^{+0.05}_{-0.04}$
$p^2_{T,min}/Q^2$	$\frac{d\sigma}{dlog_{10}(p^2_{T,min}/Q^2)}$	$\pm$ stat	$\pm$ sys	$\pm$ corr.sys[nb]	$\frac{d\sigma}{dlog_{10}(p^2_{T,min}/Q^2)}$	$\pm$ stat	$\pm$ sys	$\pm$ corr.sys[nb]
0.18 - 0.32	0.31	$\pm$ 0.02	$^{+0.07}_{-0.05}$	$^{+0.02}_{-0.01}$	0.38	$\pm$ 0.03	$^{+0.10}_{-0.13}$	$^{+0.02}_{-0.02}$
0.32 - 0.56	0.91	$\pm$ 0.04	$^{+0.10}_{-0.09}$	$^{+0.08}_{-0.08}$	1.24	$\pm$ 0.05	$^{+0.05}_{-0.30}$	$^{+0.11}_{-0.11}$
0.56 - 1.00	1.79	$\pm$ 0.06	$^{+0.04}_{-0.20}$	$^{+0.18}_{-0.18}$	2.35	$\pm$ 0.07	$^{+0.10}_{-0.43}$	$^{+0.16}_{-0.14}$
1.00 - 1.78	2.54	$\pm$ 0.07	$^{+0.15}_{-0.30}$	$^{+0.28}_{-0.27}$	3.48	$\pm$ 0.09	$^{+0.17}_{-0.64}$	$^{+0.28}_{-0.32}$
1.78 - 3.16	2.93	$\pm$ 0.08	$^{+0.11}_{-0.22}$	$^{+0.28}_{-0.32}$	4.17	$\pm$ 0.10	$^{+0.12}_{-0.51}$	$^{+0.40}_{-0.38}$
3.16 - 5.62	1.51	$\pm$ 0.05	$^{+0.20}_{-0.04}$	$^{+0.19}_{-0.15}$	2.19	$\pm$ 0.07	$^{+0.16}_{-0.19}$	$^{+0.24}_{-0.21}$
5.62 - 10.00	0.61	$\pm$ 0.03	$^{+0.02}_{-0.06}$	$^{+0.05}_{-0.10}$	0.82	$\pm$ 0.04	$^{+0.16}_{-0.08}$	$^{+0.09}_{-0.07}$
10.00 - 17.78	0.21	$\pm$ 0.02	$^{+0.05}_{-0.01}$	$^{+0.03}_{-0.02}$	0.27	$\pm$ 0.02	$^{+0.09}_{-0.01}$	$^{+0.03}_{-0.04}$
17.78 - 31.62	0.08	$\pm$ 0.01	$^{+0.01}_{-0.01}$	$^{+0.01}_{-0.01}$	0.09	$\pm$ 0.01	$^{+0.02}_{-0.01}$	$^{+0.01}_{-0.01}$

Table A.4: *Differential cross section at hadron and parton levels for $p^2_{T,max}/Q^2$ and $p^2_{T,min}/Q^2$ distributions. There are 9 equidistant bins in $log_{10}(p^2_T/Q^2)$ ($-0.75 < log_{10}(p^2_T/Q^2) < 1.5$). Jets were reconstructed using the k_T algorithm.*